FABRICATION AND CHARACTERIZATION OF ZINC OXIDE THIN FILMS FOR OPTOELECTRONIC APPLICATIONS

SITI HAJAR BINTI BASRI

FACULTY OF SCIENCE
UNIVERSITY OF MALAYA
KUALA LUMPUR

2017

FABRICATION AND CHARACTERIZATION OF ZINC OXIDE THIN FILMS FOR OPTOELECTRONIC APPLICATIONS

SITI HAJAR BINTI BASRI

DISSERTATION SUBMITTED IN FULFILMENT OF THE REQUIREMENTS FOR THE DEGREE OF MASTER OF SCIENCE

DEPARTMENT OF PHYSICS
FACULTY OF SCIENCE
UNIVERSITY OF MALAYA
KUALA LUMPUR

2017

UNIVERSITY OF MALAYA

ORIGINAL LITERARY WORK DECLARATION

Name of Candidate: **Siti Hajar binti Basri** (I.C/Passport No:)

Registration/Matric No: **SGR110108**

Name of Degree: **Master of Science**

Title of Project Paper/Research Report/Dissertation/Thesis ("this Work"):

Fabrication and Characterization of Zinc Oxide Thin Films for Optoelectronic Applications

Field of Study: **Experimental Physics**

I do solemnly and sincerely declare that:

(1) I am the sole author/writer of this Work;
(2) This Work is original;
(3) Any use of any work in which copyright exists was done by way of fair dealing and for permitted purposes and any excerpt or extract from, or reference to or reproduction of any copyright work has been disclosed expressly and sufficiently and the title of the Work and its authorship have been acknowledged in this Work;
(4) I do not have any actual knowledge nor do I ought reasonably to know that the making of this work constitutes an infringement of any copyright work;
(5) I hereby assign all and every rights in the copyright to this Work to the University of Malaya ("UM"), who henceforth shall be owner of the copyright in this Work and that any reproduction or use in any form or by any means whatsoever is prohibited without the written consent of UM having been first had and obtained;
(6) I am fully aware that if in the course of making this Work I have infringed any copyright whether intentionally or otherwise, I may be subject to legal action or any other action as may be determined by UM.

Candidate's Signature Date:

Subscribed and solemnly declared before,

Witness's Signature Date:

Name:

Designation:

ABSTRACT

Zinc oxide (ZnO) has attracted many attentions recently due its versatility in various semiconductor fields. ZnO has a wurtzite structure with a wide band gap energy of 3.3 eV and very large excitation binding energy which is 60 meV at room temperature. Thus, they are commercially valuable in optoelectronic devices. Some main interests of this material are nontoxic, inexpensive, highly transparent in visible range and conductive in electrical devices. Thus, they are very potential for application in various optoelectronic devices. However, pure zinc oxide thin film naturally has a high resistivity characteristics because of low carrier concentration. In order to improve the conductivity, ZnO thin films were doped with impurities to increase the carrier concentration and/or carrier mobility. In this work, ZnO thin films with Ni-doping were successfully produced by sol-gel spin coating method. Zinc acetate dihydrate was used as the Zn precursor, and nickel (II) acetate tetrahydrate was used as a source of Ni-dopant. The solutions were prepared by dissolving zinc acetate and nickel (II) acetate in ethanol, and diethanolamine (DEA) was used as its chelating agent. Thin films were fabricated by spin-coating method on top of glass substrates. ZnO films underwent pre-heating and post-heating treatment at 300 °C for 10 minutes and 500 °C for 1 h respectively. The influence of nickel in zinc oxide thin film on structural, surface morphology, optical, luminescence, electrical and electronic structure properties were investigated. It is observed that XRD pattern of all thin films are indifferent, with no peak signifying metallic Zn, Ni or NiO. This indicates impurity ions (Ni^{+}) were substituted with Zn atoms which cause no variations in the structural characteristic. FESEM images show the thin films exhibit a smooth surface with grain size of 50 - 70 nm which slightly varies with different Ni concentration. All of the films give high transparency over 80 % in visible range. From the transmittance data, optical band gap of deposited ZnO was calculated to be ~3.30 eV. Photoluminescence

result suggested the existing of defect state in Ni-doped ZnO. The resistivity decreases with addition of Ni-doping until it reaches an optimum level at 1.7 x 10^{-1} Ω cm. The conductivity of Ni-doped ZnO has improved from 0.28 to 5.87 Sm^{-1}; this is 20 times higher than pure ZnO. Further analysis on electrical properties with different temperature has been performed, where the activation energy obtained increases with Ni-doping.

ABSTRAK

Akhir-akhir ini, zink oksida (ZnO) telah menarik banyak tumpuan kerana bersifat serbagunanya dalam pelbagai bidang semikonduktor. ZnO yang berstruktur wurzite mempunyai jurang tenaga yang lebar iaitu 3.3 eV dan mempunyai tenaga ikatan pengujaan yang sangat besar dalam suhu bilik iaitu 60 meV. Oleh yang demikian, ia punyai nilai komersil dalam peranti optoelektronik. Beberapa ciri menarik bahan ini adalah tidak bertoksik, murah, lutsinar dalam julat cahaya tampak, dan bersifat konduktif elektrik. Ini menjadikan ia sangat berpotensi dalam pelbagai kegunaan optoelektronik. Walau bagaimanapun, filem nipis zink oksida secara tulennya mempunyai kerintangan yang tinggi kerana kepekatan caj pembawa yang rendah. Untuk mengatasi masalah ini, dan meningkatkan kekonduksian, zink oksida selalunya didop dengan bahan asing yang boleh menambahkan kepekatan pembawa dan/atau menambah pergerakan caj pembawa. Dalam penyelidikan ini, filem nipis ZnO berjaya dihasilkan dengan menggunakan kaedah salutan putaran sol-gel. Zink asetat dihidrat digunakan sebagai prekursor zink, dan nikel (II) asetat tetrahidrat digunakan sebagai sumber pendopan nikel. Larutan disediakan dengan melarutkan zink asetat dihidrat dan nikel (II) asetat di dalam etanol, seterusnya dietanolamina (DEA) ditambah sebagai agen pengkelat. Filem nipis dihasilkan dengan kaedah salutan putaran di atas substrat kaca. Filem-filem melalui pra-rawatan haba dengan suhu 300 °C selama 10 minit, dan pasca rawatan haba dalam suhu 500 °C selama satu jam. Kesan pendopan nikel terhadap ciri struktur, morfologi permukaan, optik, pendarkilau, keelektrikan, dan struktur elektronik filem nipis zink oksida telah dikaji. Telah didapati bahawa tiada perubahan terhadap pola belauan x-ray pada semua filem-filem nipis, dan tiada puncak-puncak yang menandakan kewujudan logam zink, nikel atau nikel oksida. Ini menunjukkan ion nikel (Ni^{+}) telah menggantikan atom Zn yang menyebabkan tiada perubahan dalam ciri struktur. Imej-imej mikroskop medan pelepasan imbasan

electron (FESEM) menunjukkan filem-filem nipis tersebut mempunyai permukaan yang licin dan rata, dengan saiz butiran sekitar 50 - 70 nm sedikit berbeza dengan kepekatan nikel. Kesemua filem nipis memberikan kelutsinaran yang tinggi melebihi 80% dalam julat cahaya tampak. Daripada data transmitans, jurang tenaga optik ZnO yang dikira ialah ~3.30 eV. Hasil penciriann kefotopendarcahayaan mencadangkan wujudnya kecacatan dalam jurang tenaga zink oksida terdop nikel. Kerintangan filem ZnO berkurang dengan penambahan nikel sehingga mencapai satu tahap optima pada 1.7×10^{-1} Ω cm. Kekonduksian zink oksida terdop nikel bertambah daripada 0.28 kepada 5.87 Sm^{-1}; peningkatan ini adalah 20 kali ganda berbanding dengan zink oksida yang tulen. Analisis lanjut ciri elektrik terhadap perubahan suhu telah dilakukan, dan didapati tenaga pengaktifan bertambah dengan pendopan nikel.

ACKNOWLEDGEMENTS

To begin with, first and the foremost I would thank Allah for giving me strength and good health to keep moving on and accomplish this research thesis. I would love to acknowledge some peoples that really did great helps during these years.

First of all, I like to express my deepest gratitude to my supervisor, Prof. Dr Wan Haliza Abd. Majid for her guidance, supports, advices and patience throughout this research work, especially during thesis writing.

I also would like to thank some peoples that dedicated their time helping me solving anything that came through especially Mr. Mohd Arif Mohd Sarjidan, Mrs. Nor Khairiah Za'aba, Mrs. Rehana Razali, Miss Noor Azrina Talik and all friends, lecturers and staffs in Low Dimensional Material Research Centre (LDMRC) of Physics Department, University of Malaya.

Finally, I am deeply grateful to my parents; Basri Baharin and Miskiah Yunus for their loves and supports, my sisters and brothers, and to all of my family that are always be there, supporting me through ups and downs.

THANK YOU

TABLE OF CONTENTS

LIST OF FIGURES

LIST OF TABLES

LIST OF SYMBOLS AND ABBREVIATIONS

α	:	Absorption coefficient
E_a	:	Activation energy
Al	:	Aluminum
Sb	:	Antimony
E_g	:	Band gap energy
E_B	:	Binding energy
θ_B	:	Bragg diffraction angle
CVD	:	Chemical vapor deposition
DEA	:	Diethanolamine
σ	:	Electrical conductivity
e	:	Electronic charge
EDX	:	Energy dispersive x-ray
λ_{ex}	:	Excitation wavelength
FESEM	:	Field emission scanning electron microscope
FWHM	:	Full width at half maximum
β	:	Full width at half maximum of Bragg diffraction angle
Au	:	Gold
HR-TEM	:	High resolution transmission electron microscope
ITO	:	Indium tin oxide
E_K	:	Kinetic energy
MOVPE	:	Metalorganic vapor phase epitaxy
MEMS	:	Microelectromechanical systems
ε	:	Micro-strain
μ	:	Mobility

MBE	:	Molecular beam epitaxy
MEA	:	Monoethanolamine
Ni	:	Nickel
NAT	:	Nickel acetate tetrahydrate
NiO	:	Nickel oxide
NZO	:	Nickel-doped zinc oxide
OLED	:	Organic light emitting diode
O	:	Oxygen
O_i	:	Oxygen interstitial
V_O	:	Oxygen vacancy
PES	:	Photoelectron spectroscopy
PL	:	Photoluminescence
hv	:	Photon energy
PLD	:	Pulsed laser deposition
n	:	Refractive index
ρ	:	Resistivity
R_S	:	Sheet resistance
NaCl	:	Sodium chloride
SMU	:	Source measurement unit
SAW	:	Surface-acoustic wave
TC	:	Texture coefficient
t	:	Thickness
TFT	:	Thin film field effect transistor
TCO	:	Transparent conductive oxide
UPS	:	Ultraviolet photoelectron spectroscopy
λ	:	Wavelength

XRD	:	X-ray diffraction
XPS	:	X-ray photoelectron spectroscopy
Zn	:	Zinc
ZAD	:	Zinc acetate dihydrate
Zn_i	:	Zinc interstitial
ZnO	:	Zinc oxide
V_{Zn}	:	Zinc vacancy

LIST OF APPENDICES

CHAPTER 1: INTRODUCTIONS

1.1 Zinc oxide

Zinc oxide (ZnO) is a II-VI semiconductor with a hexagonal wurtzite structure. It has a wide band gap of 3.3 eV, large exciton band energy (60 meV) and high optical transparency at room temperature where normally taken to be in range from 20 to 27 °C (Bae et al., 2001; Shim et al., 2002). These properties are mainsprings to the research on zinc oxide as a prospective semiconductor material in light emitting devices, and transparent and/or high temperature electronics (Nomura et al., 2003). ZnO is normally an n-type due to its intrinsic structural defects from the growth process; such as vacancies, interstitial, and anti-sites defects. These defects are formed when an atom is missing from the position that ought to be filled in the crystal. An anti-site is an atom of one species occupies a lattice site that is typically occupied by another species. Vacancy is an unoccupied lattice site, and interstitial defect occurs when an atom does not occupy a lattice site and perturbing the periodic potential that give rise to the ideal band structure. Based on the properties of ZnO; a wurtzite structure semiconductor with wide band gap, and large exciton binding energy, a comparison with other popular wide band gap semiconductors is presented in the Table 1.1.

Table 1.1: Comparison of the properties of ZnO and other wide band gap semiconductors (Hamid, 2009).

Material	Structure	Lattice constants (Å)		Bandgap at RT (eV)	Cohesive Energy (eV)	Melting point (K)	Exciton binding energy (meV)
		a	c				
ZnO	wurtzite	3.249	5.207	3.37	1.89	2248	60
ZnS	wurtzite	3.823	6.261	3.80	1.59	2103	39
ZnSe	zinc blende	5.668	-	2.70	1.29	1793	20
GaN	wurtzite	3.189	5.185	3.39	2.24	1973	21

Research on zinc oxide has been started as early as 1912, and its semiconducting properties are systematically investigated since the beginning of invention of transistors

(Bardeen & Brattain, 1948). After the discovery of a good piezoelectric properties of zinc oxide in 1960, the first electronic application of zinc oxide was as a thin layer in surface acoustic wave devices (Hickernell, 1976; Hutson, 1960). Now, research on zinc oxide as a semiconducting material has been revived after intensive research periods in the 1950s and 1970s (Klingshirn et al., 2005). Since 1990, there was a huge increment in the number of academic publications on ZnO as shown in the Figure 1.1.

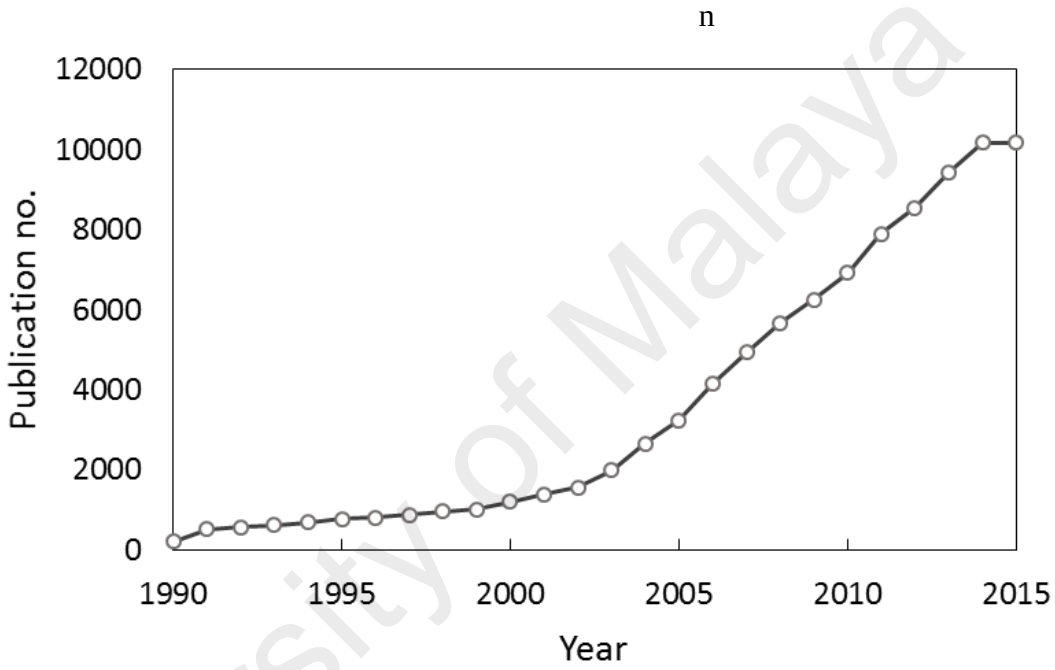

Figure 1.1: Increase of the number of publications about zinc oxide (ZnO) over the last 25 years according to the literature data base Web of Science (WoS).

The ZnO thin film can be prepared by a variety of techniques such as magnetron sputtering (Ondo-Ndong et al., 2003; Ono et al., 1978), chemical vapour deposition (CVD) (Tiku et al., 1980), metalorganic vapour phase epitaxy (MOVPE) (Ma et al., 2004), sol-gel processing (Bao et al., 1998), spray pyrolysis (Bian et al., 2004) and pulsed laser deposition (PLD) (Agura et al., 2003). Of these methods, the sol-gel technique is relatively simple and easy, the stoichiometry can be controlled over large area, low process temperature, and very low in cost.

1.2 Motivations

In application of transparent conductive oxide, indium tin oxide (ITO) is commonly used. However, due to the highly demand application of ITO materials, the indium source become limited and the cost of the material increases. These factors forcing scientist and researchers to search an alternative for ITO. Among the alternatives, ZnO have attracted the most attention because of its non-toxicity compared to ITO, and it is inexpensive due to abundant resources of ZnO. Other than that, ZnO thin film is also transparent in visible region, electrically conductive with metal dopant and can be fabricated by a simple and cheap solution process method.

1.3 Problem statement

Generally, magnetron sputtering is considered an optimum method in preparing zinc oxide thin film. But, it is complex and an expensive vacuum technique if it is to be applied to a large area coating. A deposition technique that easily can be applied to overcome this limitation is sol-gel spin coating technique. Sol-gel as a wet-processing method has a lot of parameters that need to be controlled carefully. Of those parameters are the chemical system (precursors, solvents, and additives), the coating methods, thicknesses, the substrates, and pre/post-heat treatments. All these factors have a distinct effect on the thin film structure if not carefully controlled.

The resistivity of ZnO thin film can be varied widely from ~10^{-2} to 10^{8} Ω cm. Naturally, pure ZnO has low carrier concentration which results in high resistivity. In order to increase the carrier concentration, most research in the area has suggested to control the oxygen vacancies and/or introduce a suitable metal doping to the pure ZnO. Therefore, the conductivity of ZnO can be improved.

1.4 Research Objectives

In this research, there are several objectives need to be done in order to counter the problem stated in previous section;

1. To fabricate zinc oxide thin film with nickel-doping by using sol-gel spin coating technique.
2. To characterize optical, structural and electrical properties of the ZnO thin film for transparent electrode application.
3. To investigate the influence of nickel doping to the structural, optical and electrical characteristic of ZnO thin film

1.5 Dissertation Outlines

This dissertation outlined with chapters each titled as in the heading of every chapter as introduction, literature review, experimental details, structural and morphological analysis, optical and electrical studies, and conclusions. The results and discussion in this dissertation is presented in two consecutive chapter. These chapters are related to the studies on structural, morphological, optical and electrical properties of zinc oxide thin films with addition of nickel doping.

Chapter 2 reviews literature works and theories related to this work. Subtopics begin with an introduction to zinc oxide and its general properties including structural, electrical and optical. Synthesis methods and applications for both zinc oxide nanoparticles and thin films were also reviewed in this chapter.

In Chapter 3, the experimental methods involved in the research work are explained. The chapter begins with the preparation of the precursor solution, fabrication and treatment of zinc oxide thin films and the characterizations involved.

Chapter 4 contains experimental results on the structural of deposited zinc oxide thin films by sol-gel spin coating. Results including X-ray diffractograms, field emission scanning electron microscope (FESEM) and high resolution transmission electron microscope (HR-TEM) images, and EDX analysis. Effect of transition metal doping (nickel) on structural and stoichiometry of deposited ZnO is discussed in this chapter.

Chapter 5 generally presents results on optical and electrical behavior of ZnO and Ni-doped thin films. The effect of nickel doping on the optical transparency, absorbance, reflectance, band gap and refractive index are investigated. Electrical behavior with nickel doping has also been studied and discussed in this chapter by evaluating resistivity, conductivity and activation energy of the thin films.

Chapter 6 concludes the thesis, outlines main findings and proposes suggestion for future works related to this research project.

CHAPTER 2: LITERATURE REVIEW

2.1 Introduction

Zinc oxide (ZnO) has attracted many attentions recently due its versatility in various semiconductor fields with its unique physical and chemical properties such as high chemical stability, high electrochemical coupling coefficient, broad range of radiation absorption and high photostability (Lou et al., 1991; Segets et al., 2009). ZnO is a semiconductor in group II-VI with a wide energy band gap energy (3.3 eV), very large excitation binding energy (60 meV), and high thermal and mechanical stability at room temperature. Thus, these properties make it a commercially valuable in electronics, optoelectronic applications and laser technology (Bacaksiz et al., 2008; J. Wang et al., 2005). While, the piezo- and pyroelectric properties of ZnO promise potential application as a sensor, converter, energy generator and photocatalyst in hydrogen production (Chaari & Matoussi, 2012; Wang, 2008).

In this chapter, an overview of several topics is provided to describe general properties of ZnO including the structure, optical, electrical and magnetic properties. Review on the synthesis techniques and applications of ZnO is also been covered in this chapter.

2.2 Zinc Oxide Structure

ZnO belongs to the II-IV group of binary semiconductors compound. There are three types of zinc oxide crystal structure that can be produced; wurtzite, zinc blende, and rocksalt (Figure 2.1) and the most stable is hexagonal wurtzite structure.

The wurtzite structure in Figure 2.1(c) is an example of a hexagonal close packed (hcp) crystal system consists of tetrahedral coordinate Zn and O atoms with a basic unit cell parameters: a = 3.252 Å and c = 5.213 Å at room temperature (20 to 27 °C). These parameters are temperature dependent where Karzel et al (Karzel et al., 1996) reported at 4.2 K temperature, a = 3. 2496 Å and c = 5.2042 Å. The two sublattices are displaced along c-axis with the distance b as the nearest neighbor distance.

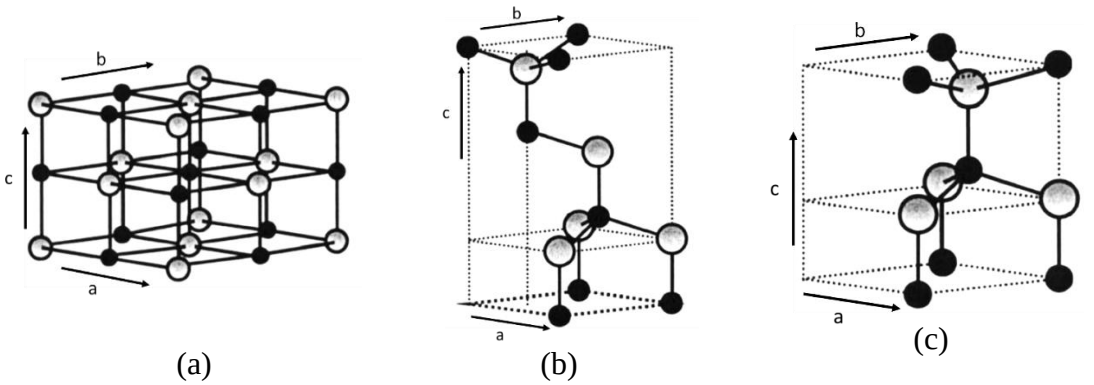

(a) (b) (c)

Figure 2.1: ZnO crystal structures: (a) rock-salt, (b) zinc blende, and (c) wurtzite, O atoms: black spheres and Zn atoms: gray spheres (Özgür et al., 2005).

Besides hexagonal wurtzite structure, ZnO cubic zinc blende structure can also be observed when grown on the cubic structured substrate. A metastable cubic phase rocksalt structure of ZnO is also known to grow on a relatively higher pressure (Özgür et al., 2005) as shown in Figure 2.2. Decremps et al., 2000 measured the shrinking of lattice cell of hexagonal ZnO up to a hydrostatic pressures of 11 GPa, while Desgrenier, 1998 extended his measurements even up to 56 GPa. The temperature-pressure phase diagram is shown in Figure 2.2, where at a pressure of 9.8GPa (at 300 K) a phase transition to the cubic phase of ZnO that exhibits the rocksalt (NaCl) structure occurs. Upon decreasing the hydrostatic pressure this phase transition is reversible in the pressure range from 2–6 GPa, depending on temperature. This means that in contrast to an earlier observation, the high pressure phase is not metastable at normal pressure. In this research, pressure is fixed at ambient, and annealing temperature was set at 500 °C. Thus, the expected structure for deposited ZnO thin film is hexagonal wurtzite.

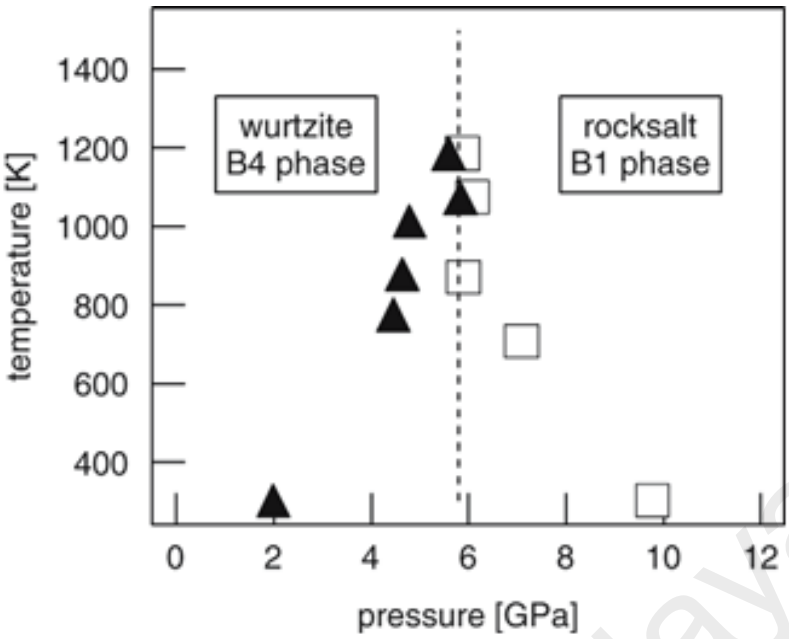

Figure 2.2: Phase diagram of ZnO: the squares mark the wurtzite (B4) – rocksalt (B1), the triangles the B1–B4 transition (Decremps et al., 2000).

2.3 Electrical properties

Electrical resistivity is a property that quantifies how strong a material opposes the flow of electrical current. This is a reciprocal property to electrical conductivity. Resistivity, ρ where denoted by,

$$\rho = \frac{1}{Ne\mu} \tag{2.1}$$

is determined by carrier concentration (N) and carrier mobility (μ) as the electronic charge (e) is a constant. Therefore, in order to achieve a low resistivity, carrier mobility and concentration should concurrently maximized. Most of research in the area suggested oxygen vacancies and doping to maximize the carrier concentration of ZnO thin film.

Vacancy is an unoccupied lattice site (inside the blue square in Figure 2.3), resulting in unfulfilled bonds within the lattice. Oxygen vacancies can be formed by controlling the substrate temperature or ambient oxygen pressure. If an oxygen vacancy is created in a perfect crystal, two electrons are created in the crystal and contributed as ionized donors. But, if there is too much oxygen created in the thin films, suboxides will form, causing the resistivity to rise (Lin, 2010).

Other than the oxygen vacancies, doping also can possibly improve the electrical conduction of metal oxide semiconductor. Host cations are substituted with higher valence electron element. This is to avoid charge neutrality when extra electrons are created as it substitute the host cation with higher valence element.

Pure zinc oxide film naturally has a high resistivity characteristics because of low carrier concentration. In order to improve the conductivity, we can either increase the carrier concentration or increase the carrier mobility in zinc oxide thin films. Higher carrier concentration could be obtained by oxygen and/or zinc non-stoichiometry, or doping with impurity. Even though non-stoichiometry films have good electrical and optical properties, they may become unstable when the ambient temperature becomes higher (Lin, 2010). Thus, doping zinc oxide thin film with impurity is a better approach to increase the carrier concentration and obtain a stable low resistivity ZnO thin film.

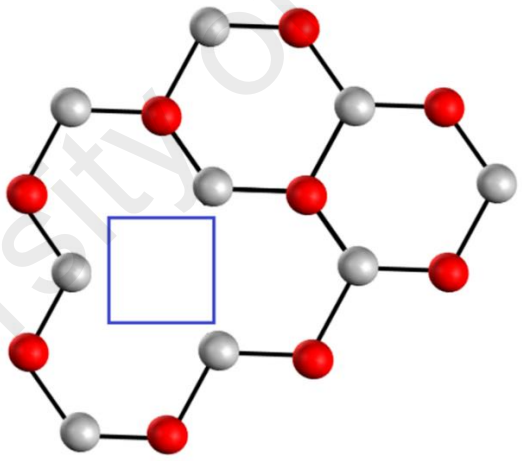

Figure 2.3: Illustrated top view of an oxygen vacancy on ZnO (100) surface.

Commonly in achieving a low resistivity ZnO thin film, researchers focus on increasing the free carrier concentration in the thin film by doping or oxygen vacancies likewise in this research, deposited ZnO thin films were doped with a transitional metal element, nickel.

2.4 Optical Properties

Generally when light is radiated into one medium to another, some of it will be transmitted, some will be absorbed and some will be reflected at the surface interface. However, the intensity of the incident light, I_0 on the surface must equal to the summation of intensities transmitted, absorbed and reflected light. This can be written as,

$$I_0 = I_T + I_A + I_R \tag{2.2}$$

or in alternative form,

$$1 = \frac{I_T}{I_0} + \frac{I_A}{I_0} + \frac{I_R}{I_0} \tag{2.3}$$

where (I_T/I_0) is the transmissivity, (I_A/I_0) is the absorptivity and (I_R/I_0) is the reflectivity. Therefore, transparent material will transmit light more than that to be absorbed and reflected.

In explaining optical phenomena within solid material such as ZnO thin films, several interactions between electromagnetic radiation and atoms, ions, and/or electron are involved and the most important are electronic polarization and energy transitions. Theoretically, light absorption in nonmetallic/semiconducting materials is explained by two basic mechanisms, which also influence the transmission characteristics of these nonmetals. One of the mechanism is electronic polarization. However, absorption by electronic polarization is important only at light frequencies in the vicinity of the relaxation frequency of the constituent atoms. Another mechanism of absorption involves valence band-conduction band electron transitions, which depends on electronic band structure of the materials, for instance ZnO thin film depends on semiconductor band structure.

Figure 2.4 shows a photon absorption for nonmetallic materials where an electron is excited across the band gap, leaving behind a hole in the valence band. The energy of the photon absorbed E, essentially greater than the band gap energy E_g. This describing the

absorption occurrence by excitation of an electron from the nearly filled valence band, across the band gap, and into an empty state within the conduction band. A free electron in the conduction band and a hole in the valence band are created.

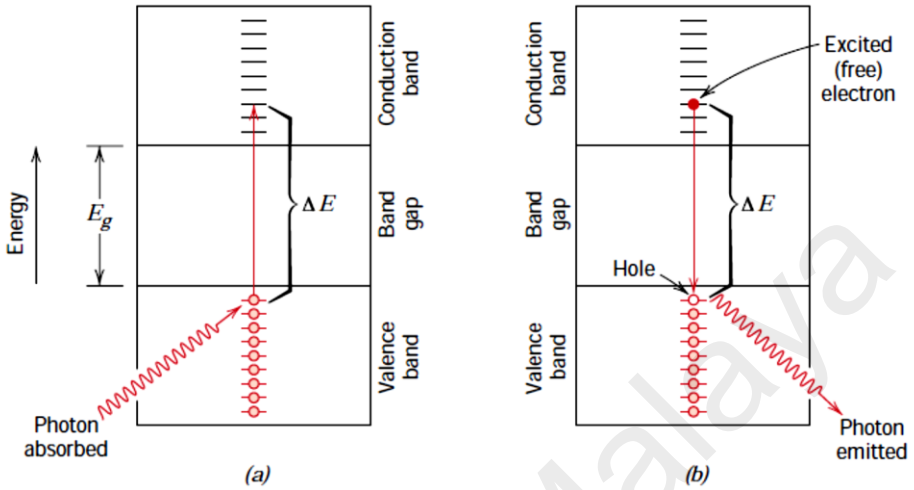

Figure 2.4: (a) Mechanism of photon absorption for nonmetallic materials and (b) emission of a photon of light by a direct electron transition across the band gap (William D Callister & Rethwisch, 2013).

The energy of excitation E is related to the absorbed photon frequency through based on transitions equation:

$$\Delta E = hv \tag{2.4}$$

Thus, if only the photon energy is greater than the band gap E_g then excitations with the accompanying absorption can take place. This can be denoted by:

$$hv > E_g \tag{2.5}$$

In contradiction, metallic materials which described in Figure 2.5, have no band gap thus every photon has an adequate energy to excite electrons into a higher energy unoccupied state. Compared to semiconductors like ZnO thin films, the absorption phenomenon occurs when the energy of the photon in some range of wavelength is greater than E_g. By manipulating the relation in Equation 2.5 in term of wavelength, λ maximum band gap energy E_g(max) to absorb visible light (400 to 700 nm) is just 3.1 eV. Thus, any nonmetallic materials that have band gap energies more than 3.1 eV will not absorb

visible light. Additionally, these materials with high purity will appear transparent and colorless.

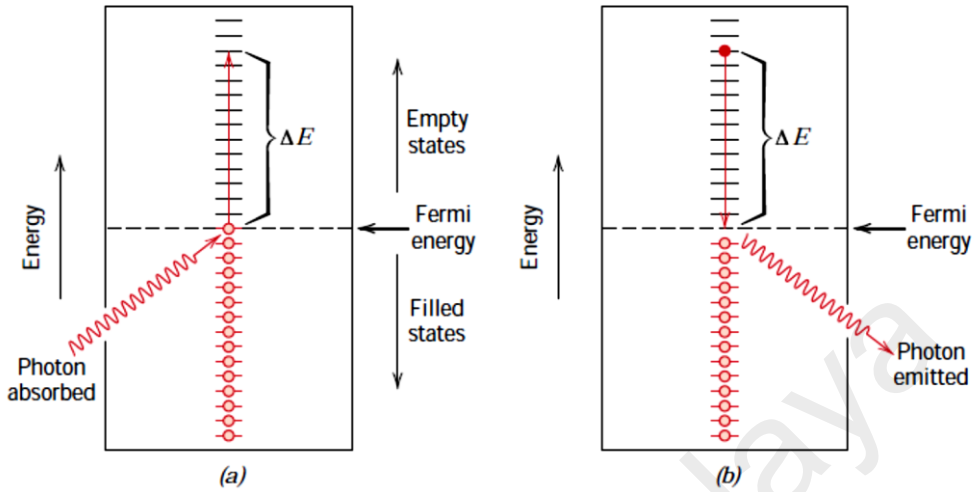

Figure 2.5: (a) Schematic representation of the mechanism of photon absorption for metallic materials in which an electron is excited into a higher energy unoccupied state and (b) reemission of a photon of light by the direct transition of an electron from a high to a low energy state (Callister & Rethwisch, 2013).

From transmittance and reflectance information of the materials, absorption coefficients of the films at different wavelength can be calculated with the following relation,

$$\alpha = \frac{1}{t} \ln \frac{(1-R)^2}{T} \tag{0.6}$$

where *t* is the film thickness, *T* is the transmittance and *R* is the reflectance. Furthermore, the absorption coefficient can be related to the band gap energy, E_g as:

$$\alpha h\nu \approx (h\nu - E_g)^{\frac{1}{2}} \tag{0.7}$$

where *hν* is the photon energy (Tauc et al., 1966).

2.5 Deposition techniques of zinc oxide thin film

There are variety of techniques to deposit ZnO thin film. Generally, depositing high quality and uniform thin films have been an intensive area of research yielding many deposition techniques and each technique falls into one of three broad categories: physical vapor deposition (e.g. magnetron sputtering, molecular beam epitaxy and pulsed laser

deposition), chemical vapor deposition, and wet chemical deposition (e.g. sol-gel depositions and spray pyrolysis deposition). Different technique results different film growth, crystallinity (single crystal, poly crystalline or amorphous), substrate interaction (adhesion) and morphology (Smith et al., 1992). Thus, a selection of deposition technique is essential to control over the properties of the resultant films. In this section, a few techniques of depositing ZnO thin film are briefly reviewed.

2.5.1 Magnetron sputtering

Planar magnetron sputtering has been invented in early 1970s (Ellmer, 2000). It is one of the most versatile used for the deposition of transparent conducting oxides (TCO) generally. In sputtering technique, mechanism start with gaseous plasma in the deposition chamber, then ions from the plasma are accelerated onto the Zn or ZnO target. With the energy transfer and molecules of the arriving ions, atoms/particles from the Zn or ZnO target are ejected to substrate. As a result, substrate which placed in the path of these atoms/particles is coated with ZnO thin film (Figure 2.6).

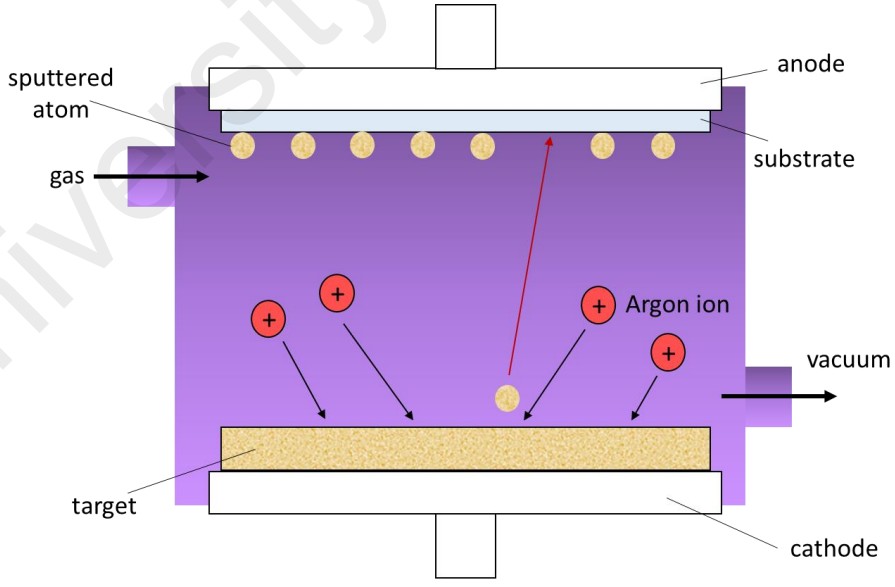

Figure 2.6: Illustration of basic sputtering deposition mechanism.

Even though sputtering is one useful technique to deposit thin films, there are two main drawbacks of this technique which are it has relatively slow deposition rate and the

electron bombardment on the substrate is extensive, causing overheating and structural damage. Thus, the magnetron sputtering was developed to deals with these issues simultaneously by using magnet behind the cathode to trap the electrons in magnetic field above Zn or ZnO target surface (Figure 2.7). Trapped electrons form curved paths in the magnetic field enhancing their probability of ionizing a neutral gas molecule. This significantly increases the erosion rate of target material to be deposited on to the substrate.

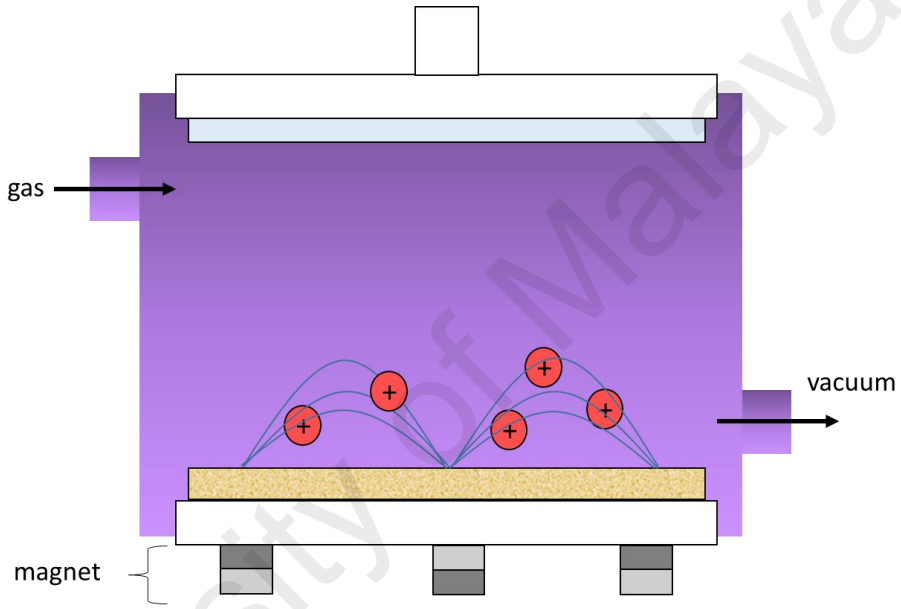

Figure 2.7: Illustration of magnetron sputtering deposition mechanism.

This magnetron sputtering technique has advantages such as low substrate temperature, good adhesion of films on substrates, very good thickness uniformity and high density of the films, good controllability and long-term stability of the process, able of forming many compounds from element (metallic) targets and relatively cheap deposition method compared to other thin films deposition method such as evaporation, chemical vapor deposition (CVD) or spray pyrolysis (Ellmer, 2000).

2.5.2 Molecular beam epitaxy (MBE)

In 1970, molecular beam epitaxy (MBE) method was developed to produce a high-purity epitaxial layer of compound semiconductors (Cho, 1971). Deposition by MBE is performed in high vacuum or ultrahigh vacuum (10^{-8} Pa), clean, low pressure conditions where the potential for contamination is minimized. MBE can produce high quality layers with abrupt interface and good control of thickness, doping and composition because of its excellent control capability. It is a valuable tool in the development of sophisticated electronic and optoelectronic devices.

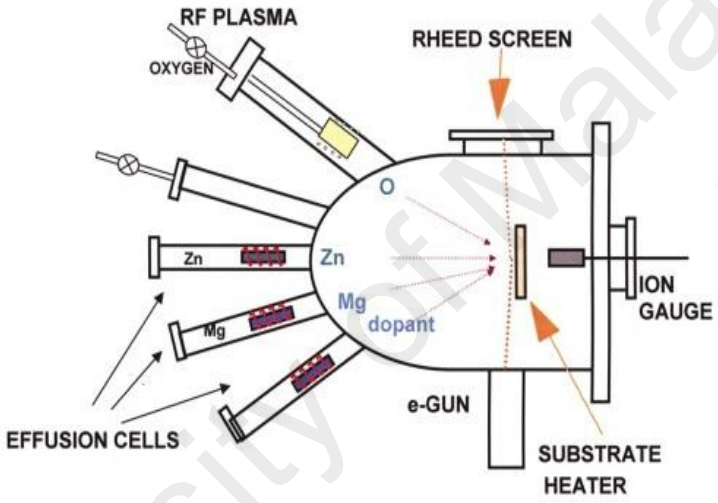

Figure 2.8: Schematic diagram of an MBE system (Zhang, 2004).

Film formation is by evaporation of elemental materials from cylindrical effusion cells. In MBE, the molecular beams are from thermally evaporated elemental sources, and the gaseous elements then condense on the substrates. Substrate is held at an elevated temperature so that arriving source element (for example Zn and O atoms) have sufficient energy to move around on the surface of the substrate and find a precise bonding positions. These evaporated atoms do not interact with each other or with the vacuum chamber gases, until they reach the substrate due to the long mean free paths of the atoms. During deposition, the growth of the crystal layers is monitored by RHEED (Reflection High Energy Electron Diffraction) (Figure 2.8). The computer controls shutters in front

of each source, allowing precise control of the thickness of each layer, down to a single layer of atoms.

2.5.3 Pulsed laser deposition (PLD)

Pulsed laser deposition (PLD) is a physical vapor deposition process which using a high-power pulsed laser beam for an ablation of the solid target material to be deposited. It shares some common characteristics with molecular beam deposition and some with sputter deposition. As shown in Figure 2.9, a focused laser pulse is directed onto target material in a vacuum chamber. The laser pulses heats and vaporizes target surface producing plasma or plume of atoms, ions, atoms and excited species. The vaporized target material in the plasma then deposited as thin film on substrate. Process could occur in either ultra-high vacuum or in the presence of a background gas for example oxygen gas, O_2 specifically when depositing oxides; to fully oxygenate the deposited films.

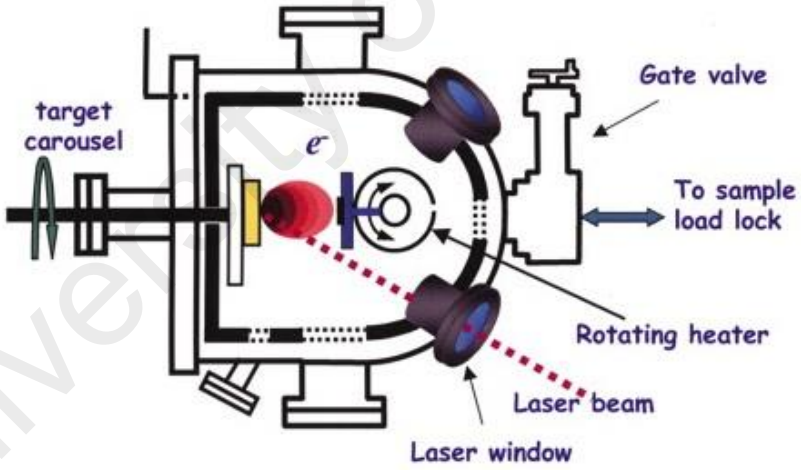

Figure 2.9: Schematic diagram of PLD system (Norton et al., 2004).

This technique possesses several favorable characteristics for growth of multicomponent materials, such as stoichiometric transfer of the target material to the substrate, compatibility with a background gas, and atomic level control of the deposition rate. In this method, oxidation of Zn primarily occurs in the ZnO ablation plasma plume, thus improving the difficulties encountered with MBE of ZnO, where oxidation proceeds via surface reactions.

2.5.4 Chemical vapor deposition (CVD)

Chemical vapor deposition (CVD) is often used in the semiconductor industry to produce thin films. In typical CVD as shown in diagram in Figure 2.10, substrate is exposed to one or more volatile compound of material to be deposited which in the diagram is the ZnO/C mixture, which react and/or decompose on the substrate surface to produce the preferred thin film deposition. Normally, volatile by-products are also produced, which are removed by gas flow through the reaction chamber. CVD differs from physical vapor deposition (PVD), which relies on material transfer from condensed-phase evaporant or sputter target sources. Since CVD processes do not require vacuum or unusual levels of power, they were practiced commercially prior to PVD (Tiku et al., 1980).

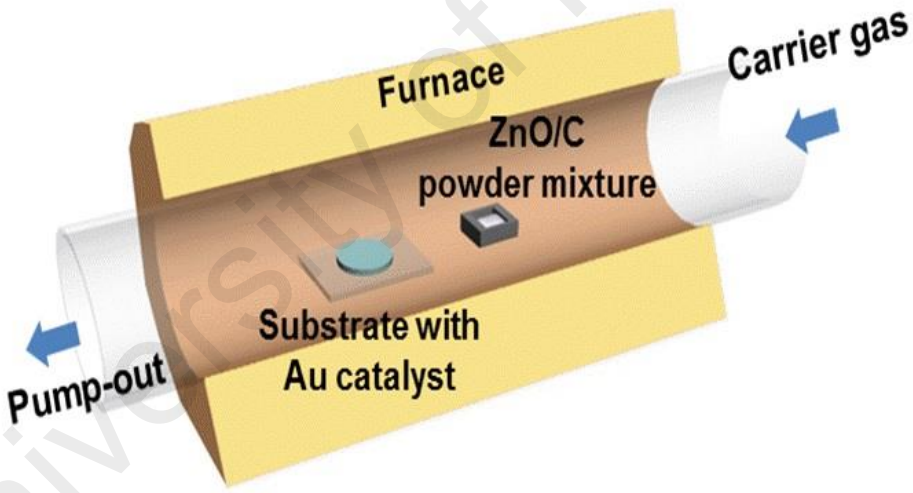

Figure 2.10: Schematic diagram of CVD system (Nanophotonic Semiconductors Laboratory, GIST).

The advantages of using CVD technique are it can be performed as a continuous process which uses relatively low consumption of energy, able to coat complex shapes and surfaces, uniform conformal coatings which are usually chemically bonded to substrate and giving high adhesion. CVD has the ability to control crystal structure, morphology and orientation by controlling the deposition parameters. However, there are few drawbacks of CVD that need to be countered such as carbon contamination from

metalorganic precursors in the films, temperature limitation on substrate compatibility, shelf-life of precursors and the possibility of side reaction.

2.5.5 Spray pyrolysis deposition

Spray pyrolysis is considered a modification of chemical vapor deposition, but by using a fine spray of zinc precursor solution (generated by a spray nozzle using compressed gas) to deliver the zinc precursor to the substrate surface for thermal reaction and film formation.

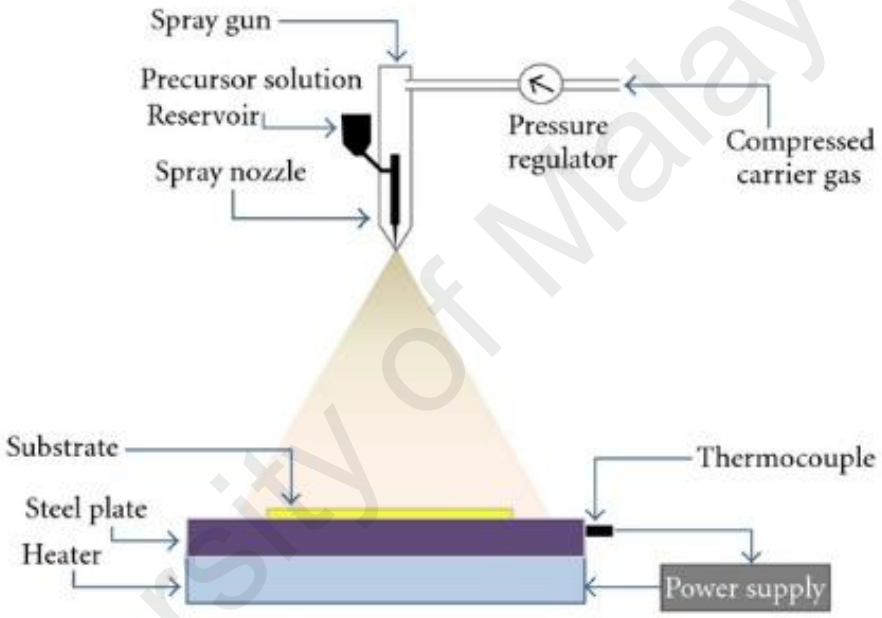

Figure 2.11: Schematic of a spray pyrolysis deposition (Patil et al., 2012).

The spray pyrolysis process consists of spraying fine droplets of the precursor's solution of Zn onto a heated substrate. The droplets undergo thermal decomposition and the reaction results in the designated yield of ZnO thin film. Like the other deposition techniques, the parameters involved need to be controlled to achieve the desired quality of films. Their effects are interdependent and they need to be optimized. The deposition parameters include the substrate nature, nozzle diameter, distance of nozzle to substrate, precursor composition, temperature of substrate during deposition, pressure of carrier gas, solution flow rate, and doping level (Inamdar et al., 2012). Spray pyrolysis is one of the

most attractive film deposition method since the film formation is carried out in air ambient by relatively simpler apparatus.

2.6 Sol gel spin coating technique

Sol-gel synthesis was first widely developed in the 1960s and expanded in mid 1980s in studying perovskite films. Since then, the sol-gel field has expanded to almost any wet chemical route to produce powders and thin films through drying and subsequent heat treatment (Livage et al., 1988; Schwartz, 1997). Generally, sol-gel is a process involving the controlled hydrolysis of dissolved metalorganic precursors followed by a condensation reaction, which resulting in the formation of a three dimensional network of particles (Corriu & Leclercq, 1996; Mitzi, 2001).

Deposition of ZnO thin films by sol gel method is simple, cheap, reliable, repeatable, and have relatively mild synthesis conditions. Sol-gel process, which is also called soft chemistry 'chimie douche' allows elaborating solid material from solution by using sol or gel as an intermediate step at much lower temperature possible. It is widely used technique because this process provides enhanced homogeneity; all precursors are mixed in liquid state, thus homogeneity can be expected on a molecular scale (Pontes et al., 2003). Doping process can easily been done with sol-gel by straightforward dissolving dopant to solution and give a homogenous dopant distribution. Compositional control is also simplified by sol-gel, as precursor stoichiometry is directly reflected in the resulting materials (Das et al., 2000). This is contrast to other method where stoichiometry is controlled trough indirect mechanisms.

ZnO thin film synthesis via sol-gel process involves several parameters such as the nature of precursors and its concentration, type of solvent, type of additive and concentration, aging time of early mixture, coating method, substrates, pre and post heat treatment.

Several precursors have been used such as nitrate, chloride, perchlorate, acetylacetonate and alkoxides such as ethoxide and propoxide, with the most often used is the acetate dehydrate. Metal salts are low-cost, ease of use and commercially available have made them interesting precursors and appropriate for large-scale applications. Two types of metal salts are inorganic salts (e.g. nitrate, chloride, sulfate etc.) and organic salts (e.g. acetate). Inorganic salts main drawback is the inclusion or difficult removal of anionic species in the final product (Armelao et al., 2001; Guglielmi & Carturan, 1988). Comparing to organic salt; acetate, the contaminants of the gel from the acetate group decomposed under annealing and producing combustion volatile by-products (Armelao et al., 2001). In brief, organic salts precursors in alcoholic media is beneficial because of low cost and the facility of metal salt use in general, and they also could avoid problems presented by certain inorganic anions and the washing steps (Znaidi, 2010).

In order to dissolve the metal salts, the solvent must have a relatively high dielectric constant (Hosono et al., 2004; Hu et al., 2000; Sun et al., 2007). Alcohols with low carbon number are the most used solvents: methanol, ethanol, 1-propanol, 2-propanol, 1-butanol and 2-methoxyethanol. Hosono et al., 2004, made a comparative study on chemical reactions from zinc acetate dehydrate to ZnO using different types of alcoholic solvents, i.e. methanol, ethanol, and 2-methoxyethanol. Zinc acetate dehydrate (ZAD) was more soluble in methanol than in ethanol or 2-methoxyethanol according to dielectric constants of these alcohols.

Additives are chemical species presenting at least one functional group, they act as base or acid and/or chelating agent. Alkali metal hydroxides, carboxylic acids, alkanolamines, alkylamines, acetylacetone and polyalcohols are example of additives for this purpose. They facilitate the zinc salt dissolution in some alcoholic media, for example zinc acetate dihydrate (ZAD) has limited solubility in alcohols. Agents like ethanolamines

or lactic acid help in complete dissolution and formation of stable sol (Chakrabarti et al., 2004)

Different coating method affects the crystallographic orientation of ZnO films. This was reported by Habibi & Sardashti, 2008 where they observed highly c-axis oriented films with dip-coating method. While for spin-coating deposited films, showed 3 peaks in XRD with high intensity peak at (002) orientation. Selection of deposition speed influence the film thickness. Ilican et al., 2008 reported that the concentration of lattice imperfection increases with chuck rotation rate. Thickness plays role on the degree of orientation. As stated by Fujihara et al., 2001, as the thickness increases, the (002) orientation was preferred and become maximum for the film thickness 260 nm and thin films will become randomly oriented above that.

Amorphous substrate such as glass helps to obtain oriented zinc oxide films along (002) direction as discussed by Chakrabarti et al., 2004. They also reported that less oriented film was obtained when using crystalline substrate such as quartz and silicon substrate. Heat treatment is one of the most important factors in governing film orientation. For pre-heat treatment, the temperature should be higher than the boiling point of the solvent and the additives, and near the crystallization temperature of ZnO. Suitable temperature of 300 ºC is in the case of 2-methoxyethanol and MEA as solvent and additive respectively to produce (002) oriented films (Lee et al., 2003; Ohyama et al., 1997). This temperature is also appropriate for the system consisting of methanol and lactic acid (Bao et al., 1998). For films obtaining from 2-propanol and DEA, the temperature for pre-heat is 100 ºC (Chakrabarti et al., 2004) and another low pre-heat temperature of 80ºC for system of methanol as solvent without any additive (Natsume & Sakata, 2000). Beside, post-heat treatment also should be carefully chosen. For most of systems, temperature ranges of 500-600 ºC appear to be the most appropriate. And above limit in temperature will cause disorientation (Lee et al., 2003; Ohyama et al., 1997).

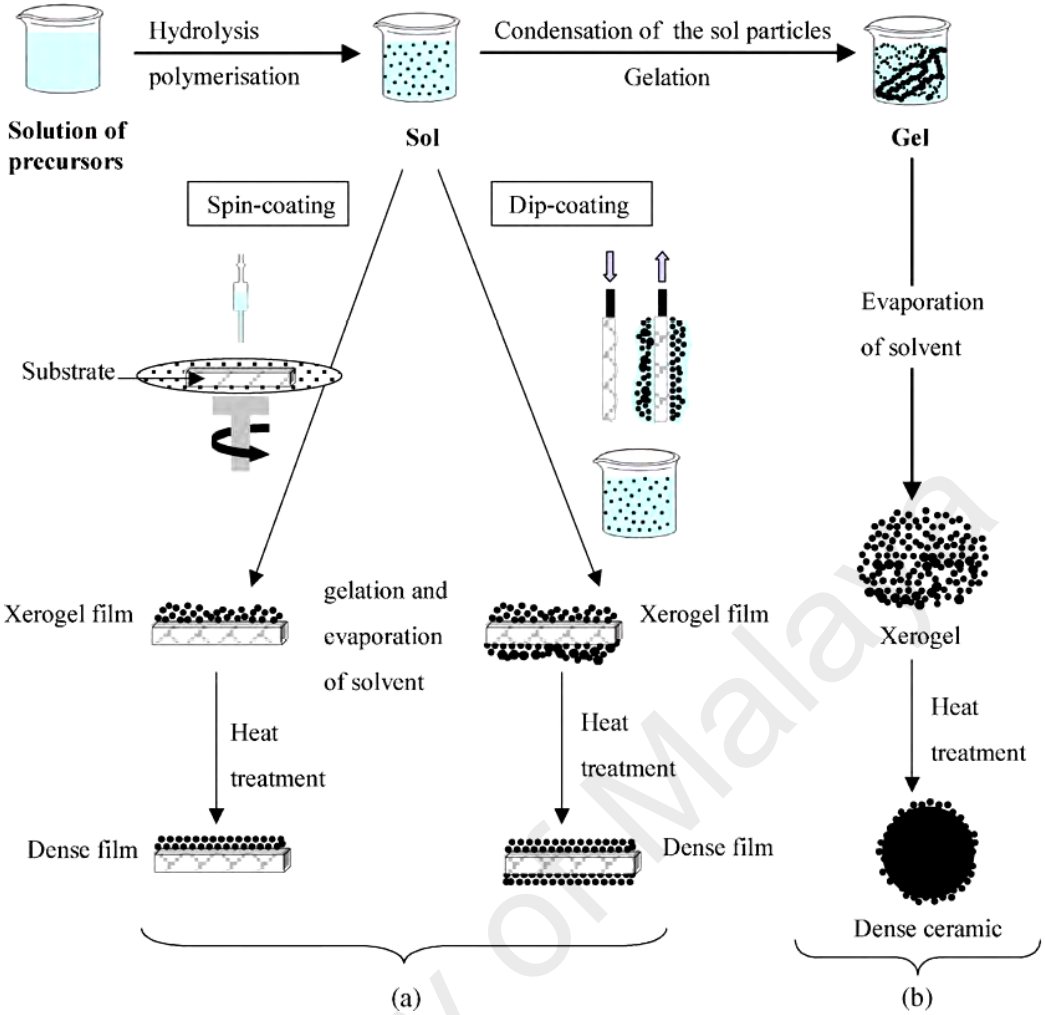

Figure 2.12: Overview of two synthesis examples by sol-gel method: (a) films from colloidal sol and (b) powder from colloidal sol transformed into gel (Znaidi, 2010).

2.7 Application of ZnO

Generally, zinc oxide is a very old technological material. In the early ages, it was produced as a byproduct of copper ore smelting and used for healing wounds. It was also used for the production of brass (Cu-Zn alloy), and this was the major application of ZnO before metallic zinc were replacing the oxide (Brown, 1978). Beginning in the industrial age (mid nineteenth century), ZnO was highly used in white paints, rubber industry where it is used as the activator for vulcanization process, and also used in porcelain enamels.

The electrical properties of ZnO has been investigated since the beginning of semiconductor ages after the discovery of transistor in 1912 (Bardeen & Brattain, 1948). Ever since, there are growing numbers of ZnO applications in electronics. Some of the applications were mentioned in the following sections.

2.7.1 Transparent electrodes

Transparent electrodes are mainly applied in thin film solar cells, and display applications such as organic light emitting diodes (OLED). In thin film solar cells, a transparent window electrode is needed for light transmission and photocurrent extraction. Some configurations used for thin film solar cells are as in the following Figure 2.13,

Highly doped ZnO films are used particularly in amorphous silicon (Rech & Wagner, 1999), and $CuInSe_2$-based cells (Klenk et al., 2005; Ramanathan et al., 2003). Addition of trivalent dopants like boron, aluminum or gallium can give a high doping levels with carrier concentrations up to 1.5×10^{21} cm^{-3} and resistivities as low as 2×10^{-4} Ω cm. The main advantage of zinc oxide is, it is much cheaper than indium oxide, and this is necessary for large technologies like thin film solar cells.

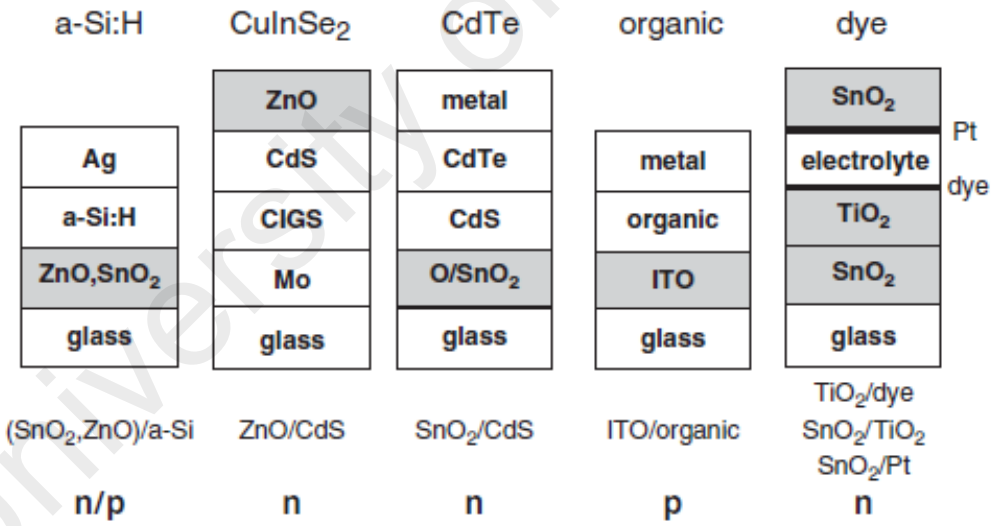

Figure 2.13: Transparent conducting oxide (TCO) electrodes in different types of thin films solar cells with the type of contact is stated at the bottom of each structure along with the doping type of the semiconductor (Ellmer, Klein, & Rech, 2007).

In display technology, ITO is mostly used as the transparent electrode. However, there is a great need in replacing ITO with other materials because of the limitability of indium nowadays. However, ITO still possess higher conductivities compared to other alternatives, and ITO also have the possibility of preparing very flat film and the good

etching behavior enables highly reproducible structure formation. In a liquid crystal display (LCD) which have been used in most flat panel display, the interface between transparent electrode and the polymer layer inserted for orientation of the liquid crystals does not have an active electronic function in the device; it is simply used to transmit light and to apply an electric field for reorientation of the crystals. This is different in OLED, where ITO is almost exclusively used as its anode material (Hung & Chen, 2002). In OLEDs, ITO is used to inject holes into the organic layer to recombine with electron injected from metal cathode. As an alternative to substituting ITO, ZnO also has been tested as electrode material in OLEDs (Jiang, et al., 2003; Park et al., 2005).

2.7.2 Varistors

Varistors are voltage-dependent resistors, which are widely used for over-voltage protection. ZnO varistors were first developed by Matsuoka, 1971 at the beginning of 1970s. They are made from sintered polycrystalline ceramics using different additives such as Bi_2O_3, Sb_2O_3, or other metal oxides. The material is poorly doped and the additives segregate to the grain boundaries during sintering leading to a large barrier for electron transport (Blatter & Greuter, 1986; Rossinelli, et al., 1984)

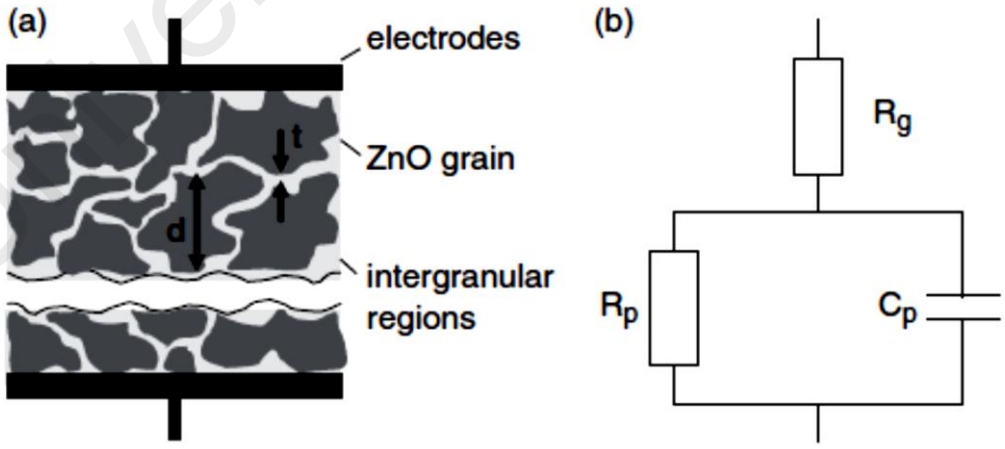

Figure 2.14: (a) Schematic diagram of the microstructure of a varistor, consisting of electrodes, ZnO grain of size d and intergranular region of thickness, *t* and (b) equivalent circuit of a varistor with $\underline{R_g}$ is the grain resistance, R_p and C_p are the parallel resistance and capacitance respectively (Levinson & Philipp, 1986).

A schematic diagram of the microstructure and the equivalent circuit of a varistor are shown in Figure 2.14. In the schematic diagram of the microstructure, it indicates two electrodes, the grain structure and the intergranular regions. The intergranular regions are responsible for the highly nonlinear IV characteristics as it governs the electron transport of varistor. It consists of depletion regions between ZnO grains, constituting electronic barriers for the current transport. Increasing the voltage at the varistor leads eventually to the breakdown of the barriers accompanied by a high current flow.

2.7.3 Piezoelectrics devices

ZnO also has a very high electromagnetic coupling coefficients as a semiconductor. Due to this, there are several ZnO thin film piezoelectric applications such as bulk acoustic wave surface-acoustic wave (SAW) resonators, filters, piezoelectric sensors, and microelectromechanical systems (MEMS) (Ellmer et al., 2007). The most common application is the SAW filter, which has been an important component in mass consumer items such as TV filters, and wireless communication systems.

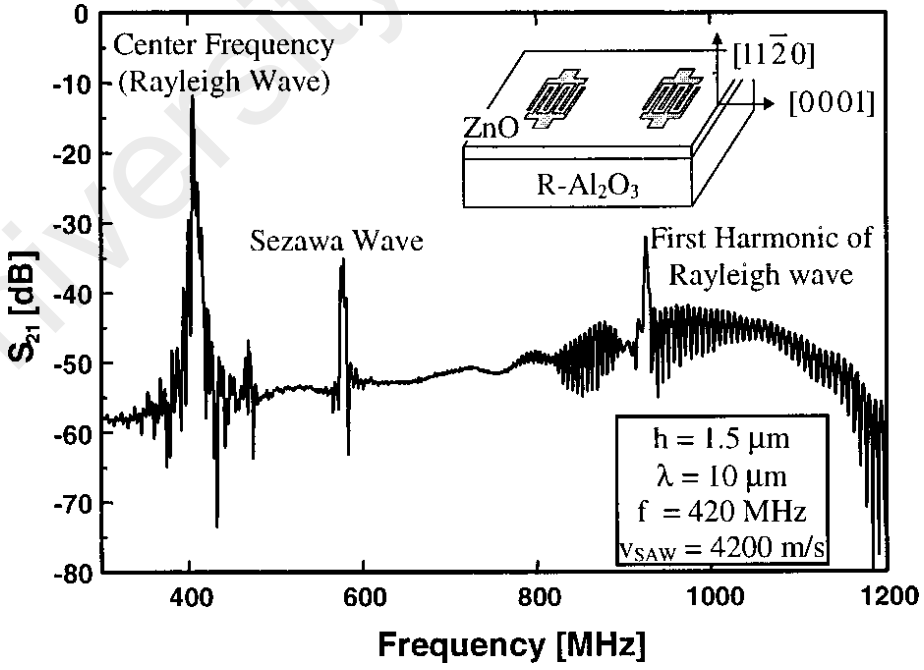

Figure 2.15: Frequency spectrum of a 10 mm wavelength SAW device on a 1.5 μm thick ZnO film and the inset shows the geometry of the fabricated device (Gorla et al., 1999).

In SAW devices, a mechanical deformation is induced by electrical contact fingers in a nearly isolating, highly (0001)-textured ZnO film (referring the insert in Figure 2.15). The insulating wave travels along the ZnO film surface with the velocity of sound in ZnO and is detected at the end of the device by another metal-finger contact. High-frequency electrical signals (10 MHz to 10 GHz) can be transformed to SAWs with typical wave velocities of about 3 kms^{-1}. A frequency curve of an SAW device is shown in Figure 2.15. Comparing to the velocity of light, SAW has much lower acoustic velocity, thus such SAW devices can also be used as acoustic delay lines with a characteristic frequency dependence suitable for high-frequency filters (Ellmer et al., 2007).

2.7.4 Transistors

Zinc oxide has a good crystalline quality even when deposited at room temperature of 20 to 27 °C. Featuring high mobilities of 10^{-50} $cm^2 V^{-1} s^{-1}$ for carrier concentration below 10^{19} cm^{-3}, this is much higher than mobility in amorphous silicon (~1 $cm^2 V^{-1} s^{-1}$) (Ellmer, 2000; Könenkamp, 2000). Thus, ZnO was investigated also as a material for thin film field effect transistors (TFT), which offers the combination of transparent, high mobility TFTs for the next generation of invisible and flexible devices (Thomas, 1997). ZnO shows a better electronics properties, and more stable at ambient conditions compare to organic semiconductors (Carcia et al., 2003). A TFT structure of RF magnetron sputtered ZnO thin film is shown in Figure 2.16 (Fortunato et al., 2005). The structure consists of indium tin oxide (ITO) as the gate electrode, and the gate insulator consists of Al_2O_3/TiO_2 multilayers (thickness 220 nm). Both, the channel layer of undoped ZnO (resistivity $\approx 10^8$ Ωcm) and the source/drain contact layers were deposited by RF magnetron sputtering at room temperature. With threshold voltage of 19 V, such ZnO-TFT could result in saturation mobility of ~27 $cm^2 V^{-1} s^{-1}$. The on/off resistances are about 45 kΩ and 20 MΩ. This example demonstrates that a ZnO-TFT works in principle, even for ZnO films

deposited at room temperature, opening a new field of applications of ZnO as a semiconductor.

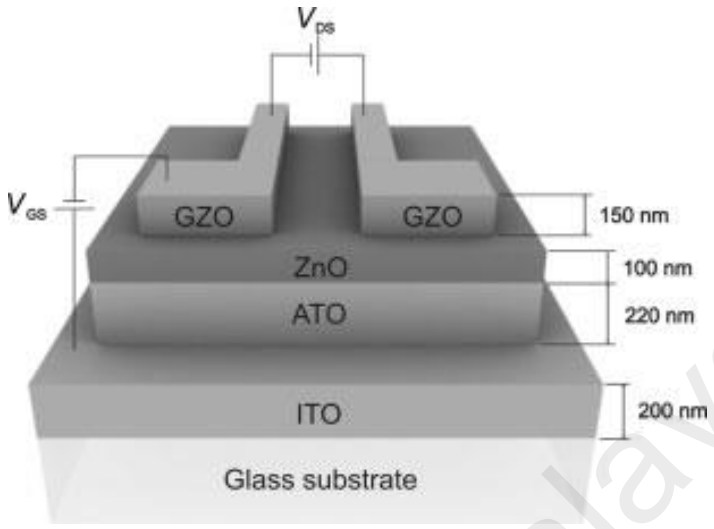

Figure 2.16: Schematic illustration of ZnO-based TFT structure: the gate insulator Al_2O_3 and TiO_2 (ATO) multilayer, while the indium tin oxide (ITO) gate and the gallium-doped zinc oxide (GZO) are source and drain, respectively (Fortunato et al., 2005).

2.8 Summary

The general properties of ZnO including the structure, optical, and electrical properties have been reviewed. Several deposition techniques of zinc oxide thin films have also been summarized. The sol-gel spin coating technique were discussed in detail. A variety of ZnO applications has been presented, especially in the electronic field. Sol-gel spin coating technique was used as the method of deposition in this work because it is simple, cheap, reliable, repeatable, and have relatively mild synthesis conditions. This technique and experimental method involve in this work will be further explained in the next chapter.

CHAPTER 3: EXPERIMENTAL DETAILS

3.1 Introduction

Experimental work of this research including sample preparations and characterizations. This chapter will be explaining and describing the details in the experimental work from cleaning of glass substrate, zinc oxide (ZnO) precursor solution preparation, and the thin films deposition. A simple wet processing method, sol-gel spin coating used to fabricate ZnO thin films will also be explained in detail in this chapter. Various types of characterization techniques used such as surface profilometer, X-Ray Diffraction (XRD), field-effect scanning electron microscopy (FESEM), energy-dispersive x-ray spectroscopy (EDX), X-ray photoelectron spectroscopy (XPS) and high resolution transmission electron spectroscopy (HR-TEM) for physical properties measurement, UV/VIS/NIR and photoluminescence (PL) spectrometer for optical characterizations, and four point probes using Keithley 236 Source Measurement Units (SMUs) and ultraviolet photoelectron spectroscopy (UPS) to characterize their electrical behavior are also described in this chapter.

3.2 Substrate preparation

Glass is used as substrate for the thin films fabrication because of its transparent behavior which is essential for optoelectronics applications. Initially, glass slides were cut using diamond cutter into a size of 25 x 20 mm^2. This size is considerable suitable as it fit nicely on spin coater's chuck. In a beaker, the cut glass pieces were immersed in soap water and placed into an ultrasonic bath for about 20 minutes to remove dust and fine particles that may have adhered on the glass surfaces. The glass substrates were then rinsed thoroughly with distilled water to wash out the soap water from their surfaces. Acetone and ethanol were used to remove the substrates from non-polar and polar type contamination respectively. The substrates were then rinsed with deionized water to minimize the existence of ion molecules on the surfaces as the contamination on the

surface may lead to poor adhesion and as a result produced pinholes in the films (Van Slyke et al., 1996). Finally, the cleaned glass substrates were purged dried with nitrogen.

3.3 Preparation of precursor solution

The doped and undoped zinc oxide thin films were deposited by sol gel spin coating technique. Thus, a precursor solution of zinc oxide was prepared for this process with zinc acetate dihydrate as source of Zn^+ and nickel acetate tetrahydrate as dopant, absolute ethanol was used as solvent and diethanolamine (DEA) as stabilizer.

Figure 3.1: Zn^+ sol with 0 to 5% Ni concentration.

Zinc acetate dihydrate (ZAD) salt were measured and dissolved together with nickel acetate tetrahydrate (NAT) salt in 5 mL absolute ethanol producing Zn^+ precursor sol/solution with Ni^+ dopant. Concentration of the sol was fixed at 0.5 M with the amount of NAT salt used in the solution varied from 0 to 5 mol percentage to ZAD salt. Stabilizer DEA was added to the sol with the ratio of 1:1 to the sol concentration. The details are tabulated in Table 3.1.

Table 3.1: Precursor solution recipe for 0 to 5 percent of nickel dopant.

Sample	ZAD (g)	NAT (g)	DEA (g)
0NZO	0.550	0.000	0.260
1NZO	0.543	0.006	0.260
2NZO	0.538	0.012	0.260
3NZO	0.532	0.019	0.260
4NZO	0.527	0.025	0.260
5NZO	0.521	0.031	0.260

The solution were then stirred using a magnetic stirrer while heated at 60°C for an hour until the solution became clear. Subsequently, the solution was aged for at least 24 hours to form homogenous colloidal solutions as shown in Figure 3.1.

3.4 Deposition of ZnO thin film by spin coating

Nickel-doped zinc oxide (NZO) thin films are deposited by spin coating sol gel technique. Spin coater model used was Laurell WS-650MZ-23NPP as shown in Figure 3.2. The system is connected to a compressed gas tank as it needs high pressure to be operated. Initially, a clean glass substrate was put on top of the spin coater chuck. From the bottom of the chuck, vacuum pump was set to a vacuum down to draw the substrate stick on the chuck and also to prevent the sample from casted out during the spin coating process. The instrument itself has been set with precautions such that it cannot be operated until the vacuum pressure is sufficient to keep the sample stable on the sample holder.

Approximately 150 μL of the precursor solution dripped onto the center of the substrate by using micro syringe. The substrates were then spun at speed of 3000 rpm and dwelling for 20 seconds. This spinning disperse and spread the sol over the substrate by centrifugal force forming thin film on top of the substrate. The thin films were then preheated at 200 °C on hot plate for 5 minutes as shown in schematic diagram in Figure 3.3 in order to evaporate solvents and remove any organic residual. After the pre-heat treatment, the step 1 to 3 as shown in Figure 3.3 were repeated for five times to get

film thickness in the range 300 to 400 nm. Finally the thin films were annealed at 500 °C in a furnace for an hour.

Figure 3.2: Laurell WS-650MZ-23NPP spin coater in 10k clean room environment.

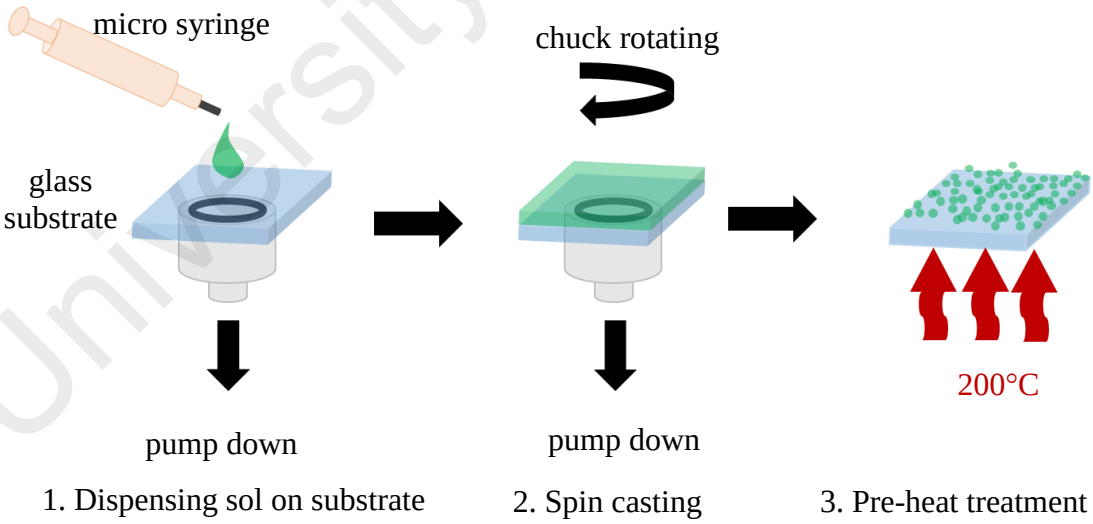

Figure 3.3: Schematic diagram of spin coating process.

3.5 Characterization Techniques

3.5.1 Thickness Measurement

The thickness of the thin films was measured with a contact profilometer. Basically, it measures the height of the substrate and the substrate with film on it, so the differences between the twos is the thickness of the sample. Films need to be scratched carefully to differentiate between the substrate and the thin film. Measurement was done by a diamond stylus moving across the samples' scratches at specific distance. The deflection of the stylus generate the surface profile of thin film, hence the thin film thickness could be obtained. A schematic diagram of the thickness measurement is illustrated in the Figure 3.4.

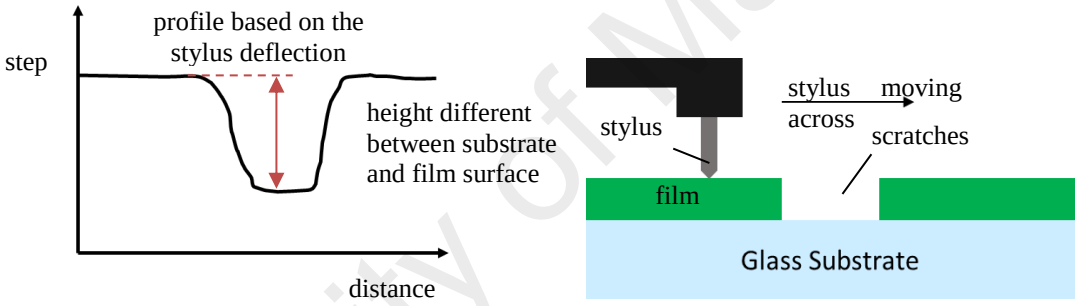

Figure 3.4: Schematic diagram showing the thickness measurement.

In this work, thickness of undoped and nickel-doped zinc oxide thin films were measured by using KLA TENCO P-6 surface profilometer (Figure 3.5). The films were scratched along the sample evenly thus measurement could be done at several heights across the scratches. Finally, average thickness was calculated from them.

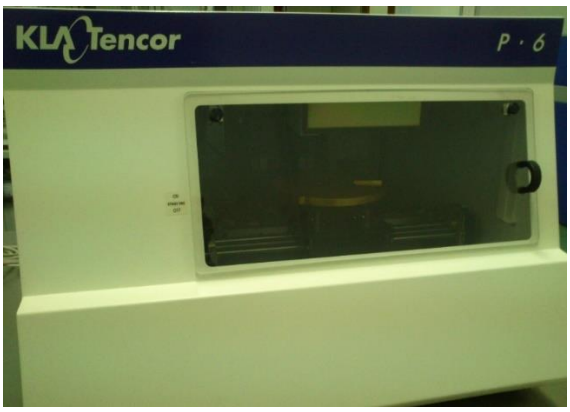

Figure 3.5: KLA Tencor P-6 surface profilometer.

3.5.2 X-ray Diffraction (XRD)

Crystalline structure of deposited Ni-doped zinc oxide (NZO) films were determined by using X-ray Diffractometer or XRD. X-ray diffraction is a non-destructive technique to determine and identify crystalline samples revealing the crystal structure of the material. A crystal lattice is a three-dimensional systematic arrangement of atoms in space as example cubic, rhombohedral, hexagonal, etc. The lattice forms series of parallel planes and separated by a distance *d* from each other, and moreover this *d* varies according to material (Do et al., 1997; Kolosov et al., 2001). Diffractogram or diffraction of samples is the measurement of constructive interference that occurred after monochromatic source X-ray beams upon the crystal planes of crystalline samples. Collimated X-rays were projected towards the samples, then the reflected rays results in constructive interference as they meet Bragg's Law condition,

$$n\lambda = 2d\ sin\,\theta \tag{3.1}$$

where *n* is an integer denoting the order of diffraction, λ is the incident X-ray wavelength, *d* is the distance of plane in the lattice and θ is the angle between incident ray and scattering plane or the diffraction angle as shown in Figure 3.6. In a nutshell, diffractions only occur when distance taken by the reflected rays from successive crystallographic plane by *n* number of wavelength (Callister, 2007). Thus, to meet Bragg's Law conditions as the angle θ was varied, *d*-spacing value differs. Characteristic pattern of samples can be obtained by plotting angular positions and diffraction intensities.

Table 3.2: Scanning parameters of XRD measurement.

Step size	0.0260
Step time	198.6450
Applied voltage	45 kV
Scan range	20° - 80°

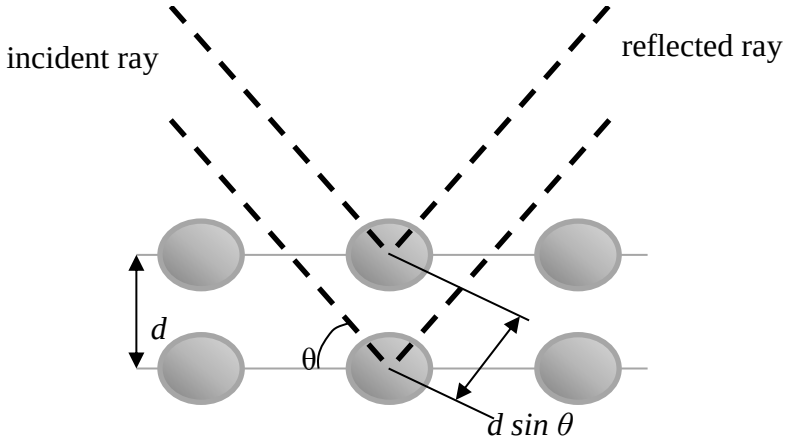

Figure 3.6: Diffraction pattern of X-rays by atomic plane.

The crystallography of deposited nickel-doped zinc oxide thin films in this research were determined with XRD measurement performed by PANalytical Empyrean diffractometer as in Figure 3.7. with the scanning parameters are shown in Table 3.2,.

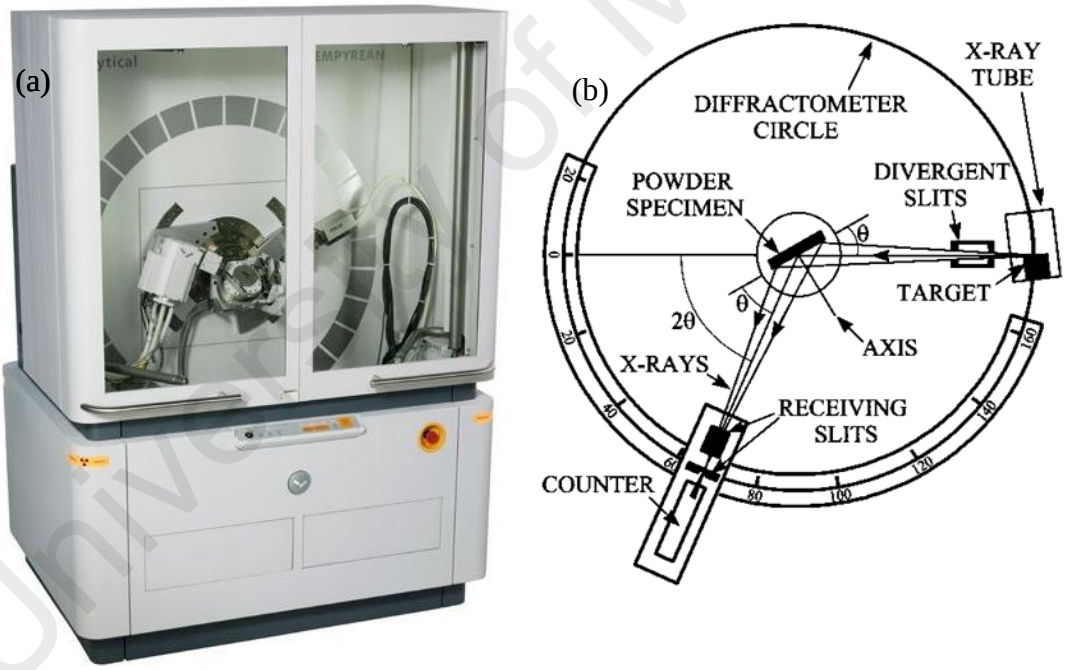

Figure 3.7: (a) An X-ray diffractometer model PANalytical Empyrean and (b) a schematic diagram of an xray diffractometer.

3.5.3 High-resolution transmission electron microscopy (HR-TEM)

High resolution transmission electron microscopy (HR-TEM) provides a high resolution images of sample structure in the atomic scale where it can visualize feature to minimum size of 1Å ($1x10^{10}$ m). Thus with this tool, we can study the crystal arrangement

of the material and rectifying the initial XRD analysis. In basic of TEM working principle (Figure 3.8(a)), electron beam was shone on piece of crystal sample which had been tilted at low Miller indices direction. This, in intention for the sample to be exactly perpendicular to electron beams. Lattice planes will be sufficiently close to Bragg position when they are about parallel to the electron beam, and results in diffractions of the primary beam. This diffraction is the Fourier transform of the periodic potential of electron in two dimensions. It was then brought back together with primary beam by objectives lens. Their interference provides a back-transformation and leads to an enlarged picture of the periodic potential.

HR-TEM images in this research were acquired by using JEOL JEM 2100-F (Figure 3.8(b)). As a preparation of HRTEM measurement, the deposited ZnO thin films on the glass substrate were sonicated in ethanol until the ZnO film peeled off and dispersed in the solvent. The mixture was then dropped on top of an amorphous carbon coated copper grid and dried thoroughly before the measurement can be done.

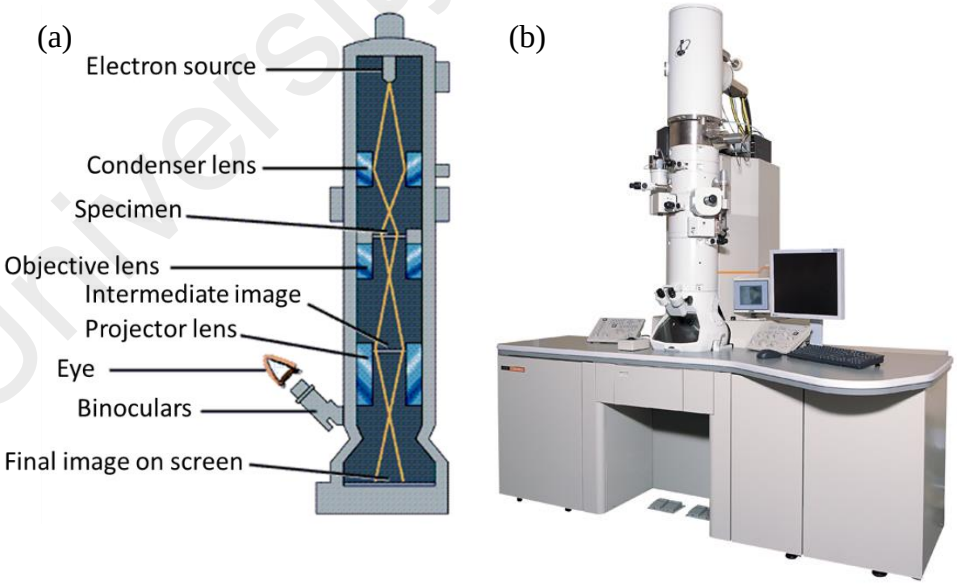

Figure 3.8: (a) A Schematic diagram of general transmission electron microscope, and (b) A model of JEOL JEM 2100F High Resolution Transmission Electron Microscope.

3.5.4 Field Emission Scanning Electron Microscopy (FESEM)

In order to study the surface morphology of the thin films, field emission scanning electron microscope (FESEM) images were obtained using Hitachi U8000. Generally, a scanning electron microscope (SEM) electron microscope that is capable of producing image of a sample by using energetic electron beam to scan across the sample on a fine scale. The interaction between the electrons and the atoms that make up the sample results in signal generation that contain information about the physical properties of the sample such as the sample's surface topography, composition, distribution pattern, shape and size dimension of the grains as well as its crystallographic feature.

Energy dispersion X-ray spectroscopy or EDX measurement has been performed with a JEOL JSM 7600 field emission scanning electron microscope (FESEM). It is used to analyze element of the thin film sample where in this work, initial ratio and stoichiometry calculation of the synthesized element could be validated.

3.5.5 Optical Characterizations

3.5.5.1 Ultraviolet-Visible-Near Infrared (UV/VIS/NIR) Spectrometer

UV/VIS/NIR spectrometer is used to determine the optical transmittance, absorbance and reflectance of the thin film sample. The model used is Perkin Elmer Lambda 750 UV/VIS/NIR Spectrometer as shown in Figure 3.9. In the spectrometer there are four main parts; light source, sample compartments, detector and data acquisition computer. Sample compartments are in between the light source and the detector. Every set of measurements were done after initially calibrated with their substrate. In this research, transmittance of clean glass substrate were measured first for spectrometer's calibration. Only after that, the samples i.e. ZnO thin films were placed in the sample compartment to measure their transmittance and absorbance.

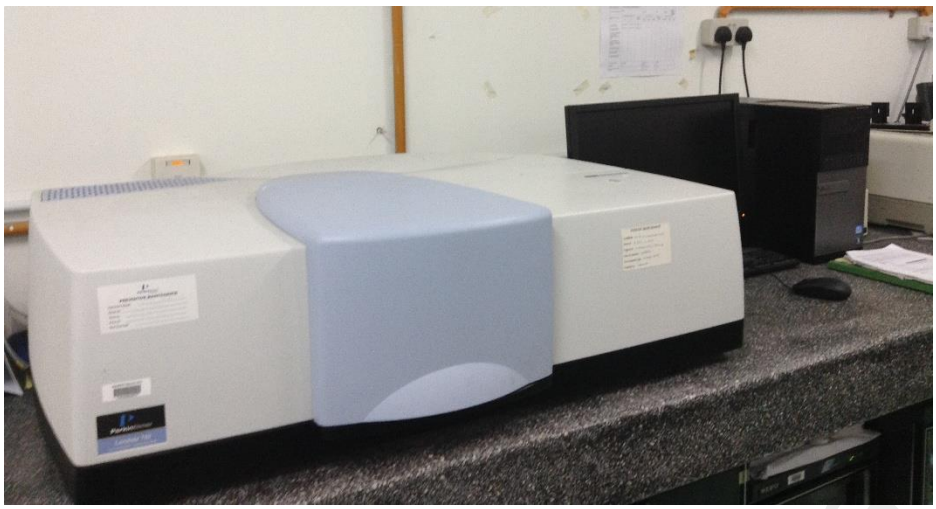

Figure 3.9: Perkin Elmer Lamda 750 UV/VIS/NIR Spectrometer with data acquisition computer.

A simple illustration on UV/Vis/NIR transmittance and absorption measurement is shown in Figure 3.10. The initial light intensity (I_o) and transmitted light intensity (I) are measured, where then the transmittance can be determined by $T = I/I_o$ and the absorption, $A = -\log (I/I_o)$ according to Beer-Lambert law. Also with $I = I_o e^{-\alpha t}$ relation, the absorption coefficient, α can be calculated. In this work, transmittance, absorptions and reflectance of all the samples have been measured by using the UV/VIS/NIR spectrometer with the parameter used stated in Table 3.1. There is plenty of information can be derived from the measured transmittance for instant the film thickness, t, index refraction, n, energy band gap, E_g and extinction coefficient, k.

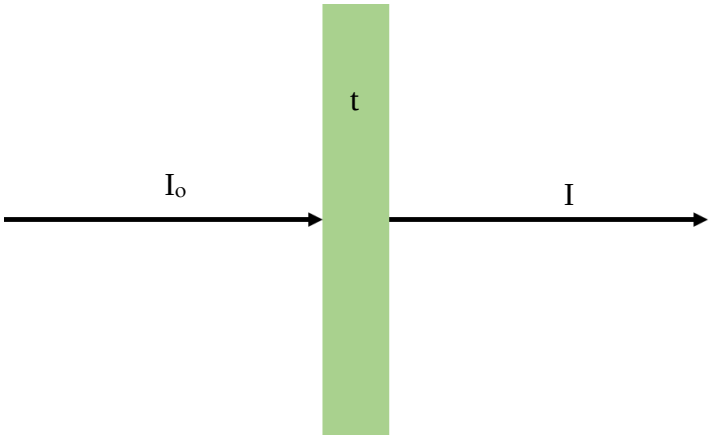

Figure 3.10: UV/Vis/NIR Spectroscopy working principle.

Table 3.3: Parameter of UV/VIS/NIR spectrum.

Photometric mode	A, %T, %R
Response	Fast
Band width	5.0 nm
Scanning speed	2000 nm/min
Start wavelength	900 nm, 1500 nm
End wavelength	200 nm, 300 nm
Data pitch	2.0 nm

3.5.5.2 Photoluminescence

Another optical characterization done in this work is the photoluminescence measurement which have been performed with Perkin Elmer Luminescence Spectrometer LS50B model (Figure 3.11). Photoluminescence (PL) spectrometer provides information on electronic structure of a material by measuring its transition energy. Basically, PL is a process when any material emitting light after absorb photon. When an absorbed photon energy is sufficient for the material, electrons will excite from low to a higher energy state (Gfroerer, 2000). The electrons will then turn to the lower energy level by releasing energy in a form of light emission. This emitted light is called photoluminescence (PL).

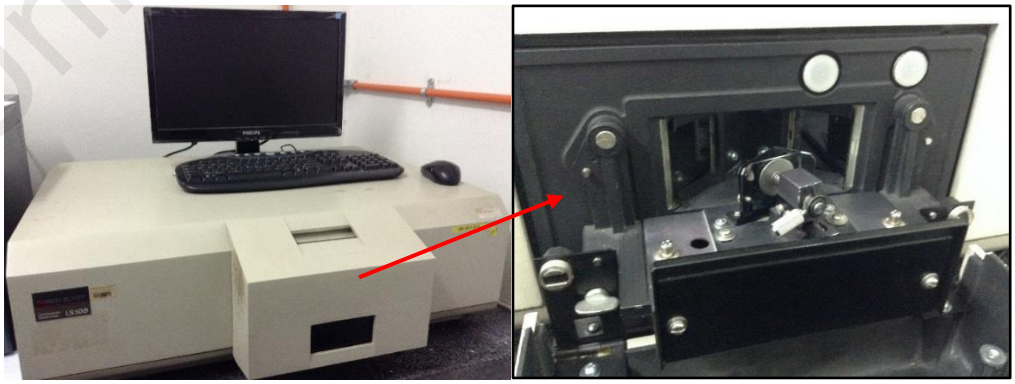

Figure 3.11: Photoluminescence spectrometer (Model: Perkin Elmer Luminescence spectrometer LS50B) and photograph in right shows inside the sample compartment.

The emission spectra of pure and doped zinc oxide thin films were measure in the range of 200 to 730 nm, with data pitch at 0.5 nm, slit of 15 mm and excitation wavelength of 280 nm. The emission spectra obtained provides information to identify surface, interface, impurity level and etc.

3.5.6 Electrical Characterizations

Sheet resistance, R_s of the thin films was measured with a four-point probe (Jandel Universal Probes) as photographed in Figure 3.12(a). Four-point probes is consisting of four probes as illustrated in Figure 3.12(b), touching the sample surface. Current is swept through probes 1 and 4 from 0.00 A to 1.00 nA, while the voltage potential was measured between probes 2 and 3. When there is a resistance in the sample, there will be a drop in voltage. Source and output were measured by Keithley 2400 source measure unit (SMU). Resistivity, ρ of samples was then calculated by

$$\rho = \frac{\pi}{ln\,2} R_s t \tag{3.2}$$

where t is the films thickness, and R_s is the measured sheet resistance. However, for a higher resistivity sample (~10^4 Ω), two point probe I-V measurement is more suitable.

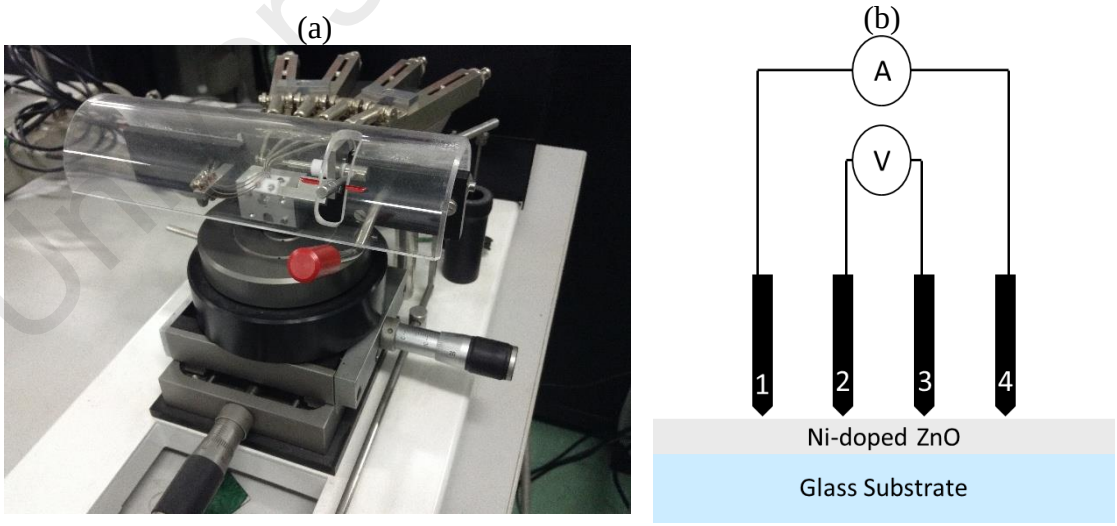

Figure 3.12: (a) A photograph of Jandel Universal probe (b) illustration of schematic structure of a four-point probe.

Sheet resistance, R_s alternatively been measured by two probes method using aluminum electrodes, in coplanar geometry parallel to the substrate surface as in Figure

3.13 with electrodes distance is 40 μm to each other. This electrical characterization relies on Keithley 2400 source measurement unit (SMU). Resistivity, ρ of thin film with film thickness t from this structure can be calculated by,

$$\rho = R_s t \tag{3.3}$$

Current-voltage (IV) measurements of the thin films have also been carried out at different temperature 300 to 473 K in order to determine the activation energy E_a where beforehand, it is necessary to know the Ohmic region of the samples at different temperature.

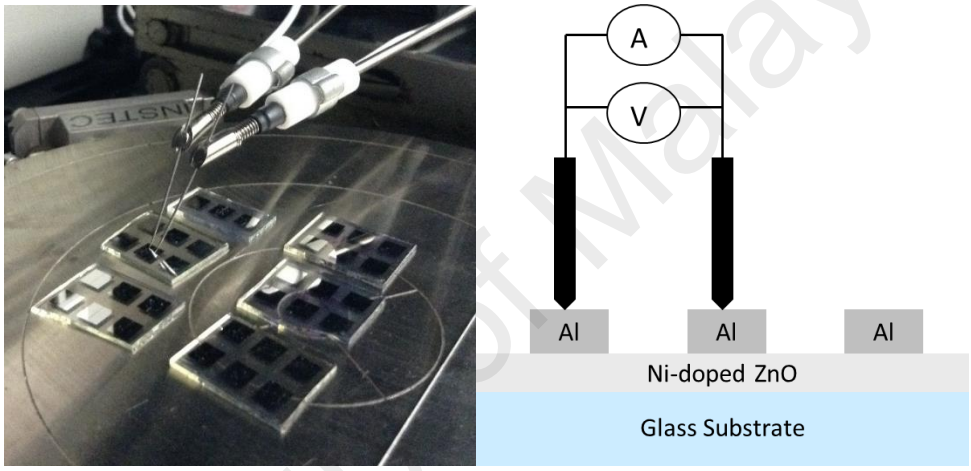

Figure 3.13: (a) Basic two probes IV measurement setting and (b) illustration schematic structure of I-V measurement.

The activation energy E_a evaluated by d.c. conductivity from IV measurement is taken at different temperature. The dependency of electrical conductivity σ to the semiconducting temperature was described by Arrhenius equation,

$$\sigma = \sigma_o \, exp(-\frac{E_a}{kT}) \tag{3.4}$$

with σ_o is the pre-exponential factor, k is the Boltzmann constant and T is temperature. The activation energy E_a and pre-exponential σ_o factor were obtained from the least square straight line fits of the data.

3.5.7 Photoelectron Spectroscopy (PES)

Generally, photoelectron spectroscopy or PES is a measurement of emitted electron from matter by photoelectric effect. PES detects the kinetic energy of the electrons escape from the sample surface after photon of light hit the surface electrons and transfer their energy. The mechanism can be explain by the relation;

$$photon\ energy, hv = E_B + E_K \tag{3.5}$$

where E_B is the binding energy, and E_K is the kinetic energy of the sample measured. The photon energy, *hv* used to hit the surface transferred to the surface and energized electrons to overcome their attraction and then escape from the surface.

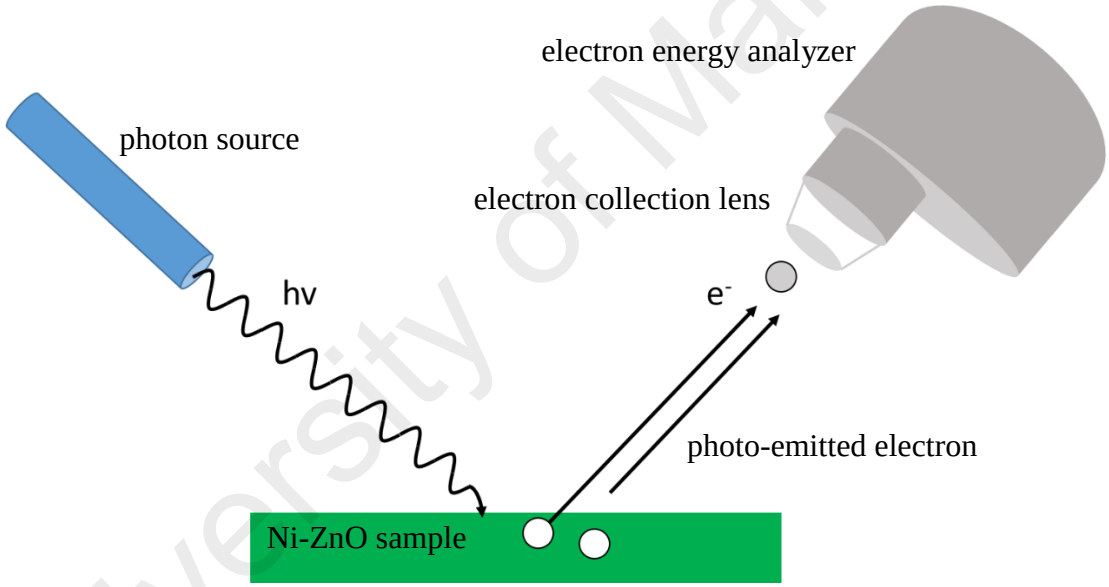

Figure 3.14: Schematic diagram of photoemission process and measurement.

In Figure 3.14, the principle of photoelectron measurement were explained. There are three main steps in a photoemission process; first process is when the electron in the material absorb the incoming photon, it is transferred from initial to the excited state. Then, the electrons travel to the sample surface and finally ejected into the vacuum. These ejected electrons are captured by the electron energy analyzer to measure their kinetic energy.

Photoemission spectra of the thin films were measured at beamline 3.2(a) (PES) Synchrotron Light Research Institute, Nakhon Ratchasima, Thailand which the facility is

photographed in Figure 3.15. Initially, samples were cut to the size that could be mounted on a stainless steel plate of 28 mm x 94 mm as shown in Figure 3.15(a), before being transferred to the measuring chamber.

(a) (b)

Figure 3.15: Picture of (a) sample stage with size 28 mm x 94 mm and (b) PES in beamline 3.2a, SLRI.

Two types of PES measurement have been done. They are X-ray photoelectron spectroscopy (XPS) and Ultraviolet photoelectron spectroscopy (UPS). Briefly, by definition XPS is a photoelectron measurement using soft x-ray (200-2000 eV), this range radiation is to examine the core-levels of the samples. Due to the grating limitation in the synchrotron facility, measurement done in the range energy of 30-650 eV with photon energy *hv* of 650 eV. XPS data gives information on the energy level of atomic core electrons, and chemical shifting of core levels tells the chemical structure of the sample.

In UPS measurement, the light source is in the ultraviolet (UV) range where in the SLRI, measurement was done at 0 to 45 eV with 0.1 eV step size resolution. The photon energy for UPS measurement was set at 39.5 eV. The valence energy level were studied by UPS, thus electronic structure of the thin films could be explained.

Prior to each measurement, a calibration with gold is necessary since the photon energy of the synchrotron light is unstable. Narrow scan of Au 4f in the kinetic energy range from 495 to 525 eV was made before every set of XPS measurement was performed to confirm the charging shift of the measured energy (if any). While for UPS calibration, with the same range of measurement parameter, the work function of gold (Au), can be

calculated from the photo emission spectrum by taking into account the kinetic energy, E_K distribution,

$$E_K = hv - E_B - \Phi_S \tag{3.6}$$

with hv is the photon energy of the source, binding energy is E_B and work function of the metal sample is Φ_S.

3.6 Summary

Ni-doped ZnO thin films were prepared by sol-gel spin coating technique, with pre-heat treatment at 300 °C, and post-heat treatment at 500 °C. The characterizations for the thin films were made to study the structural, morphology, optical and electrical properties of the transparent ZnO thin films with respect to nickel doping. The structural characteristics were investigated by x-ray diffractometer, while the morphology of the thin films were studied from FESEM images. Optical analysis give information on their transparency, the energy band gap, and also defects of the thin films. Electrical characterizations provide the conductivity and resistivity of the thin films. Information on optical and electrical properties are very essential for optoelectronic applications.

CHAPTER 4: STRUCTURAL AND MORPHOLOGICAL PROPERTIES

4.1 Overview

This chapter presents the experimental result on structural and morphological of deposited zinc oxide thin film with respect to nickel doping by sol gel spin coating technique from precursor solution of zinc acetate dihydrate, ethanol and diethanolamine (DEA) as additive. It is essential to identify the effect of doping in developing a thorough understanding on the structural development of the thin film. Micro and nano-structural development of the films involves certain mechanisms. It can be discussed by relating to their nucleation and growth of cluster on the film. Thus, outputs from XRD, HR-TEM and FESEM are analyzed and discussed in this chapter. Other than that, EDX analysis is also utilized to confirm the stoichiometry of samples yielded.

4.2 Film formation and Crystal Growth

Transparent zinc oxide thin films were successfully deposited on top of glass substrates by spin-coating technique. The thickness of the films were determined from surface profiler measurements. Since the spin coating parameters and concentration of the precursor solution are fixed (0.5 M), sample thickness was predicted to be consistent. In Figure 4.1, thickness of the deposited ZnO thin film is presented with respect to Ni-doping concentration. The average thickness measured is around 300 to 400 nm, where for pure ZnO thin film, the value is 308 nm, and for Ni-doped ZnO thin films, the values are 361, 395, 436, 412 and 391 nm respectively for 1 %, 2 %, 3 %, 4 %, and 5 % Ni-doping. Overall, the percentage error is adequately small except for that of pure ZnO and 1 % Ni-doped ZnO. These two samples are less uniform compared to the others as the thickness measurement was taken at multiple points in a larger surface area throughout the samples. With respect to the doping concentration, thickness of the deposited thin

films is independent of the Ni. Instead, the thickness of sol-gel deposited thin films depends on their deposition parameters such as precursor concentration or viscosity and rotation speed of spin coating.

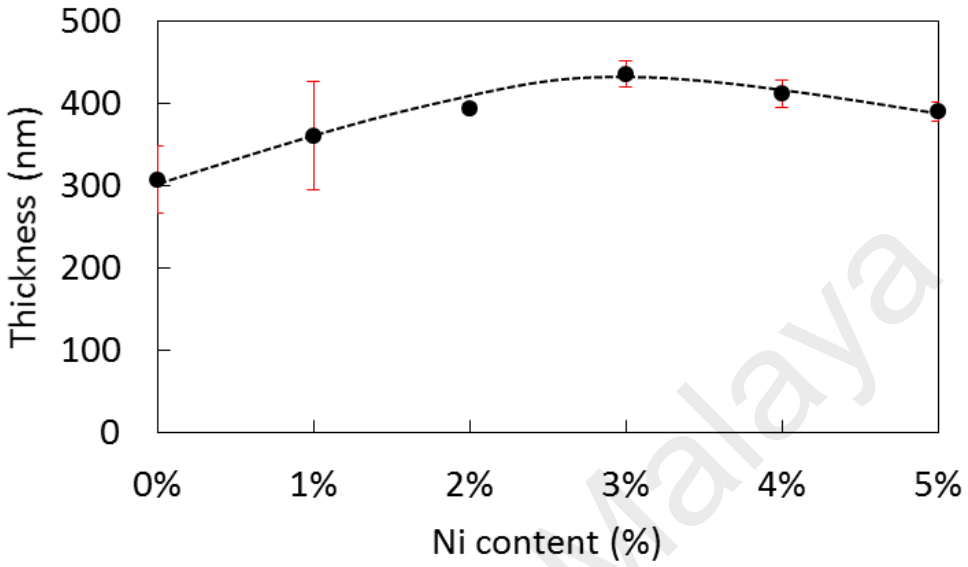

Figure 4.1: Thickness of deposited ZnO thin film by sol gel method with different Ni doping concentration.

Generally in a sol-gel process, molecular precursor in a homogeneous solution undergoes a series of transformation: 1) hydrolysis of the molecular precursor; 2) polymerization via successive bimolecular addition of ions, forming oxo-, hydroxyl or aqua bridge; 3)condensation by hydration; 4)nucleation; and 5)growth (Hu et al., 2000; Pierre, 2013).

In the growth of ZnO crystal, Spanhel and Anderson had suggested two possible ways to explain the mechanism; Ostwald ripening and aggregation. In the colloidal precursor sols, as soon as the smallest stable molecular cluster are formed, they rapidly combine to give the next most stable aggregate. The primary aggregates would further rapidly combine to give the next most stable secondary aggregate and so on. In further work, the authors observed that the primary clusters were stable aggregates and the growth of ZnO crystal in sol-gel process would be a result of rapid aggregation rather than a result of Ostwald growth. As a conclusion to that, the Ostwald mechanism should be considered

as only one possible approach to the formation of bulk materials. (Spanhel & Anderson, 1991).

In another work, Spanhel 2006 reported that in a system of zinc acetate dihydrate (ZAD) as precursor, at least four different primary particles or clusters serving as initiators of the ZnO colloid growth could be identified. These primary particles or clusters naturally depend strongly on the synthesis conditions chosen such as its initial salt concentration, time and temperature of thermal treatment, the nature of alcohol solvent, and the overall humidity, storage and analysis conditions.

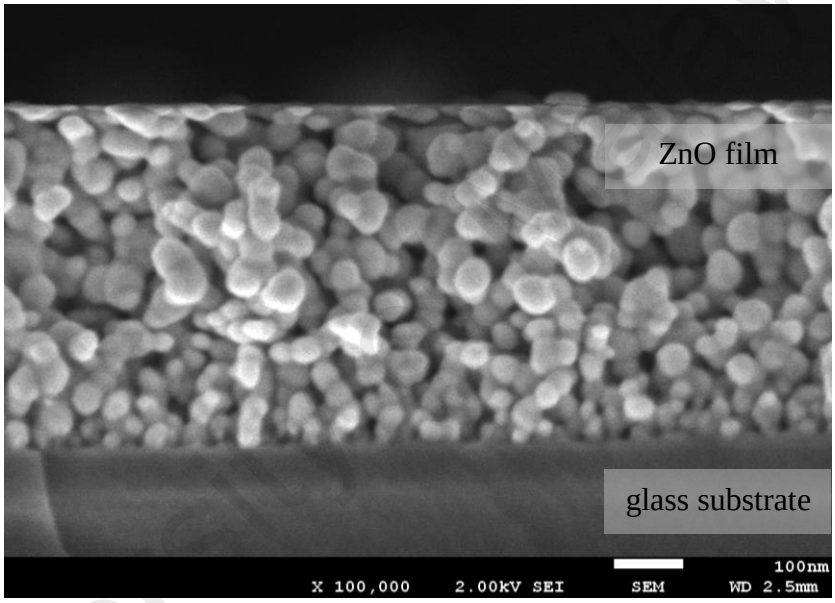

Figure 4.2: FESEM image of cross-sectioned deposited ZnO thin film.

In Figure 4.2, a cross-sectional FESEM image of sol-gel deposited pure ZnO thin film is shown, with 100,000 times magnification. ZnO particles growth can be observed in the thin film - particle size near the glass substrate increase as it grow to its surface. This may be the results of pre-heating treatment process done to the sample where the spin coating process were repeated several times after the pre-heat treatment. This may lead to an aggregation of particle at each layer deposited, and stable particles grow bigger after the pre-heating process.

4.3 X-Ray Diffractions (XRD)

X-ray diffraction patterns of pure and Ni-doped ZnO thin films deposited with different mol percentage of nickel (0 %, 1 %, 2 %, 3 %, 4 %, and 5 %) are shown in Figure 4.3. All samples are polycrystalline and give strong diffraction peaks at 2θ = 31.70°, 34.38 and 36.18° which corresponds to (100), (002) and (101) hkl plane respectively. These peaks indicate zinc oxide hexagonal wurtzite structure by matching with PDF-2 pattern code 01-075-0576 reference. Besides the three peaks, several other peaks are clearly seen at 47.6°, 56.7°, 63.0°, 68.1° and 69.2° diffraction angle respectively indicating (102), (110), (103), (112) and (201) hkl plane. Diffraction peaks intensity increase with Ni-doping until 3 % and decrease with more addition. This shows an improvement to the ZnO crystallinity up to 3 % of Ni and decreasing with more of it. Except for a different preferential diffraction peak, this shows quite a similar trend to Abed et al., 2011 work where the preferred plane (002) gave the highest intensity at 3 % Ni-doping. However, this behavior is in opposition to doping effect of classical Al and In on ZnO structure where these atoms destroy the initial preferential orientation of undoped film, becoming polycrystalline. In this case, textured structure disappears by increasing the doping concentration (Yoshida et al., 2000). Moreover, there is no peak signifying metallic Zn detected nor Ni and its oxide (NiO) in the 2θ region displayed. This may suggest Ni^{+} substitutes Zn^{+} in the hexagonal crystal lattice without altering the lattice structure.

In the study of sol-gel thin film, Fujihara reported orientation is basically a matter of nucleation and crystal growth. This can be explained by first looking to the influence of substrate. There are two possible mechanisms for film orientation of film on glass substrate which are the initial orientation due to nucleation and the final growth orientation. Both are results from the nucleation at film/substrate interface. If it is compared to vapor phase deposition, nucleation occurs in an initial stage of deposition

after adsorption of raw materials. While in sol-gel process, nucleation is characterized by post-deposition crystallization. Activation energy of film/substrate interfacial must be lowered in order for nucleation to preferentially grow at the substrate surface (Fujihara et al., 2001).

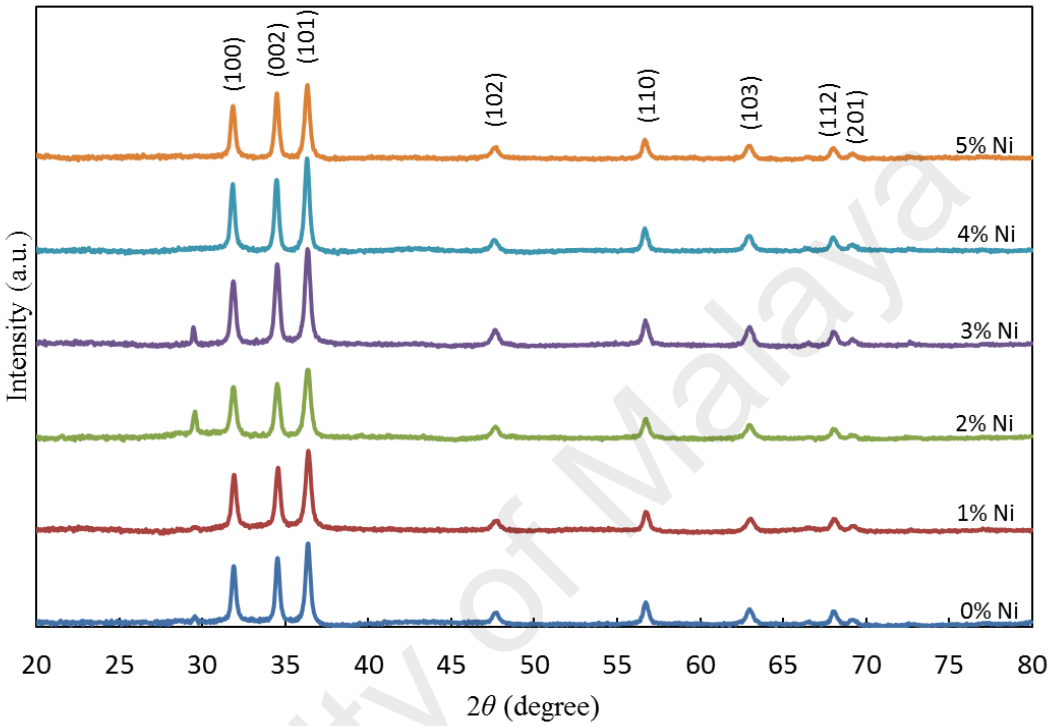

Figure 4.3: XRD patterns of undoped and Ni-doped ZnO thin film.

In order to further evaluate the preferred orientation, texture coefficient, *TC (hkl)* was calculated by its common formula as shown in Equation 4.1.

$$TC(hkl) = \frac{I(hkl)/I_o(hkl)}{\frac{1}{N}\sum I(hkl)/I_o(hkl)} \quad (4.1)$$

where *TC(hkl)* is the texture coefficient of the hkl planes, I is the measured or normalized intensity, I_o is the corresponding standard intensity from JCPDS, while N is the number of reflection. Accordingly, hkl plane with a higher value of *TC* is a more preferred orientation. *TC* values calculated for the three prominent peaks (100), (002) and (101) are shown in Figure 4.4 with respect to the nickel doping percentage. It can be clearly seen that for all samples of undoped and Ni-doped ZnO thin films, (101) plane gives the highest *TC* value compared to (100) and (002) planes. Thus, the preferred orientation of

all samples is at (101) plane. This preferred orientation is consistent with Wang et al., 2006 and Liu et al., 2008 works which were also using the same sol gel method to deposit ZnO thin films.

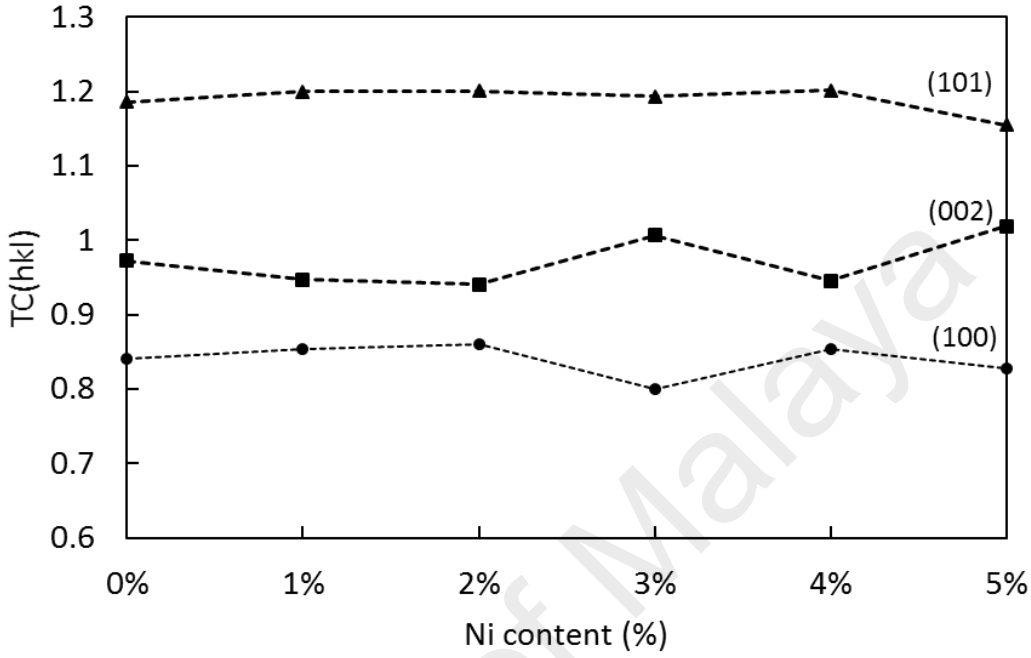

Figure 4.4: Texture coefficient, *TC(hkl)* of plane (100), (002) and (101).

Yet at the same time, a contradiction is also found when compared with others work. Majority of the sol-gel deposited ZnO thin films give the preferred orientation plane at (002) c-axis oriented. The orientation of sol-gel deposited ZnO thin films is usually due to their precursors and heat treatment temperature. Considering the chemical system of the precursor solution (zinc precursors, solvent and additive), preferential orientation is also reflected to be due to the differences in the zinc coordination power and the boiling points of the additives (Nishio et al., 1996). Nishio reported a comparison effect of DEA, MEA, diethylenetriamine, and acetylacetone stabilizer on c-axis orientation with ethanol as solvent. Boiling point of these additives respectively are 271 °C, 171 °C, 207 °C and 140 °C. It was found the films prepared with MEA and acetylacetone are highly c-axis oriented in contrast to the films prepared with DEA or diethylenetriamine (Nishio et al., 1996). Ohyama et al., 1996 also reported a comparison of ZnO thin films obtained from precursor solutions containing two different additives: MEA and DEA. The thin films

prepared using MEA as an additive and annealed between 400 and 600 °C were highly oriented along c-axis, while the thin film prepared with that of DEA additive, ZnO films gives the three XRD peaks (100), (002) and (101) for the same range of heat treatment temperature. In agreement with this work, the possible explanation is probably due to the structure of alkanolamine-zinc acetate complexes form in the coating solutions. The ligand denticity of DEA is tridentate while MEA is a bidendate (Ohyama et al., 1996).

In term of size, crystallite is the smallest form of crystal. The crystallite size of pure ZnO and Ni-doped ZnO thin films can also be calculated from the diffraction pattern. The average crystallite sizes, *D* of the undoped and Ni-doped ZnO thin film were estimated from the X-ray diffraction pattern using the Scherrer equation,

$$D = \frac{0.9\lambda}{\beta \cos\theta_B} \tag{4.2}$$

where λ is the X-ray wavelength of 1.54 Å, θ_B is the Bragg diffraction angle of (101) peak, and β is the full width at half maximum (FWHM) of θ_B. Overall, the crystallite size *D* average is around 42 nm. The average crystallite sizes, *D* for different Ni-doping ZnO thin films are 46, 39, 38, 42, 48, and 46 nm for 0 to 5 % mol percentage of nickel respectively.

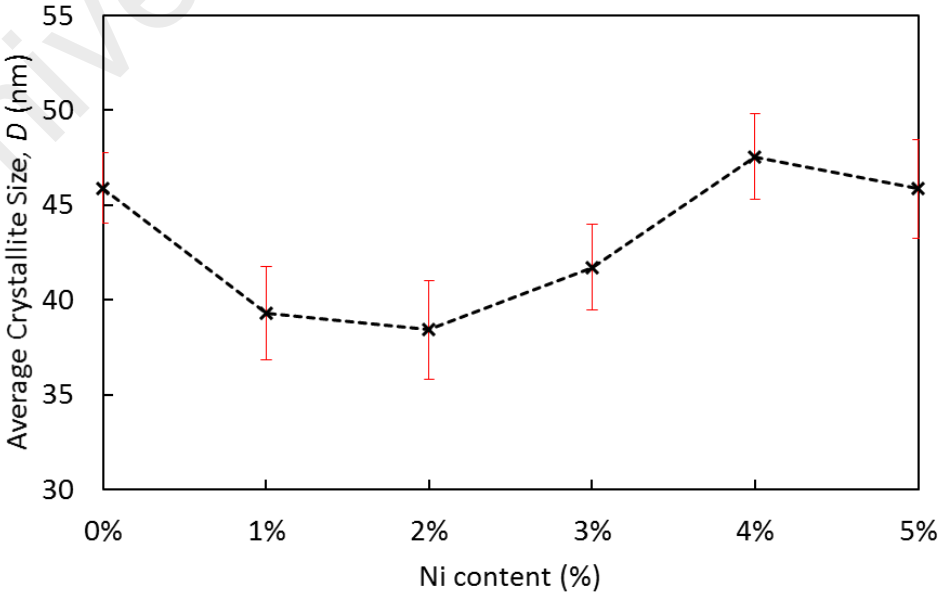

Figure 4.5: Average crystallite size of Ni-doped ZnO.

Figure 4.5 shows the graph of average crystallite size, *D*. By taking account the error propagation, the crystallite size of pure and doped ZnO thin film do not vary much except a slight decreases with 1 % Ni-doping until 3 %, and slightly increases back at 4 % and 5 %. Doping does not affected the crystallite size of ZnO thin film. The particle size of sol-gel ZnO thin films usually affected by aging time and aging temperature of alcoholic zinc precursor solution. According to Spanhel, aging of alcoholic ZnO colloid produces larger particles and bathochromic shift (Spanhel, 1991). Since these parameters were controlled at a fix aging time and temperature, size was expected to be not much different with different Ni-doping concentration.

Lattice strain or micro strain occur from the displacement of unit cells caused by dislocations, surface restructuring, lattice vacancies, interstitials, substitutionals and more. Micro-strains, ε developed in the thin films can be calculated from the diffraction spectra with the following equation,

$$\varepsilon = \frac{\beta \cos \theta_B}{4} \tag{4.3}$$

where θ_B is the Bragg diffraction angle, and β is the full width at half maximum (FWHM) of θ_B. Micro-strain, ε of all samples were plotted together with the crystallite size with respect to different Ni mol percentage is shown in Figure 4.6.

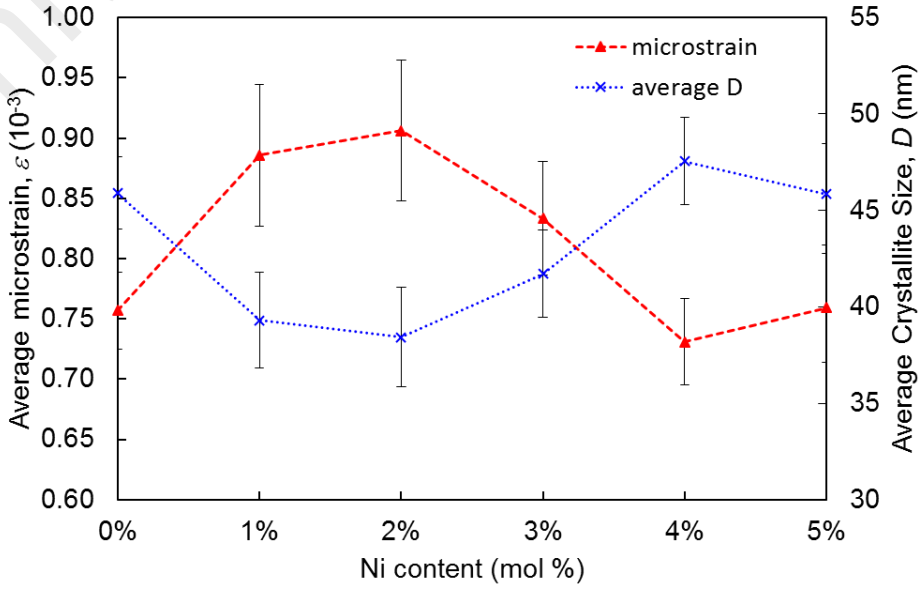

Figure 4.6: Microstrain, ε of Ni-doped ZnO thin films and average crystallite size, *D*.

Table 4.1: The 2θ value, average crystallite size (D), texture coefficient *TC(hkl)*, micro-strain (ε), and d-spacing of different Ni-doped ZnO from XRD spectra.

Ni content %	2θ value (±0.01)	Average Crystallite size, D (±0.1) nm	*TC(hkl)* (±0.001)	Micro-strain, ε (±0.001) x10^{-3}	d-spacing (±0.001) nm
0	31.90	45.9	0.841	0.754	0.281
	34.54		0.973	0.712	0.260
	36.37		1.186	0.804	0.247
1	31.92	39.3	0.854	0.830	0.281
	34.56		0.947	0.853	0.260
	36.39		1.199	0.974	0.247
2	31.87	38.4	0.860	0.929	0.281
	34.52		0.940	0.819	0.260
	36.35		1.200	0.971	0.247
3	31.87	41.7	0.800	0.797	0.281
	34.52		1.006	0.799	0.260
	36.35		1.193	0.904	0.247
4	31.83	47.6	0.854	0.728	0.281
	34.48		0.945	0.680	0.260
	36.31		1.201	0.785	0.248
5	31.85	45.8	0.827	0.750	0.281
	34.49		1.018	0.701	0.260
	36.32		1.155	0.827	0.247

From Equation 4.3, micro strain ε of ZnO thin film expected to be inversely related to the crystallite size D. Thus, we can see the micro strain ε increases with addition of nickel up to 2 % mol percentage, and decreases at higher mol percentage. The ZnO thin film structure become slightly stressed with nickel doping, and started to relax at mol percentage more than 2 %. This slight change with different Ni concentration can be ascribed by the substituted Ni^{2+} ion which have smaller ionic radius (0.069 nm) compared to Zn^{2+} ionic radius (0.074 nm). Atom that may trapped in the non-equilibrium position, shift to a more equilibrium position by releasing strain (Raja et al., 2014). As a summary of XRD analysis, the values of 2θ value (for three main plane) average crystal size D,

texture coefficient *TC*, micro strain ε and d-spacing of different Ni-doped ZnO thin films are shown in Table 4.1.

4.4 High Resolution Transmission Electron Microscopy (HR-TEM)

Previously in the XRD analysis, sample with 3 % Ni-doping was found to give the highest and narrow diffraction peak indicating that the 3 % Ni-doped ZnO thin film has the best crystal quality. Thus, this sample was chosen to be observed under a high resolution transmission electron microscopy (HR-TEM) to look at its lattice fringes in order to study the morphology and structure of Ni-doped ZnO thin film.

Figure 4.7 below shows a HR-TEM image of 3 % Ni-doped ZnO thin film. A single crystal can be observed clearly with a diameter of about 41.9 nm. This result is consistent if we compare with the calculated average crystallite size, *D* of 3 % Ni-doped ZnO thin film, which is 41.7 nm. The percentage different is around 0.5 %.

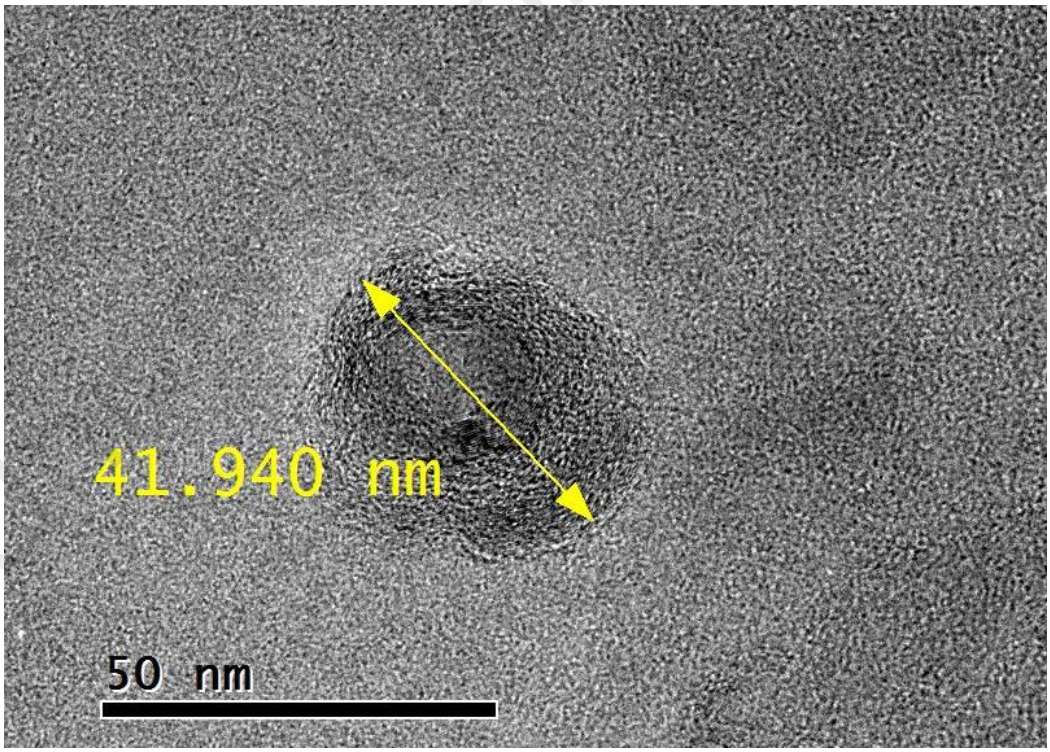

Figure 4.7: HR-TEM image of a single crystal 3 % Ni-doped ZnO thin film.

A higher resolution image of Figure 4.7 is shown in Figure 4.8(a). It shows a clear and coherent lattice fringes in a shape of either hollow hexagonal or hexagonal with

amorphous structure inside. The later describes it better when comparing to the FESEM images in Section 4.5, there is no images which could prove a hollow hexagonal structure of Ni-doped ZnO thin films. The lattice spacing measured from HR-TEM was about 0.26 nm, which refers to the (002) plane of hexagonal ZnO crystal. These confirmed that the structure of the nanocrystals exhibited (002) hkl; one of the preferred orientation found in XRD. Similar to that of Figure 4.8(b), the d-spacing value is about 0.26 nm.

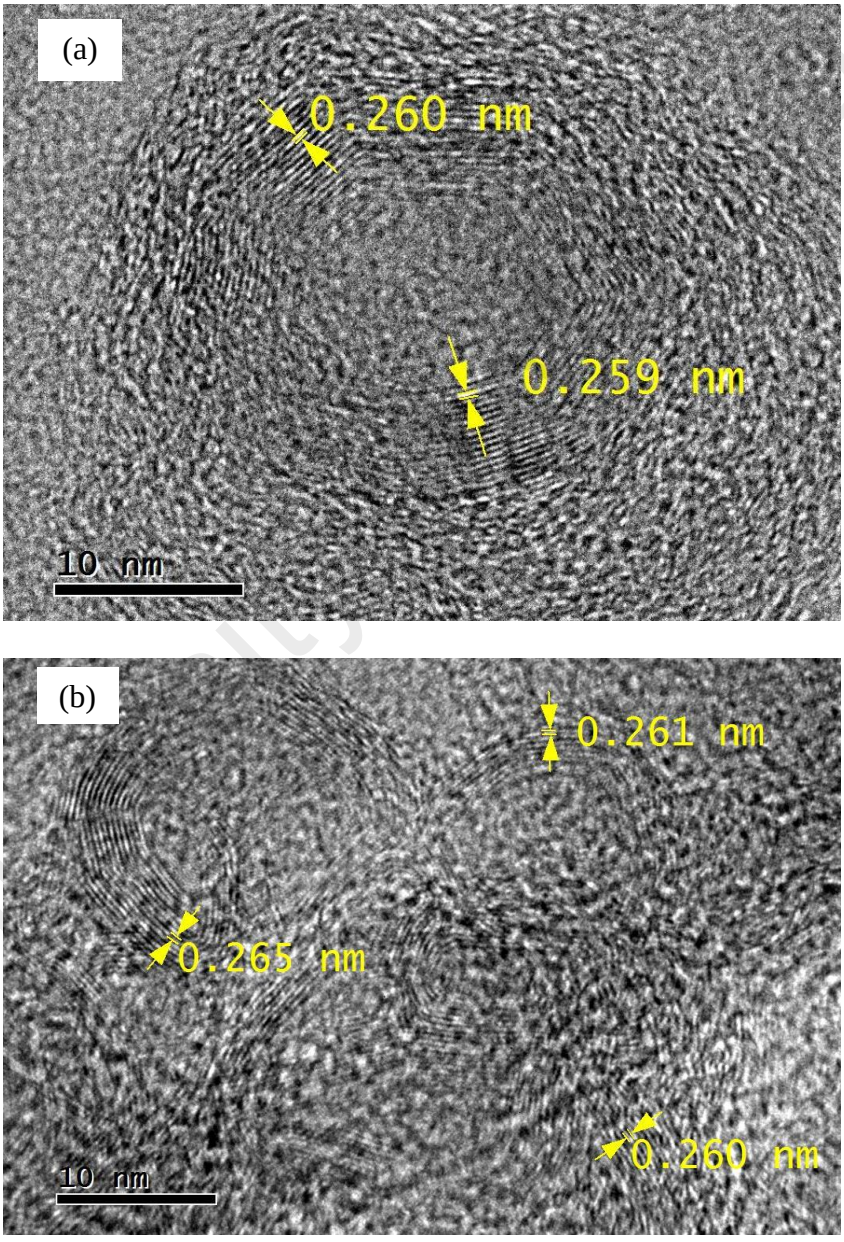

Figure 4.8: HR-TEM images of 3 % Ni-doped ZnO thin film.

4.5 Field Emission Scanning Electron Microscopy (FESEM)

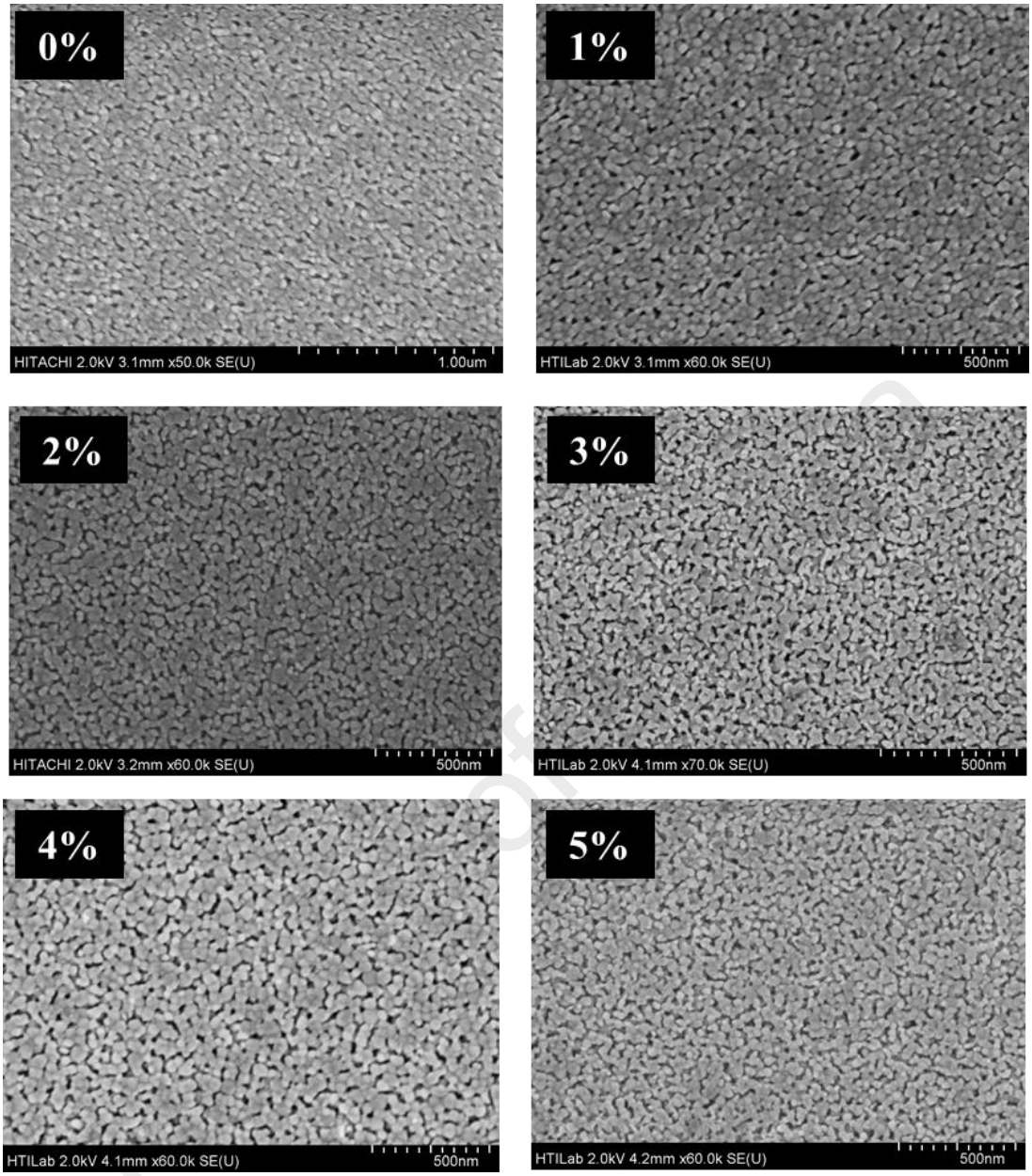

Figure 4.9: FESEM images series of ZnO thin films with different Ni-doping concentration.

Surface morphology of prepared ZnO thin films on glass substrates has been studied, and their FESEM images are presented in Figure 4.9. Figure 4.9 shows FESEM images of ZnO thin films with different Ni-doping concentration, varied from 0, 1, 2, 3, 4 and 5 mol percentage. Images were captured in 50k, 60k, and 70k x magnification. All of the images show a uniform, dense and adherent film.

In order to estimate the grain size or the particle size of the thin films, an open source image processing program, *ImageJ* was utilized to obtain grain/particle size distribution

for every image. The particle size distribution graphs are presented in the Figure 4.10. Mode of each graph is 50 or 70 nm; therefore size of the grains/particles of deposited pure and Ni-doped ZnO thin films is in the range of 50 to 70 nm. Summary graph of the grain size for each sample is presented in Figure 4.11. As the Ni-dopant mol percentage increases, the average grain size is the same at either 50 nm for 2-3 % Ni-doped ZnO thin films, or 70 nm for pure and 1, 4, 5 % Ni-doped ZnO thin films.

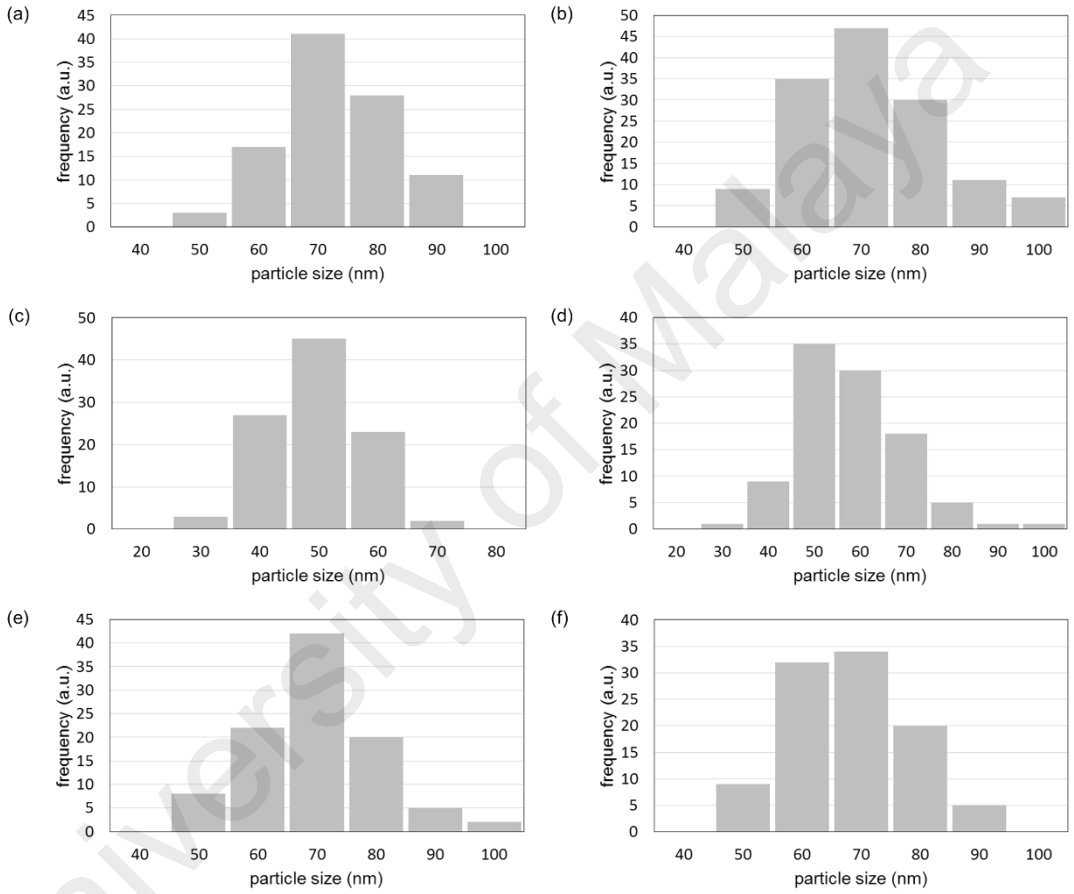

Figure 4.10: Particle size distribution graphs for (a) pure ZnO, (b) 1 % Ni, (c) 2 % Ni, (d) 3 % Ni, (e) 4 % Ni, and (f) 5 % Ni.

Essentially, the nature of sol gel ZnO thin film particles depend strongly on the synthesis condition chosen, especially the initial salt or precursor concentration, temperature and time of thermal treatment, nature of alcohol solvent and overall humidity, storage and analysis conditions (Spanhel, 2006). Also in other respects, Meulenkamp, 1998 described particle size was influenced by temperature, water and reaction products during the aging of ZnO sol. In this work, the ZnO sol parameters mentioned are fixed

and controlled, thus as discussed in the Section 4.3 Ni doping concentration is expected not to affect the grain/particle size or morphology of ZnO thin films generally.

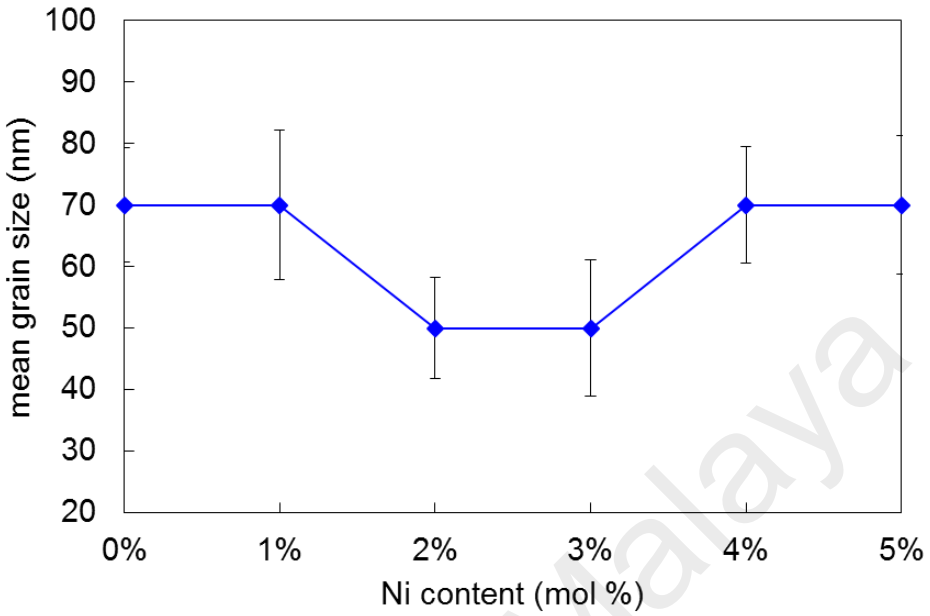

Figure 4.11: Summary from grain size distribution from FESEM images of ZnO thin films with different Ni mol percentage.

When comparing this grain size distribution to the crystallite size, *D* calculated from the XRD, the sizes are not in the same range or pattern. The values of crystallite size *D* calculated from XRD results are different compared to the FESEM estimation of grain size represented in Figure 4.11. They are actually not in contradiction as the size given by FESEM corresponds to dimension parallel to the substrate, while XRD corresponds to dimension perpendicular to the substrate (Bouaoud et al., 2013). Additionally, a crystallite is a unit of crystal from a long range order of atoms. While, a particle usually has more than one crystallite, but not necessarily. Thus, calculation from XRD gives smaller sizes as they are the crystallite size and not the grain size as obtained from FESEM.

4.6 Energy Dispersive X-ray Spectroscopy (EDX)

Energy dispersive x-ray spectroscopy (EDX) measurement has been performed to analyze the element of the thin film and also to validate the stoichiometry calculation of

the sample. The EDX spectra of pure and Ni-doped ZnO thin films are shown in Figure 4.12

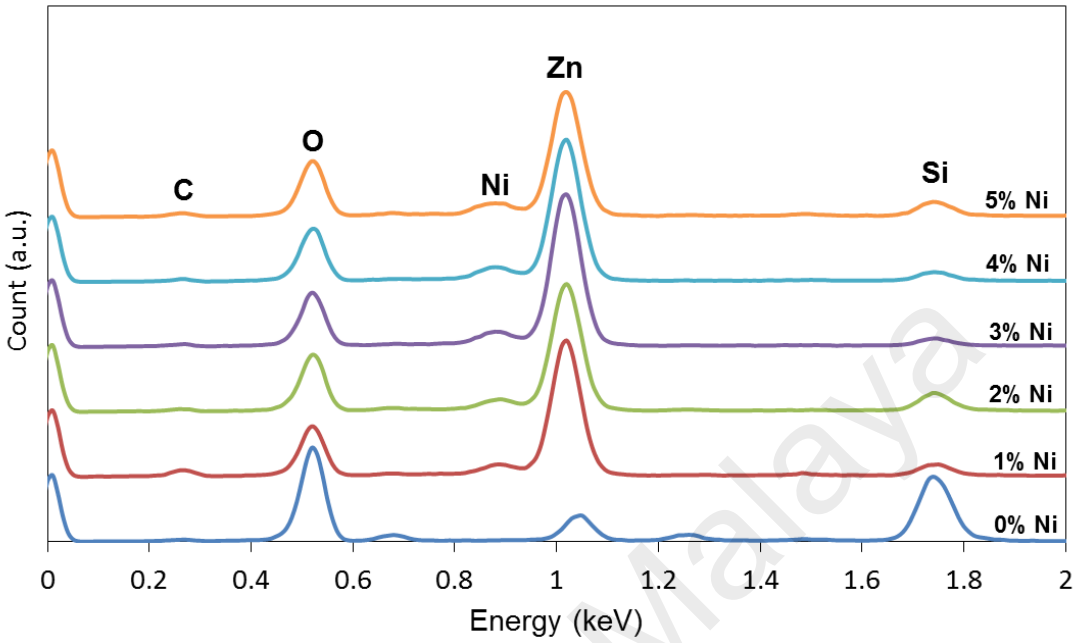

Figure 4.12: EDX spectra of pure and Ni-doped ZnO thin film with different nickel mol percentage.

The spectra confirm all of the thin films are mainly composed of Zn and O. There small amount of carbon element also detected may due to the carbon tape used during the measurement preparation of the sample, and also an appearance of Si peak in the ZnO thin film spectra is from the glass substrate. In the Ni-doped thin films, Ni element is clearly seen in spectra. This indicated that Ni was successfully incorporated in the ZnO thin films. The details of compositional elements in all sample are summarized in the Table 4.2.

Table 4.2: Compositional elements for ZnO thin films with different content of Ni-doping.

Sample	Atomic percentage of the elements (± 0.01 %)		
	O	**Ni**	**Zn**
pure ZnO	94.55	0.00	5.45
1 % Ni-doped ZnO	58.63	0.53	40.84
2 % Ni-doped ZnO	61.21	0.91	37.88
3 % Ni-doped ZnO	55.07	1.70	43.22
4 % Ni-doped ZnO	56.45	2.13	41.42
5 % Ni-doped ZnO	59.49	2.70	37.81

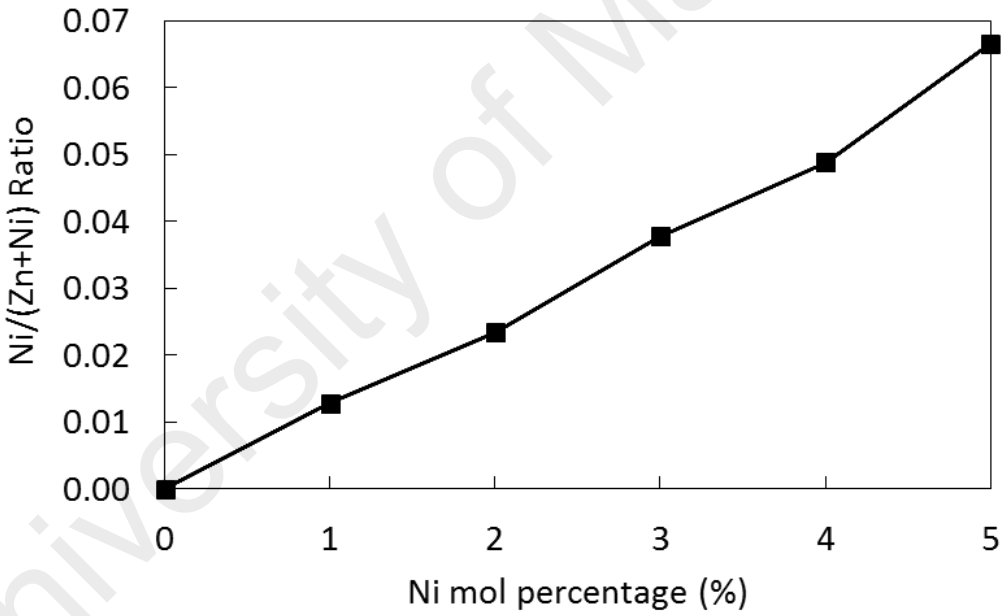

Figure 4.13: Ratio Ni to (Zn + Ni) content.

In the table above, the compositional elements of all sample is presented in term of atomic percentage. Ni content is observed in every doped sample with a consistent increase. An imbalance of Zn and O atomic percentage is clearly seen in pure ZnO thin film. This excessive atomic percentage of oxygen are speculated from the oxides of SiO_2 originated from the glass substrate. Subsequently, the ratio of nickel to total metal in the thin films were calculated from the table, and summarized as graph in Figure 4.13.

Stoichiometric balance is confirmed as the present of Ni in the ZnO system and mol percentage in precursor solution is nearly equal to nominal stoichiometry.

4.7 X-ray Photoelectron Spectroscopy (XPS)

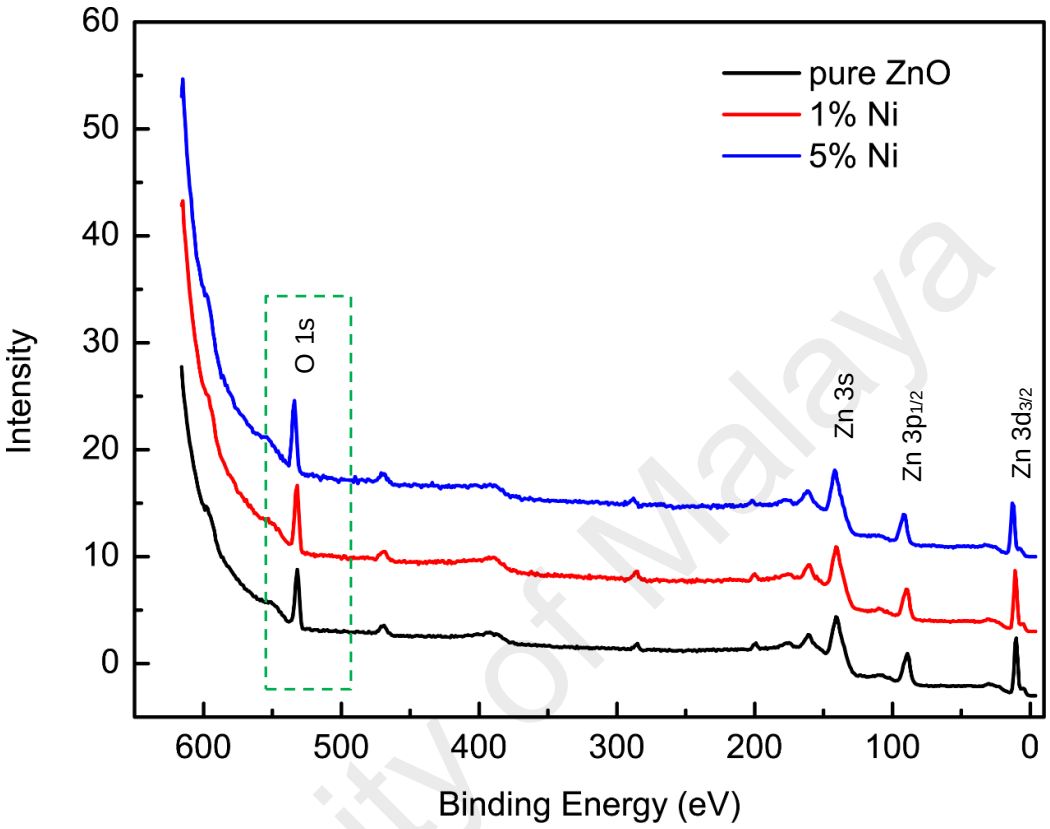

Figure 4.14: XPS survey for pure ZnO and Ni-doped ZnO thin films.

XPS spectroscopy is a technique used to investigate the chemical composition of materials. It is basically measure the kinetic energy of emitted electrons from the sample after soft x-ray light source hit the surface. Figure 4.14 shows the overlay XPS survey spectra of pure and Ni-doped ZnO thin films at different mol percentage (1 % and 5 % Ni-dopant). This XPS survey spectra were measured in the binding energy ranging from 0 to 600 eV. This measurement was done initially before the higher resolution scan to analyze the surface compositional. The detected elements from the survey spectra were zinc (Zn) and oxygen (O). Due to the limitation of the facility mentioned in previous chapter, core levels electron peak of Zn $2p_{3/2}$ and Ni $2p_{3/2}$ at 1021.8 eV and 852.7 eV respectively, could not be detected in the spectra.

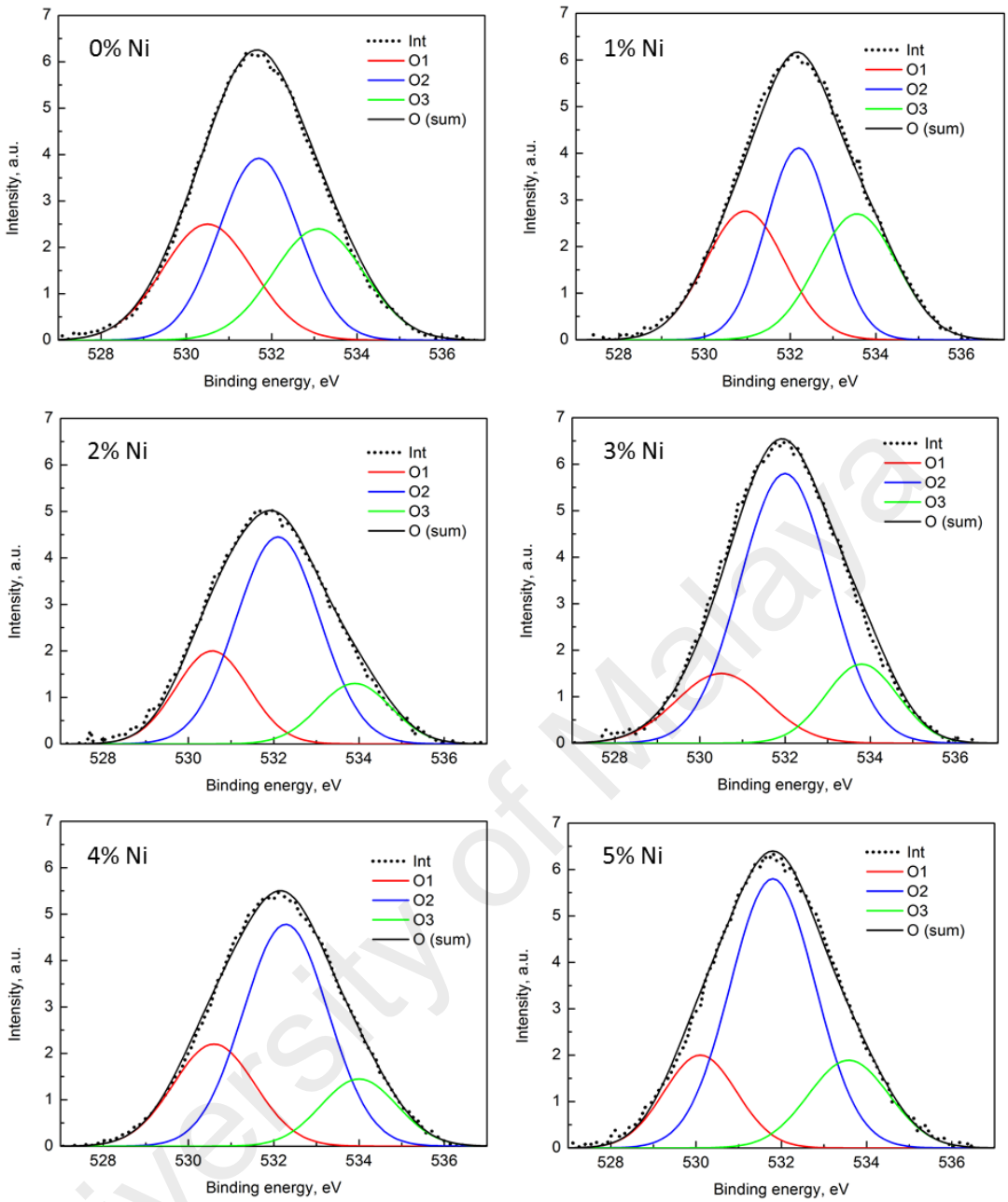

Figure 4.15: XPS spectra of O 1s and its Gaussian-resolved component for different Ni-dopant mol percentage (0 to 5%) where the dotted line (Int) is the measured XPS data, and the black line is the summation of the deconvoluted oxygen component.

In order to investigate the oxygen states in detail, O 1s spectra were carefully deconvoluted into three peaks (O1, O2, O3), using Gaussian fitting with the subtraction of Shirley type background, and are presented in Figure 4.15. The peaks are corresponding to low binding energy, middle binding energy, and high binding energy components centered at 530.5 ± 0.2 eV (O1), 532.0 ± 0.2 eV (O2) and 533.6 ± 0.2 eV (O3) respectively (Bang et al., 2012; Hsieh et al., 2008).

The low binding energy peak (O1) is attributed to O^{2-} ions on the hexagonal wurtzite structure of Zn^{2+} ion array, surrounded by Zn (or the Ni substitution). This peak indicates the Zn-O bonds, where intensity of this peak measures the amount of oxygen atoms that in a fully oxidized stoichiometric surrounding (Chen et al., 2000). The higher binding energy peak (O3), around 533.7 eV usually attributed to chemisorbed or dissociated oxygen or OH species on the surface of the ZnO thin films, such as CO_3, adsorbed H_2O or adsorbed O_2 (Hsieh et al., 2008). At the medium binding energy peak (O2) of the O 1s spectrum at 532.0 eV, it is associated with O^2 ions that are in oxygen-deficient Zn-O bonding matrix, and changes in the intensity of O^2 peak may explain the concentration of the oxygen vacancies (V_O) (Chen et al., 2000).

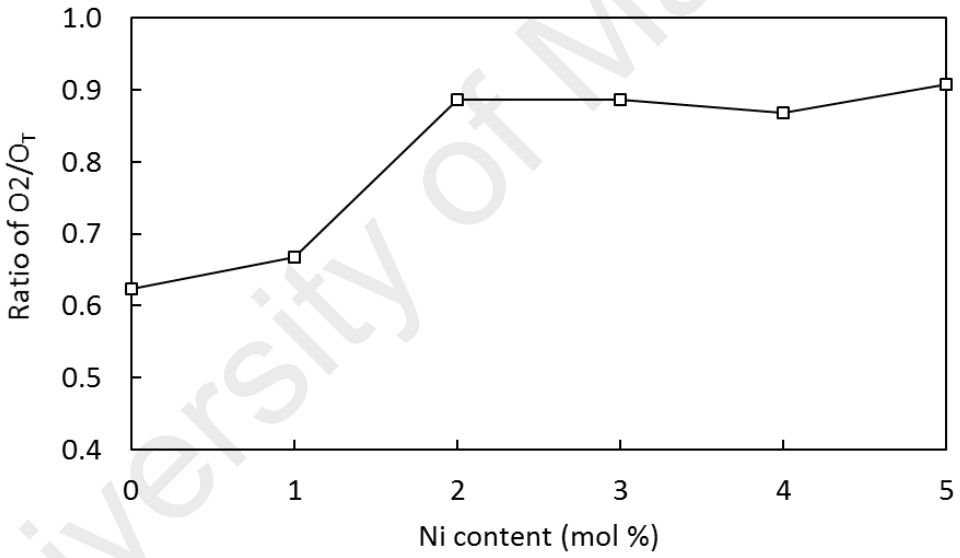

Figure 4.16: Intensity ratio of O2 component to total intensity (O_T) with respect to Ni-dopant mol percentage.

In every sample, the intensity of O2 always appears higher than the O1 component in the surface layer. This indicates the large oxygen-deficient state at the surface layer, thus at the same time is an enrichment of the Zn (or Ni) in the surface layer. The relative intensity ratio of O2 to the total O 1s is shown in Figure 4.16. It can be seen that the relative intensity of medium binding energy component O2 increases with addition of Ni-dopant, up until 2 % mol concentration before it plateaus at higher concentration of Ni.

This indicates oxygen vacancies (V_O) is increasing with Ni-dopant with an optimum concentration at 2 % mol concentration, means an oxygen-deficiency at the surface. It is well known that a more oxygen-deficient film commonly exhibits a lower resistivity (Chen et al., 2000). The resistivity and electrical characteristic of the thin films will be further discussed in Chapter 5.

4.8 Summary

Pure ZnO and Ni-doped ZnO thin films have been successfully prepared on glass substrates by a simple sol gel method, through spin coating with post heat treatment at 500 °C. The thin films growth mechanism was explained by the rapid aggregation, producing film thickness of 300 to 400 nm. Nickel have been doped in the thin films at various concentration from 0 to 5 mol percentage. It have been confirmed from the x-ray diffraction that Ni^+ substituted Zn^+ in the hexagonal crystal lattice without modifying the lattice structure. X-ray diffraction measurement gives the information on the crystal structure of the materials. All of the ZnO thin films is polycrystalline with preferred orientation is at (101) hkl plane. The best crystal quality is found to be in the 3 % Ni-doped ZnO thin film. Scherrer equation was manipulated to estimate the average crystallite size. Crystallite size of ZnO in average was around 42.0 ± 0.1 nm. HR-TEM analysis was done to 3 % Ni-doped ZnO thin films, the crystallite size and d-spacing were consistent with XRD results. Morphology of the ZnO thin films were observed from the FESEM images. All of the images show a uniform, dense and adherent film. Grain size was also estimated from the images and the ZnO grain size distribution is in the range of 50 to 70 nm in diameter. EDX measurement has been performed to analyze the element of the thin films and to validate the stoichiometry calculation. Stoichiometric balance is confirmed, it is nearly equal to the nominal stoichiometry with 0.5 % average deviation. The oxygen vacancy (V_O) at the surface layer of the thin films was investigated by deconvolution of XPS spectra. Relative intensity of V_O increases with Ni-doping.

CHAPTER 5: OPTICAL AND ELECTRICAL PROPERTIES

5.1 Overview

The effect of Ni doping in the optical and electrical properties of deposited ZnO thin films was investigated and discussed in this chapter. Optical characterizations was done using UV/Vis/NIR spectrometer to measure absorbance and transmittance, and photoluminescence (PL) spectroscopy to measure photoluminescence of the thin films. The optical band gap and the refractive index of ZnO thin films were furthermore calculated from the transmittance spectra. Electrical characterizations were done by the measurement of I-V from source measurement unit (SMU) to obtain the resistivity, and by varying the temperature in I-V measurement, the behavior of the thin films' conductivity was manipulated to obtain the activation energy.

5.2 UV/Vis/NIR Spectroscopy

The optical properties such as transmittance, absorption coefficient, and band gap energy of Ni doped ZnO thin films are determined from the variation of the optical transmission with wavelength in the range of 300 – 900 nm. Optical transmittance spectra of ZnO thin films at different Ni doping percentages are shown in Figure 5.1. All of the films exhibit high transparency; about 90 % transmittance in the visible to infrared region. Obviously, there is a sinusoidal pattern of interference fringes superimposed on the spectra. These strong interference fringes are result of multiple reflections at the interfaces (air and substrate). This is also indicating an excellent surface quality and homogeneity of the thin films (Caglar et al., 2006) which is in agreement of FESEM images in the previous chapter.

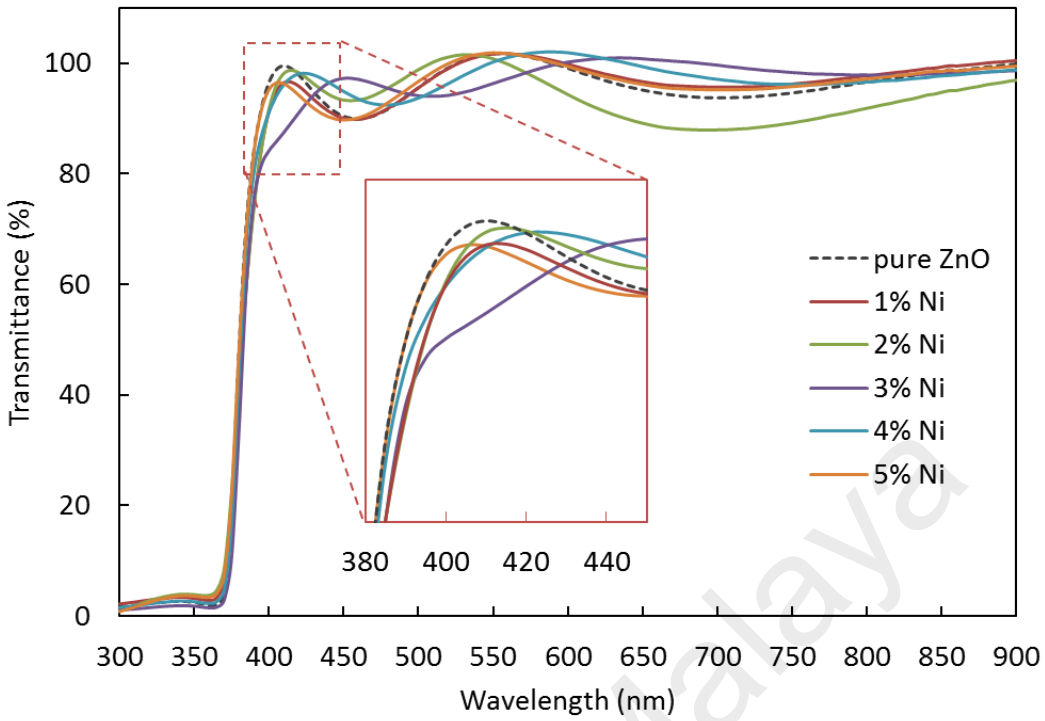

Figure 5.1: Optical transmittance spectra of ZnO thin films with different Ni-doped concentration.

Towards the ultraviolet (UV) region (wavelength < 390 nm), the transmittance of the pure and Ni-doped ZnO thin films decrease with a sharp fundamental absorption edge at 370 nm due to the direct transition of electrons from the valence band to the conduction band (Bouaoud et al., 2013). It is also observed that the visible transmittance decrease slightly at 400 nm for Ni doped ZnO films as evidenced in the inset of Figure 5.1. This might be due to the presence of Ni dopant in the ZnO matrix leading to the formation of grainy surfaces and thereby slight increase in the scattering loss (Singh et al., 2010).

From the transmittance spectra, absorption band edge can be estimated by plotting the first derivative of the transmittance spectra, $dT/d\lambda$ with respect to wavelength. The $dT/d\lambda$ vs wavelength plot is shown in Figure 5.2.

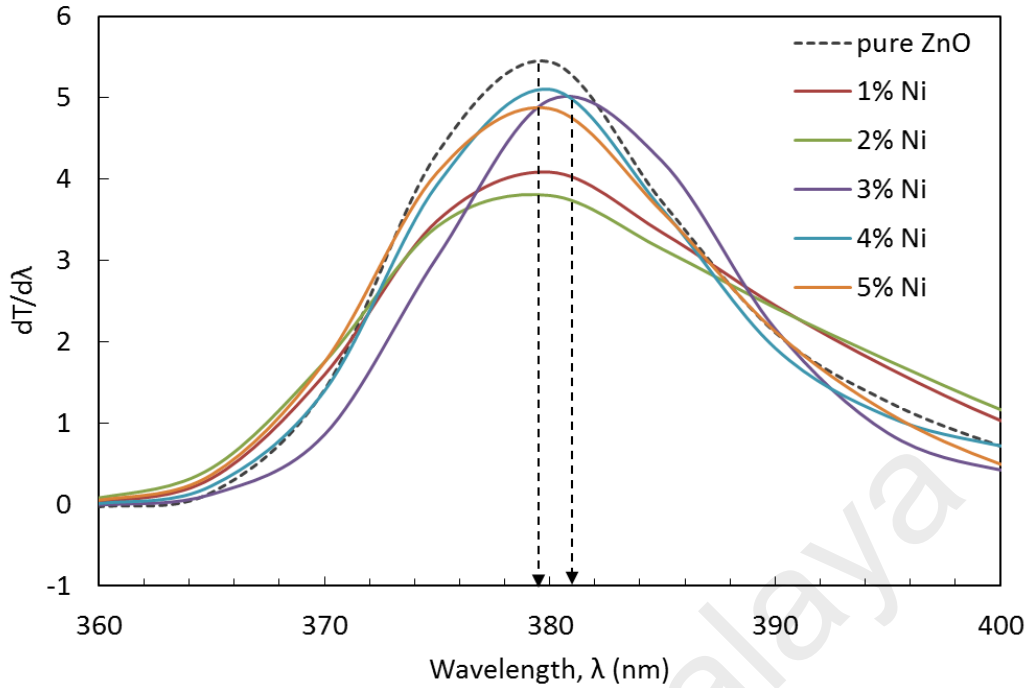

Figure 5.2: Plot of first derivative of transmittance spectra $dT/d\lambda$ versus wavelength with respect to Ni-dopant to the ZnO thin films.

The maximum peak of each spectrum indicates the absorption band edge or the optical band gap. They appear to be at 380 nm or 3.27 eV. No significant changes to the optical band gap of the films with Ni-doping except for the ZnO thin film doped with 3 % Ni concentration, the peak has shifted slightly to a higher wavelength and gives a slight different optical band gap, E_g of about 3.26 eV.

This result is consistent with previous reports (Srikant & Clarke, 1998), the nickel dopant does not create any sublevel in the electronic transition of ZnO thin film, thus does not alter the band gap. This postulates that a low doping may be insufficient to introduce a new level to the band gap.

Figure 5.3 shows the absorption spectra of the ZnO thin films with respect to Ni-doping. It can be observed that all of the ZnO thin films exhibit a strong absorption in the visible wavelength range from 350 nm to 400 nm with a shoulder peak at 360 nm. These absorption peaks present the characteristic of ZnO which is ascribed to the intrinsic band-gap absorption of ZnO due to the electron transitions from the valence band to the conduction band ($O_{2p} \rightarrow Zn_{3d}$) (Zak, et al., 2011). It is established that the optical energy

gap, E_g of most of the semiconducting materials, can be analyzed at the fundamental absorption edge in terms of band-to-band transition concept (Fujii et al., 1995; Gagandeep et al., 2000).

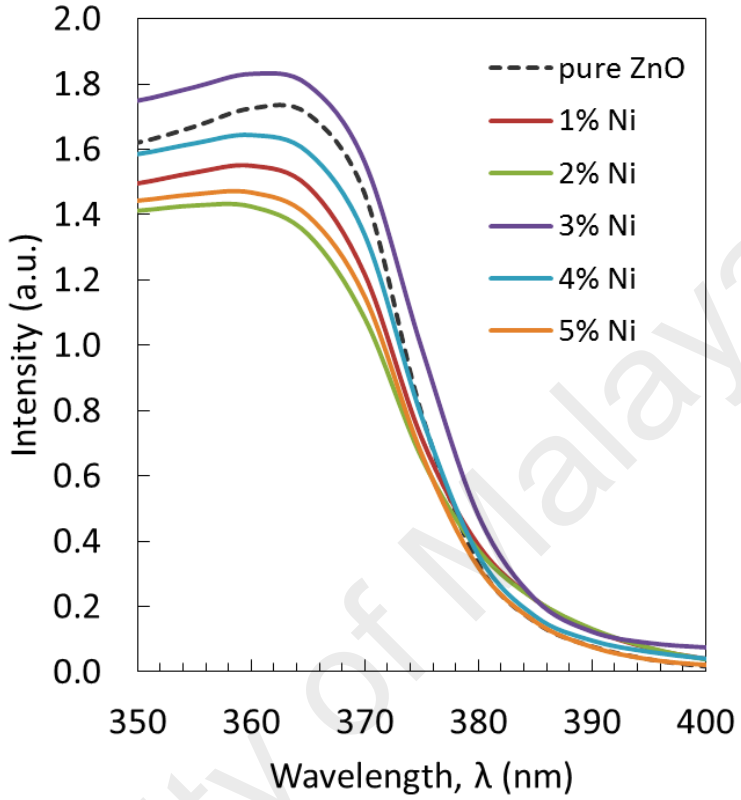

Figure 5.3: UV-Vis absorption spectra.

The optical band gap, E_g of ZnO thin films can also be calculated from Tauc's relationship. By assuming that the absorption edge tends to possess a parabolic relation with the photon energy (Muhammad & Sulaiman, 2011; Souri, 2011), Tauc's relationship can be denoted as,

$$\alpha hv = \alpha_0 (hv - E_g)^n \tag{5.1}$$

with α is the absorption coefficient, α_o is an energy-independent constant and n is a value to determine the type of the involved optical transition, in which n = ½ or 0.5 is the direct allowed optical transition while n = 2 is the indirect allowed transition. Note that the absorption coefficient, α can be obtained from the ratio of the absorbance, A to the film thickness, t values. It can be written as,

$$\alpha = \frac{2.303A}{t} \tag{5.2}$$

Moreover, the derivation of equation above can be expressed as:

$$\frac{d\ ln(\alpha hv)}{d\ hv} = \frac{n}{hv - E_g} \tag{5.3}$$

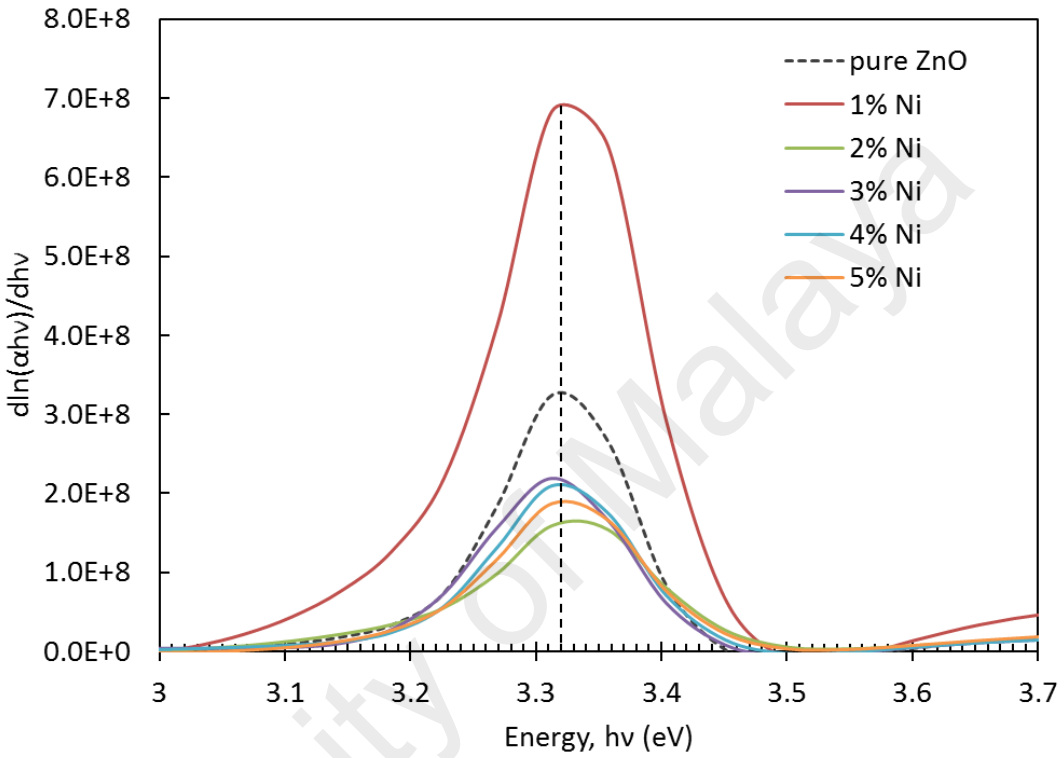

Figure 5.4: Plot of derivation of dln*(αhv)/dhv* versus ln *(hv-E_g)*.

The differentiated characteristic of ln (*αhv*)/*dhv* as a function of *hv* is displayed in Figure 5.4. From Equation 5.3, the approximate value of the optical band gap E_g can be obtained from the maximum value of the plot. The value of E_g is ~3.32 eV. Considering this value, a plot of ln (*αhv*) versus ln ($hv - E_g$) is plotted as shown in Figure 5.5(a). It is found that the calculated value of the slope, *n* is estimated as 0.5 for all of ZnO thin films. This estimation provides evidence for the direct energy transition of the energy band gap in ZnO and Ni doped ZnO thin films which is in agreement with the other findings of the undoped ZnO and doped ZnO (Norton et al., 2004; Olson et al., 2007; Xiang et al., 2009; Zak, Razali, et al., 2011).

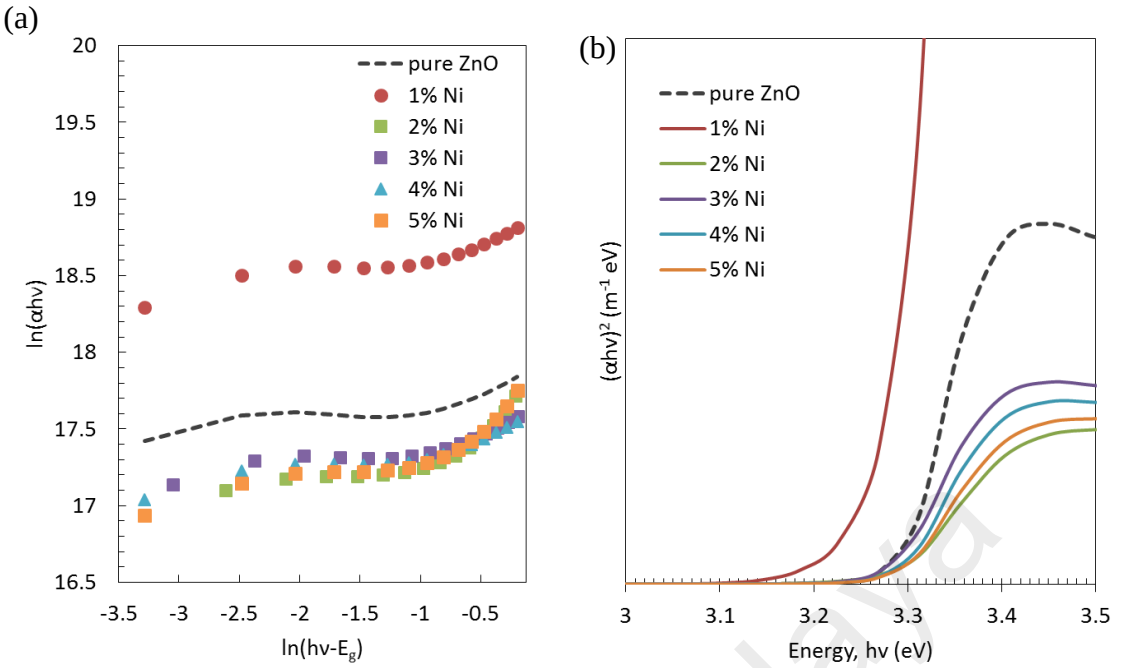

Figure 5.5: (a) Graph of ln (αhv) versus ln (hv-E_g) and (b) graph of $(\alpha hv)^2$ versus photon energy, hv.

In order to evaluate the value of E_g more precisely, a graph of $(\alpha hv)^2$ against hv has been plotted as well, as shown in Figure 5.5(b). The value of E_g was calculated by extrapolating the straight line towards the x-axis of the plot. The optical band gap, E_g for all ZnO thin films is around 3.23 to 3.26 eV. All the calculated value of E_g determined from transmittance and absorption spectra are given in Table 5.1.

Table 5.1: The values of energy band gap for Zno thin films with different Ni-dopant concentration.

Ni content %	**Function**		
	$dT/d\lambda$	$d(\alpha hv)/dhv$	$(\alpha hv)^2$
	E_g **(eV)**	E_g **(eV)**	E_g **(eV)**
0	3.27	3.32	3.30
1	3.27	3.32	3.27
2	3.28	3.33	3.29
3	3.26	3.31	3.29
4	3.27	3.32	3.30
5	3.27	3.32	3.28

From the table, average E_g from each function is 3.27, 3.32 and 3.29 eV for $dT/d\lambda$ estimation, $d(\alpha hv)/dhv$, and $(\alpha hv)^2$ function respectively. The average value of E_g is about 3.30 ± 0.02 eV. The optical energy band gap (E_g) of the ZnO thin film does not affected by the addition of Ni-dopant. As mentioned before, this may lead to the postulation of low doping is insufficient to introduce sublevel to the electronic transition of ZnO band gap, thus does not modify the band gap (Srikant & Clarke, 1998).

Furthermore, optical properties of any materials are strongly dependent on the refractive index (n) and the extinction coefficient (k). These constants were determined from the measured transmittance, where the refractive indices, n at various wavelengths were calculated using equation given as (Manifacier, et al., 1976),

$$n = [N + (N^2 - n_0^2 n_1^2)^{\frac{1}{2}}]^{1/2} \tag{5.4}$$

where,

$$N = \frac{n_0^2 + n_1^2}{2} + 2n_0 n_1 \frac{T_{max} - T_{min}}{T_{max} T_{min}} \tag{5.5}$$

n_1 is the refractive index of the glass substrate, and n_0 is the air's refractive index. n is explicitly determined from T_{max}, T_{min}, n_1 and n_0 at the same wavelength. The method that was proposed by Manifacier consisting of T_{min} and T_{max} as continuous functions of wavelength, λ. These functions are the envelope maxima $T_{max}(\lambda)$ and minima $T_{min}(\lambda)$ in the transmission spectra as shown in figure below.

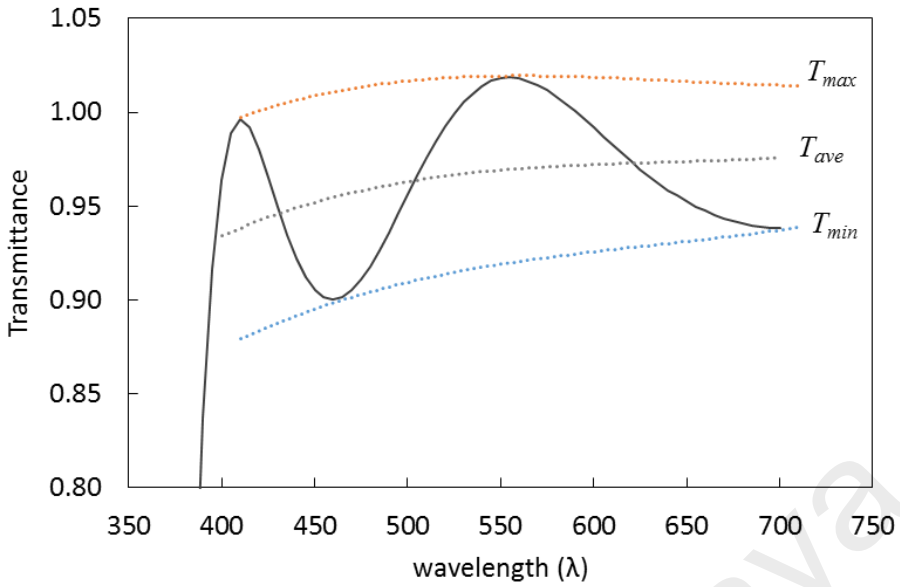

Figure 5.6: Transmittance spectrum of pure ZnO thin film with envelope maxima and minima.

As an example from the transmittance spectrum of pure ZnO thin film in Figure 5.6, the T_{max} and T_{min} are obtained from the envelope of interference fringes of the transmittance spectrum, in the visible range. So, these $T_{max}(\lambda)$ and $T_{min}(\lambda)$ function is applied in Equation 5.5, to calculate the refractive index, n. The spectral dependence of refractive index, $n(\lambda)$ of ZnO thin films are plotted in Figure 5.7 with respect to Ni-doping percentage.

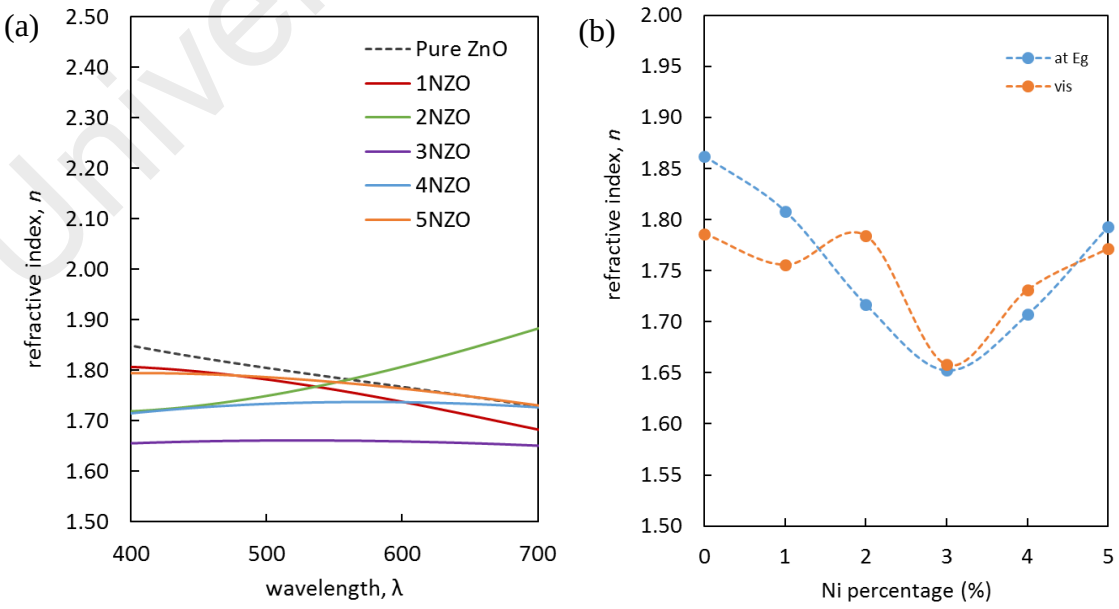

Figure 5.7: (a) Spectral dependence plot of ZnO thin films refractive indices, n versus wavelength λ and (b) average refractive index, n at different Ni-doping percentage.

Figure 5.7(a) shows the magnitude of *n* at wavelength range of 350 and 800 nm (visible spectrum), with different Ni-doping percentage. The refractive indices, n are observed varies between 1.65 and 1.92. Value of refractive index, *n* decreases with the increase of wavelength for all thin films except for ZnO with 2 % Ni doping, where *n* increases at higher wavelength. This is consistent with the trend reported by Benouis et al (Benouis et al., 2010) where the decrease in n correlates with the corresponding increase in transmittance (Hsu et al., 2005), whereas the slight increases in the 2 % Ni ZnO is also corresponding to the decrease in its transmittance. In Figure 5.7(b), *n* values at 374 nm (in blue) and at average visible range (in red), are plotted with respect to percentage of Ni-doping. At the band gap wavelength, refractive index of pure ZnO is 1.86. The value decreases to 1.66 with 3 % Ni-doping percentage, and it increases to 1.79 with higher Ni-doping percentage. These values are in the same range as reported by others; around 1.7 – 2.2 (Xie et al., 2012). Summary of the refractive indices at the band gap wavelength (E_g) and as the average in the visible spectrum are tabulated in the Table 5.2.

Table 5.2: Index refraction, *n* of ZnO thin film with different Ni-doping percentage concentration.

Ni content (%)	***n* (visible range) (±0.01)**	***n* (at E_g) (±0.01)**
0	1.79	1.86
1	1.76	1.81
2	1.78	1.72
3	1.66	1.65
4	1.73	1.71
5	1.77	1.79

5.3 Photoluminescence

The photoluminescence or PL measurement provides information on electronic structure of materials, by measuring the transitional energy. PL spectra of deposited pure and Ni-doped ZnO thin films are shown in Figure 5.8. As a reference for an absorption edge, an excitation energy at 280 nm was used for PL measurement. From the figure, it can be observed that all thin films demonstrate a broad band emission in the visible wavelength ranging from 350 nm to 550 nm. The emission characteristics are related to the radiative recombination among point defects in the ZnO lattice, such as oxygen vacancy, zinc vacancy, oxygen interstitial, zinc interstitial, and anti-site defect. It can be noted that the undoped ZnO film exhibit a prominent peak at 416 nm which is considerably consistent with the other reports (Djurišić et al., 2004; Fan et al., 2005; Shen et al., 2005).

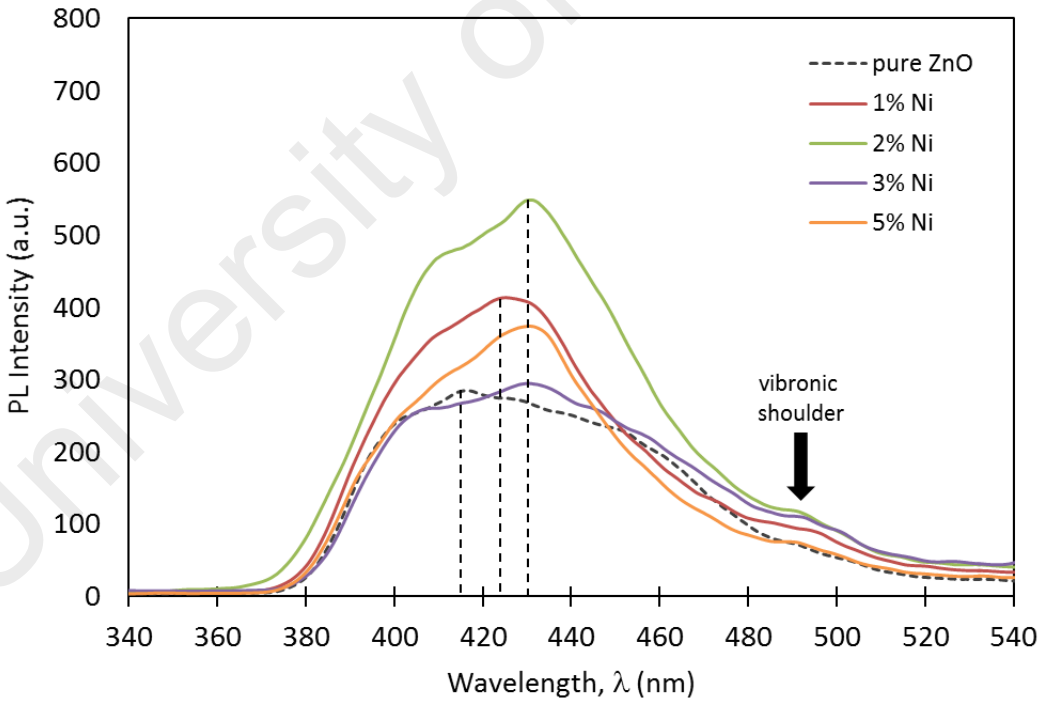

Figure 5.8: Photoluminescence spectra of ZnO thin film with different Ni-doping percentage.

This 416 nm violet emission is also reported by Jeong et al., 2003, when they measured the peak in a wavelength range between 413 and 424 nm. This is believed by the author, to be originated from the Zn vacancies of the sample. Jin et al., 2000 has also deduced

that their violet emission displayed at 420 nm wavelength is probably due to radiative defects from the interface traps which exist at the grain boundaries. The radiative transition between this level and the valence band has resulted in the violet luminescence (Jin et al., 2000).

Upon Ni doping, the dominant peaks are slightly shifted towards a longer wavelength, which can be seen in Figure 5.8. The peak at 416 nm for pure ZnO thin film has shifted to 426 nm for the 1 % doped Ni and even to a longer wavelength of 432 nm with that of 2 % doped Ni and higher. According to the shifting of PL peak to a longer wavelength, it can be interpreted that the emitted energy has been reduced. The photo excitation and the emission phenomena are been summarized with a schematic diagram of energy band gap as shown in Figure 5.9.

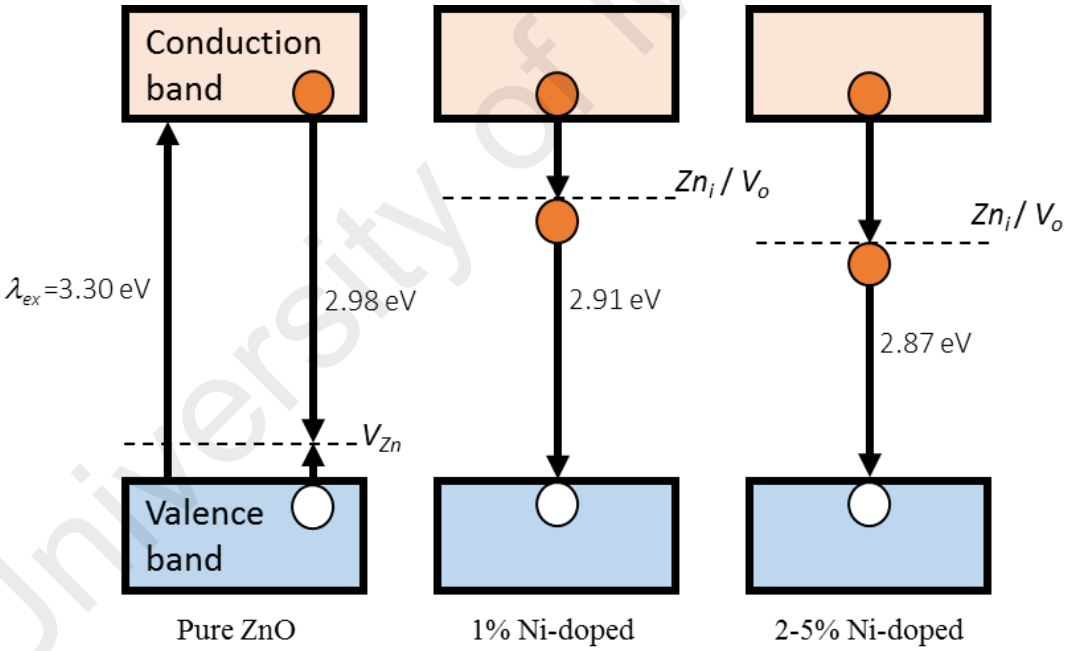

Figure 5.9: A schematic energy band diagram of PL emissions, originated due to electronic transitions between different defect levels and band edges of Ni-doped ZnO thin films.

This phenomenon is explained to be due to the merging of an impurity band into the energy band gap. The hybridization between states of the ZnO matrix and of the Ni dopant leading to the formation of such impurity band and thereby gives rise to new donor electronic states just below the conduction band (Mondal, et al., 2013). Such formation

of donor levels contradicts the Burstein–Moss effect and results in the narrowing of the effective energy gap of Ni-doped ZnO thin films as obtained from PL measurement (Mondal et al., 2013).

This position variation of the emission peak or the narrowing of the effective energy gap may be related to the defects or stoichiometry in the ZnO film (Fan et al., 2005). In other work, Sun, 2000 calculated the energy levels of various intrinsic defects in ZnO; the draft was shown in Figure 5.10. From Sun's calculation, it can be deduced that that the violet emission of PL spectra of the ZnO thin films be attributed to the energy transition of electronics from the upside of the valence band to the interstitial zinc (Zn_i) level as well as to the energy transition of electronics from the bottom of the conduction band to the zinc vacancy (V_{Zn}) level (Sun, 2000). The interstitial zinc (Zn_i) should be the main defects in deposited ZnO film. The concentration of the interstitial zinc (Zn_i) and zinc vacancy (V_{Zn}) defects in ZnO films depended strongly on annealing temperature and oxygen pressure (Fan et al., 2005). In this work, the annealing temperature is 500 °C, which is higher than the melting point of metal Zn, 419 °C that may lead to the interstitial zinc and zinc vacancy defect.

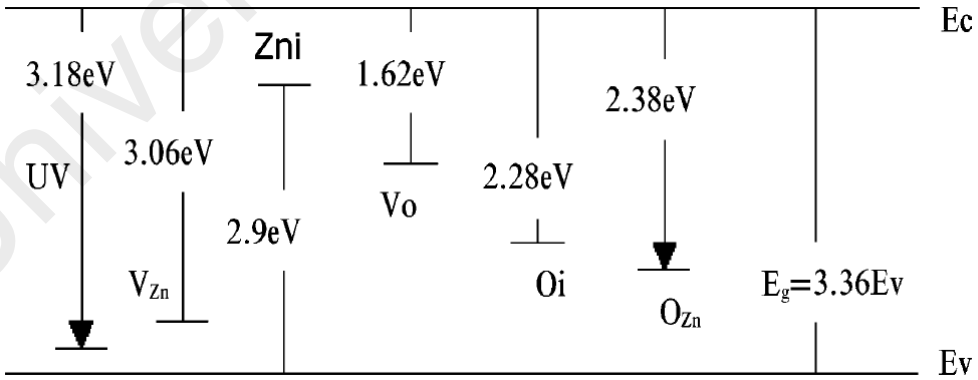

Figure 5.10: Draft of calculated defect's level in ZnO thin film (Fan et al., 2005).

In addition from the PL results in Figure 5.8, a pronounced vibronic shoulder is also observed at 495 nm for the undoped and Ni doped ZnO thin films suggesting the presence of oxygen vacancies in these thin films, consistent with the XPS results discussed in

Section 4.7 (Gao & Wang, 2005; Roy et al., 2003). In Figure 5.11, oxygen vacancies ratio to the total oxygen in the sample is plotted at different Ni-doping percentage. At the same axis, the PL peaks position are also plotted. It can be seen that the oxygen vacancies and the peak position follow a similar trend. As the Ni-doping increases, the oxygen vacancies increases, and the PL position shift to a longer wavelength until 2 % of Ni-doping before it reaches a saturated value. From this observation, the different in the effective energy gap can also be originated from the oxygen vacancies defect. Oxygen vacancies (V_O), zinc vacancies (V_{Zn}), oxygen interstitials (O_i) and zinc interstitials (Zn_i) may be the most probable defects that occur in ZnO nanostructures. Mostly, in the electronic transition between defect levels, the main donor defects are Zn_i, Ni_i and V_O while acceptor defects include V_{Zn} and O_i (Ashokkumar & Muthukumaran, 2015),

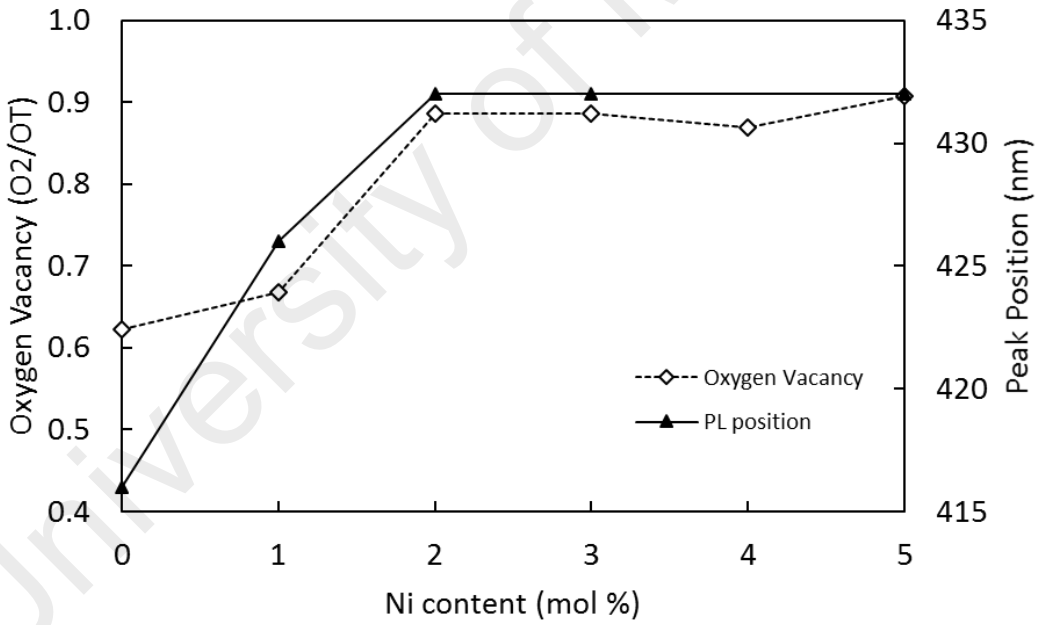

Figure 5.11: PL peak position and oxygen vacancies ratio to total oxygen, with respect to the Ni-doping percentage.

5.4 Electrical Characteristics

The sheet resistance (R_s) of ZnO thin films in this work is measured by conventional two probes I-V measurement with an aid of aluminum electrodes deposited on top of the thin films to improve the electrical contact. Resistivity of the thin films, with thickness *t* can be determined by,

$$\rho = R_s t \tag{5.6}$$

Prior to the calculation of the resistivity of the thin film, a current-voltage measurement at room temperature has been performed to measure the sheet resistance, R_s. Voltage applied was swept from 0 V to 50 V, and the measured current is in the magnitude of ~10^{-4} A. In Figure 5.12, the log *I* vs log *V* graph is plotted at a different percentage of Ni-doping. Before the sheet resistance (R_s) can be calculated, the ohmic region for each sample is determined. From the log *I* vs log *V* plot, ohmic region has a slope m = 1, where every sample is ohmic between 2 V and 8 V. Thus, the sheet resistance R_s, was measured in this range; 2 – 8 V.

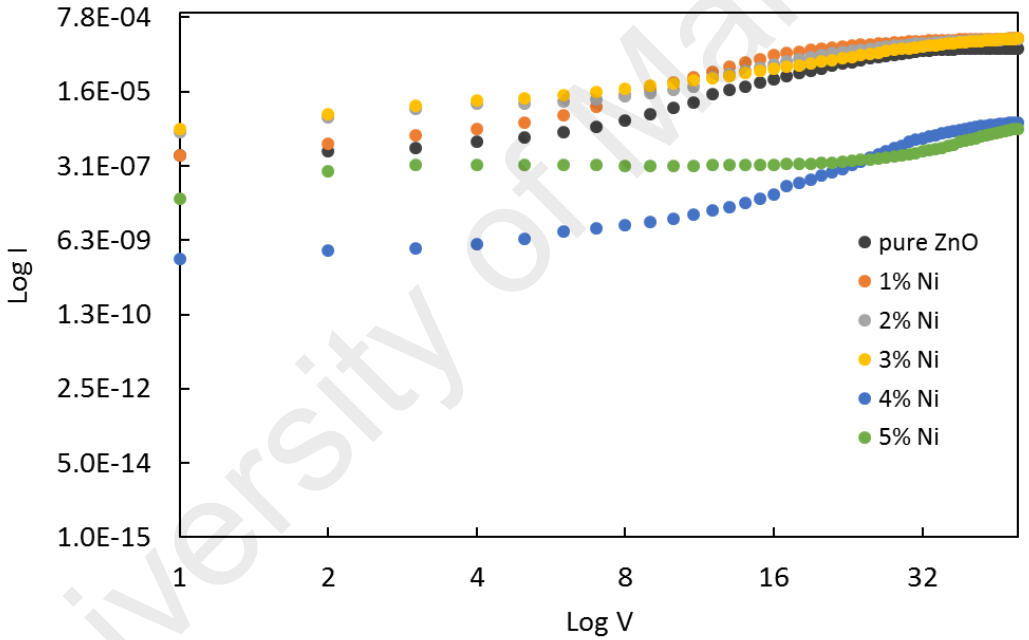

Figure 5.12: Log *I* versus *V* plot of ZnO thin films with different Ni percentage.

Resistivity ρ of ZnO thin films is calculated from Equation 5.6, with R_s obtained from the I-V curve and the thickness *t* was obtained as described in Section 4.2. The ρ values for each sample are tabulated in Table 5.3.

Table 5.3: Resistivity of ZnO thin films with different Ni-doping mol percentage.

Ni-doping (%)	**0**	**1**	**2**	**3**	**4**	**5**
Resistivity, ρ (±0.01) (Ω cm)	353.94	50.43	28.16	17.04	393.73	280.28

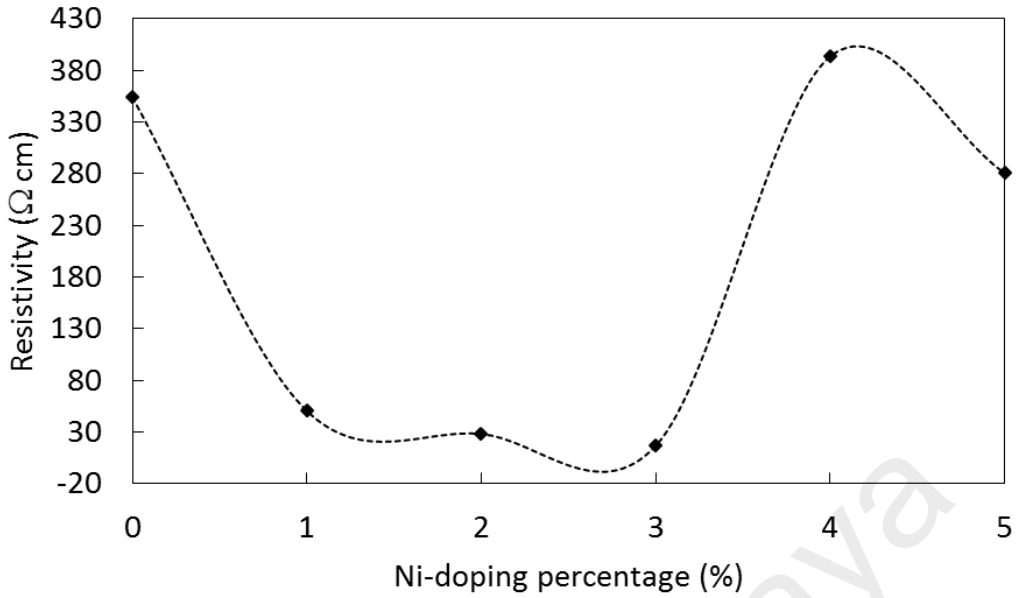

Figure 5.13: Resistivity of pure ZnO and Ni-doped ZnO thin films.

Figure 5.13 shows the variation of the resistivity of ZnO thin films deposited on glass substrate by sol-gel spin coating, as a function of Ni-doping percentage. The pure ZnO thin film has a resistivity of 353.94 Ω cm. With Ni-doping, the resistivity of the ZnO thin film dropped to the lowest resistivity of 17.04 Ω cm for 3% Ni-doped ZnO. Further increase in Ni-doping percentage, the resistivity value starts to increase significantly. This resistivity result is consistent with the work from Shrestha et al., 2010 where in their report, Al-doped ZnO thin films were prepared using the same sol gel spin coating technique, the resistivity decreases until 2 at % of Al and increases drastically at higher Al concentration.

The decrease in resistivity with Ni doping can be attributed to the increase in carrier concentration and also to the increase in mobility. After doping concentration exceed 3 at %, the mobility decreases drastically. Therefore, the increase in resistivity can be attributed to change in carrier mobility. At a small amount of Ni-doping percentage, Ni atoms occupy the Zn atoms sites in ZnO matrix. When the concentration was increased above 3 mol percentage, the resistivity of the film increases. This is because the doping concentration may exceeded the solid solution limit, that the Ni atom does not occupy the

lattice sites, but forms a kind of neutral defect, instead. These neutral Ni do not contribute to free carrier concentration, thus at high doping level the neutralized Ni atoms result in a disorder in the lattice. They act as a scattering center that increase the resistivity (Shrestha et al., 2010).

Current voltage (I-V) measurements of the thin films have also been carried out at different temperature from 300 to 473 K in order to determine the activation energy E_a. Figure 5.14 shows a graph of log I vs V at different temperature from 303 to 473 K. This is an I-V measurement at different temperature for 1 % Ni-doped ZnO thin film. The voltage was swept from 0 V to 50 V. From Figure 5.14, the highest current measured for 1% Ni-doped ZnO thin film is around ~10^{-3} A.

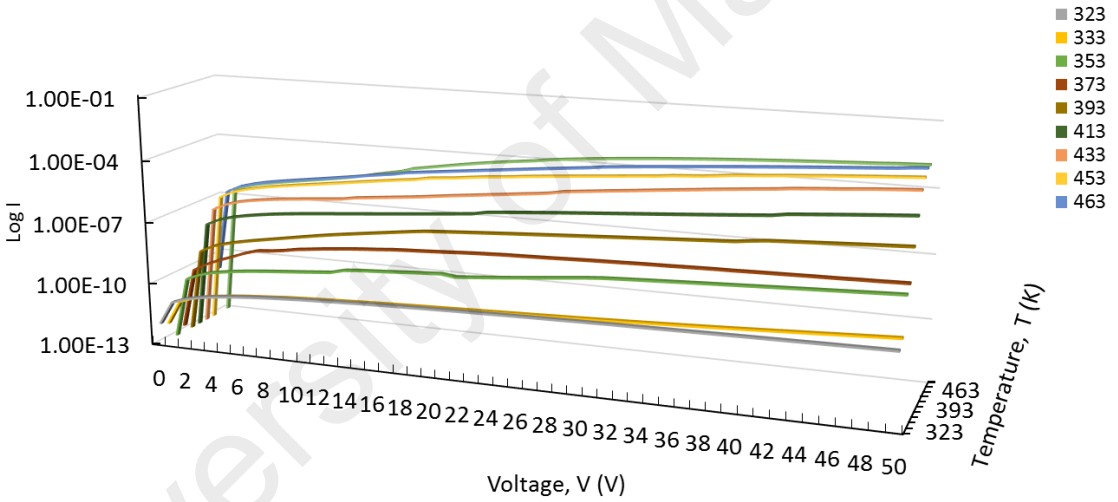

Figure 5.14: Log *I* vs *V* at several temperature for 1 % Ni-doped ZnO thin film.

The temperature dependence of conductivity for semiconductor materials can be expressed by using Arrhenius equation:

$$\sigma = \sigma_o \exp(-E_a/kT) \tag{5.7}$$

where σ is the electrical conductivity at temperature T, σ_o is the exponential pre-factor, k is the Boltzmann constant and E_a is the activation energy. Activation energy, E_a is the additional energy the reactant molecules need to form activated complex for the reaction. It is the difference in energy of activated state and reactant (Kakati et al., 2010). In

semiconductors, activation energy is the potential barrier or energy barrier that need to be overcome by the charge carrier to hop from one site to another. The Arrhenius plot is shown in Figure 5.15. It is observed that the pure ZnO thin films (orange dots) in Figure 5.15(b) exhibit increase in conductivity as temperature increases until 418 K. The conductivity slightly decreases at temperature higher than 418 K. This behavior indicates the semiconductor nature and thermally activated conductivity of the ZnO thin films. With Ni-doping, the Arrhenius plot of ZnO thin films can be separated to two region of negative-slope linear behavior as shown in Figure 5.15(b) where the E_a of 2 % Ni-doped ZnO can be divided in region below 373 K and above 373 K. This is similar to Sheeba's work (Sheeba et al., 2016) where their Sb-doped ZnO thin films give two temperature region of activation energy.

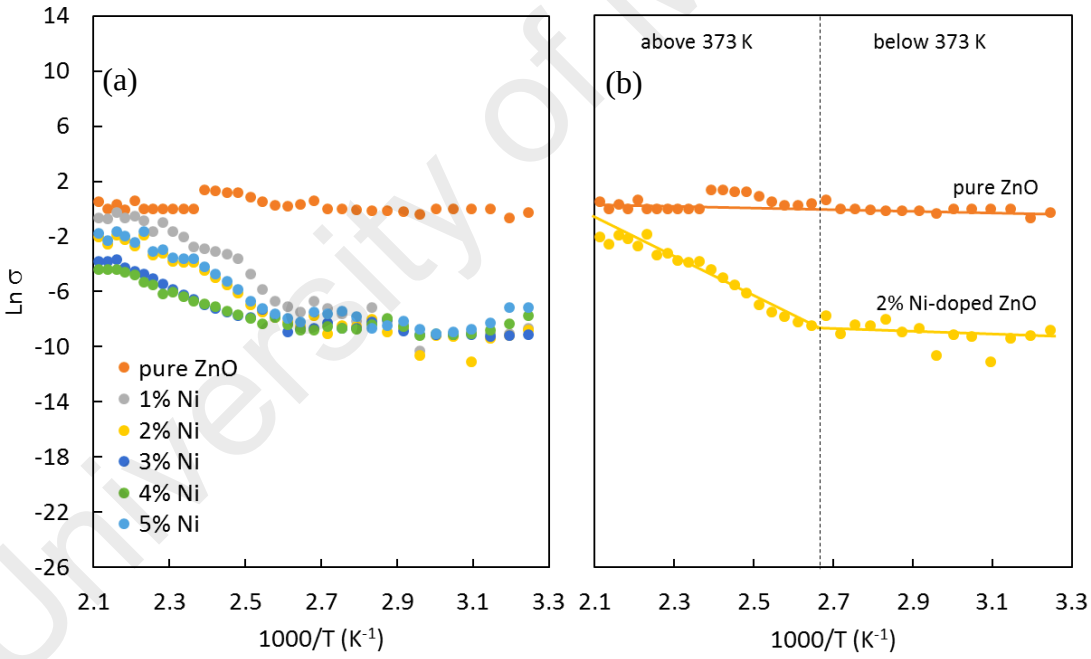

Figure 5.15: Temperature dependence of dc conductivity (σ) of (a) ZnO thin films at different Ni-doping percentage and (b) dc conductivity of 2 % Ni-doped ZnO thin film at two different temperature region is compared to pure ZnO behavior.

The slope of the conductivity-temperature plot (ln σ vs 1000/T), is the activation energy E_a of electronic transport for this semiconducting materials. The activation energy E_a values calculated from the slope of the graphs is between 0.7 to 15.1 eV for region below and above 373 K respectively. The summary of the calculated activation energy

(E_a) and the pre-exponential factor ($ln\ \sigma_o$) of ZnO thin film with different Ni-doping percentage, in two different temperature region (above 373 K, and below 373 K) is tabulated in Table 5.4.

Table 5.4: The activation energy, and the pre-exponential factor of undoped and Ni-doped ZnO thin films at two different temperature region.

Ni-doping (%)	Activation energy, E_a (± 0.1) eV		$ln\ \sigma_o$ (± 0.1)	
	above 373 K	below 373 K	above 373 K	below 373 K
0	1.3	1.3	11.3	4.1
1	15.1	3.1	32.8	0.7
2	13.7	3.6	27.8	1.4
3	9.5	1.4	16.3	-4.7
4	8.6	0.7	13.9	-6.7
5	14.4	2.7	29.9	-0.6

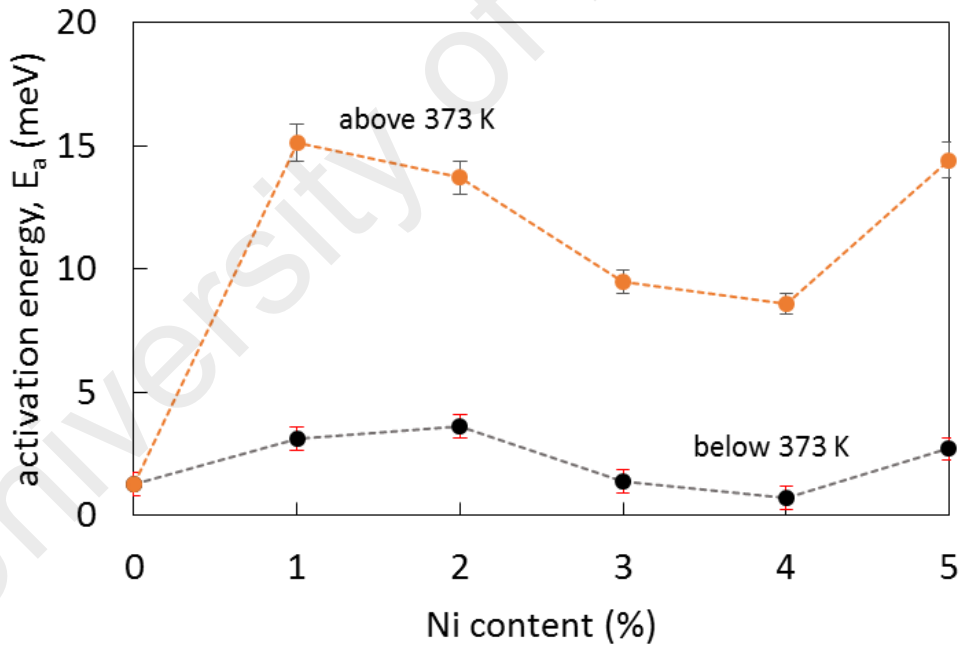

Figure 5.16: Activation energy of ZnO thin films at different Ni-doping percentage.

In particular, the pure ZnO presents an activation energy E_a of 1.3 eV for all region of temperature measured. E_a increases with Ni-doping for both region of temperature, for instant the ZnO thin film with 2 Ni at % has an activation energy of 3.6 eV below 373 K while 13.7 eV above 373 K. All Ni-doped ZnO thin films has an inflection point at temperature of 373 K. Thus basically, the electron concentration in the ZnO thin films

increases by the nickel doping. The behavior of activation energy of undoped and Ni-doped ZnO thin films are presented in Figure 5.16. In the region below 373 K, the activation energy E_a of ZnO thin film increases with Ni-doping until 2 %. E_a decreases at 3 to 4 % of Ni-doping, and increases at 5 %. This trend is similar to the temperature region above 373 K, E_a increases at 1 % of Ni-doping, it decreases at higher doping until 4 at % and increases at 5 %. This is consistent with the work done by Gonzalez et al., 1998, where the doping of aluminum has increased the activation energy of deposited ZnO films, by increasing the electron concentration. Their trapping levels with activation energy under 55 meV contribute to the electrical conductivity with a very low energy cost, thus improving the conductivity aluminum doped ZnO thin films (Gonzalez et al., 1998).

5.5 Summary

Effects of Ni dopant on optical and electrical properties of deposited ZnO thin film have been investigated. The optical transmittance of all of the ZnO thin film were obtained above 85 % transparency. The average calculated optical band gap obtained from the absorption spectra is 3.30 eV, where nickel doping does not significantly alter the optical band gap of the ZnO thin films. The obtained energy band gap is consistent with the commercial ZnO (3.30 eV) with deviation of 0.6 %. The index refraction calculated from the transmittance spectra is between 1.60 and 1.90. Nickel doping reduces the refractive index until a minimum point at 3 % of Ni with the lowest index at 1.65 ± 0.01. Photoluminescence of the samples was measured, and all films exhibit a broad PL emission. The peak of PL emission of pure ZnO thin film centered at 413 nm wavelength. This PL peak is slightly shifted to longer wavelength with nickel doping. This attributes to the formation of sublevel in the ZnO thin films that may resulted from the defects from the interstitial zinc (Zn_i), zinc vacancy (V_{Zn}) and oxygen vacancy (V_O). The electrical resistivity was measured by using the two probes I-V measurement. Resistivity of pure

ZnO thin film measured was 35.4 x 10^1 Ω cm. Nickel doping reduces the resistivity to 1.7 x 10^1 Ω cm at an optimum mol percentage of 3 %. The activation energy (E_a) of ZnO thin film is found to be 1.3 eV. E_a value increases up to 15.1 eV above 373 K, when Ni-doping was introduced.

CHAPTER 6: CONCLUSIONS AND FUTURE WORKS

6.1 Conclusion

In general, this thesis has discussed the formation of the prepared ZnO thin films through morphological and structural analysis, and the effect of nickel-doping to the optical and electrical properties of the thin films.

ZnO thin films with different Ni-doping concentration have been successfully prepared on top of glass substrate by sol-gel process and spin coating method. The average thickness of the deposited thin films is about 300 to 400 nm, and their growth mechanism was explained by rapid aggregation process. The chemical systems used to develop ZnO thin films are summarized in Table 6.1.

Table 6.1: Chemical systems used for zinc oxide thin films development, resulting thickness and crystallographic orientation.

Precursor (mol L^{-1})	Zinc acetate dihydrate (ZAD) (0.5 M)
Solvent	Ethanol
Additive (ratio)	Diethanolamine (DEA) (1:1)
Aging time (hour)	24
Substrate	Glass
Pre-heat treatment (°C)	200
Post-heat treatment (°C)	500
Thickness (nm)	300 – 430
Crystal orientation	(100), (002), (101)

The deposited ZnO thin film is polycrystalline with three strong diffraction peaks (100), (002), and (101) indicating hexagonal wurtzite structure. The preferred orientation is (101) hkl plane. Average crystallite size was 46.0±0.1 nm, while the grain size distribution is 70 nm. For transparent electronics applications, the optical and electrical properties of ZnO thin films have been investigated. The transparency of pure ZnO thin film was above 85 %. Optical band gap (E_g) and the refractive index (n) have been calculated from the transmittance measurement of ZnO thin film. The calculated E_g and

n are 3.3 eV and 1.86 respectively. The deposited ZnO thin film exhibit a broad photoluminescence peak at 416 nm. This violet emission was believed to be originated from the Zn vacancies of the thin film. The electrical resistivity of the thin films was calculated from the I-V measurement. Pure ZnO thin film has resistivity of 35.4 x 10^1 Ω cm. From temperature-dependent of I-V measurement, the activation energy of ZnO thin film is found to be 1.3 eV.

Doping with nickel does not change the crystal structure as Ni^+ substituted Zn^+ in its hexagonal crystal lattice. The presence of nickel element was confirmed by EDX analysis, and the stoichiometric balance was proven with average deviation of 0.5 %. All of the ZnO thin films are polycrystalline with (101) hkl preferred orientation. ZnO with 3 % of Ni has the best crystal quality. Average crystallite size for Ni-doped ZnO thin films was around 42.0 ± 0.1 nm, and the grain size distribution is in 50 to 70 nm range of diameter. At the surface layer of the ZnO thin films, the oxygen vacancy was found to increase with Ni-doping. All deposited ZnO thin films have transparency above 85 %, with average calculated band gap of 3.30 eV. These two quantities were not affected by the addition of Ni-doping. The calculated refractive index values are between 1.60 and 1.90 where Ni-doping reduces the refractive index until a minimum point as exhibited by 3 % Ni-doping (1.65 ± 0.01). The measured photoluminescence peak at 416 nm for pure ZnO thin film was shifted to a longer wavelength with Ni-doping. This attributes to the formation of sublevel in the ZnO thin films that may resulted from the defects from the interstitial zinc (Zn_i), zinc vacancy (V_{Zn}) and oxygen vacancy (V_O). Electrical resistivity of ZnO thin films was improved with Ni-doping. The minimum resistivity was 1.7 x 10^1 Ω cm exhibited by ZnO thin film with 3 % Ni-doping. Activation energy increases with Ni-doping up to 15.1 eV at temperature above 373 K.

6.2 Future Works

In order for Ni-doped ZnO thin film to be applied as a transparent electronics devices, the transparency and electrical resistivity must be compatible to other available transparent materials. Thus, obviously from this work the resistivity need to be improved. In future, more work is needed to be concerned to obtain optimum parameter for enhancing the growth of ZnO thin film through sol-gel method. In the synthesis process, the chemical system can be controlled with different precursor, solvent or additive. This is crucial in producing the preferred orientation of the crystal structure.

In optical characterization, a reflectance measurement can be done in the future to understand the optical constant. For electrical measurement of thin film, four-point probes Hall-effect measurement can be adopted to measure a more precise resistivity.

REFERENCES

Abed, S., Aida, M. S., Bouchouit, K., Arbaoui, A., Iliopoulos, K., & Sahraoui, B. (2011). Non-linear optical and electrical properties of ZnO doped Ni Thin Films obtained using spray ultrasonic technique. *Optical Materials, 33*(6), 968-972.

Agura, H., Suzuki, A., Matsushita, T., Aoki, T., & Okuda, M. (2003). Low resistivity transparent conducting Al-doped ZnO films prepared by pulsed laser deposition. *Thin Solid Films, 445*(2), 263-267.

Armelao, L., Fabrizio, M., Gialanella, S., & Zordan, F. (2001). Sol–gel synthesis and characterisation of ZnO-based nanosystems. *Thin Solid Films, 394*(1), 89-95.

Ashokkumar, M., & Muthukumaran, S. (2015). Effect of Ni doping on electrical, photoluminescence and magnetic behavior of Cu doped ZnO nanoparticles. *Journal of Luminescence, 162*, 97-103.

Bacaksiz, E., Parlak, M., Tomakin, M., Özçelik, A., Karakız, M., & Altunbaş, M. (2008). The effects of zinc nitrate, zinc acetate and zinc chloride precursors on investigation of structural and optical properties of ZnO thin films. *Journal of Alloys and Compounds, 466*(1), 447-450.

Bae, S. H., Lee, S. Y., Kim, H. Y., & Im, S. (2001). Effects of post-annealing treatment on the light emission properties of ZnO thin films on Si. *Optical Materials, 17*(1), 327-330.

Bang, S., Lee, S., Ko, Y., Park, J., Shin, S., Seo, H., & Jeon, H. (2012). Photocurrent detection of chemically tuned hierarchical ZnO nanostructures grown on seed layers formed by atomic layer deposition. *Nanoscale Research Letters, 7*(1), 1.

Bao, D., Gu, H., & Kuang, A. (1998). Sol-gel-derived c-axis oriented ZnO thin films. *Thin Solid Films, 312*(1), 37-39.

Bardeen, J., & Brattain, W. H. (1948). The transistor, a semi-conductor triode. *Physical Review, 74*(2), 230.

Benouis, C., Benhaliliba, M., Juarez, A. S., Aida, M., Chami, F., & Yakuphanoglu, F. (2010). The effect of indium doping on structural, electrical conductivity, photoconductivity and density of states properties of ZnO films. *Journal of Alloys and Compounds, 490*(1), 62-67.

Bian, J., Li, X., Gao, X., Yu, W., & Chen, L. (2004). Deposition and electrical properties of N–In codoped p-type ZnO films by ultrasonic spray pyrolysis. *Applied Physics Letters, 84*(4), 541-543.

Blatter, G., & Greuter, F. (1986). Electrical breakdown at semiconductor grain boundaries. *Physical Review B, 34*(12), 8555.

Bouaoud, A., Rmili, A., Ouachtari, F., Louardi, A., Chtouki, T., Elidrissi, B., & Erguig, H. (2013). Transparent conducting properties of Ni doped zinc oxide thin films

prepared by a facile spray pyrolysis technique using perfume atomizer. *Materials Chemistry and Physics, 137*(3), 843-847.

Brown, H. E. (1978). Zinc Oxide--Properties and Applications. *International Lead Zinc Research Organization, Incorporation, New York. 1978, 218 p*.

Caglar, M., Caglar, Y., & Ilican, S. (2006). The determination of the thickness and optical constants of the ZnO crystalline thin film by using envelope method. *Journal of Optoelectronics and Advanced Materials, 8*(4), 1410.

Callister, W. D. (2007). *Materials science and engineering: an introduction*: John Wiley & Sons.

Callister, W. D., & Rethwisch, D. G. (2013). *Fundamentals of materials science and engineering* (Vol. 471660817): Wiley.

Carcia, P., McLean, R., Reilly, M., & Nunes Jr, G. (2003). Transparent ZnO thin-film transistor fabricated by rf magnetron sputtering. *Applied Physics Letters, 82*(7), 1117-1119.

Chaari, M., & Matoussi, A. (2012). Electrical conduction and dielectric studies of ZnO pellets. *Physica B: Condensed Matter, 407*(17), 3441-3447.

Chakrabarti, S., Ganguli, D., & Chaudhuri, S. (2004). Substrate dependence of preferred orientation in sol–gel-derived zinc oxide films. *Materials Letters, 58*(30), 3952-3957.

Chen, M., Wang, X., Yu, Y., Pei, Z., Bai, X., Sun, C., . . . Wen, L. (2000). X-ray photoelectron spectroscopy and auger electron spectroscopy studies of Al-doped ZnO films. *Applied Surface Science, 158*(1), 134-140.

Cho, A. Y. (1971). Film deposition by molecular-beam techniques. *Journal of Vacuum Science & Technology, 8*(5), S31-S38.

Corriu, R. J., & Leclercq, D. (1996). Recent developments of molecular chemistry for sol–gel processes. *Angewandte Chemie International Edition in English, 35*(13-14), 1420-1436.

Das, R. N., Pati, R. K., & Pramanik, P. (2000). A novel chemical route for the preparation of nanocrystalline PZT powder. *Materials Letters, 45*(6), 350-355.

Decremps, F., Zhang, J., & Liebermann, R. (2000). New phase boundary and high-pressure thermoelasticity of ZnO. *EPL (Europhysics Letters), 51*(3), 268.

Desgreniers, S. (1998). High-density phases of ZnO: Structural and compressive parameters. *Physical Review B, 58*(21), 14102.

Djurišić, A., Choy, W. C., Roy, V. A. L., Leung, Y. H., Kwong, C. Y., Cheah, K. W., . . . Surya, C. (2004). Photoluminescence and electron paramagnetic resonance of ZnO tetrapod structures. *Advanced Functional Materials, 14*(9), 856-864.

Do, L.-M., Kim, K., Zyung, T., Shim, H.-K., & Kim, J.-J. (1997). In situ investigation of degradation in polymeric electroluminescent devices using time-resolved confocal laser scanning microscope. *Applied Physics Letters, 70*(25), 3470-3472.

Ellmer, K. (2000). Magnetron sputtering of transparent conductive zinc oxide: relation between the sputtering parameters and the electronic properties. *Journal of Physics D: Applied Physics, 33*(4), R17.

Ellmer, K., Klein, A., & Rech, B. (2007). *Transparent conductive zinc oxide: basics and applications in thin film solar cells* (Vol. 104): Springer Science & Business Media.

Fan, X., Lian, J., Zhao, L., & Liu, Y. (2005). Single violet luminescence emitted from ZnO films obtained by oxidation of Zn film on quartz glass. *Applied Surface Science, 252*(2), 420-424.

Fortunato, E. M., Pimentel, A., Gonçalves, A., Marques, A., Pereira, L., & Martins, R. (2005). Fully Transparent ZnO Thin-Film Transistor Produced at Room Temperature. *Advanced Materials, 17*(5), 590-594.

Fujihara, S., Sasaki, C., & Kimura, T. (2001). Crystallization behavior and origin of c-axis orientation in sol–gel-derived ZnO:Li thin films on glass substrates. *Applied Surface Science, 180*(3–4), 341-350.

Fujii, T., Nishikiori, H., & Tamura, T. (1995). Absorption spectra of rhodamine B dimers in dip-coated thin films prepared by the sol-gel method. *Chemical Physics Letters, 233*(4), 424-429.

Gagandeep, Singh, K., Lark, B. S., & Sahota, H. S. (2000). Attenuation measurements in solutions of some carbohydrates. *Nuclear Science and Engineering, 134*(2), 208-217.

Gao, T., & Wang, T. (2005). Synthesis and properties of multipod-shaped ZnO nanorods for gas-sensor applications. *Applied Physics A, 80*(7), 1451-1454.

Gfroerer, T. H. (2000). Photoluminescence in analysis of surfaces and interfaces. *Encyclopedia of Analytical Chemistry*.

Gorla, C., Emanetoglu, N., Liang, S., Mayo, W., Lu, Y., Wraback, M., & Shen, H. (1999). Structural, optical, and surface acoustic wave properties of epitaxial ZnO films grown on (011 2) sapphire by metalorganic chemical vapor deposition. *Journal of Applied Physics, 85*(5), 2595-2602.

Guglielmi, M., & Carturan, G. (1988). Precursors for sol-gel preparations. *Journal of Non-Crystalline Solids, 100*(1), 16-30.

Habibi, M., & Sardashti, M. K. (2008). Structure and morphology of nanostructured zinc oxide thin films Prepared by dip-vs. spin-coating methods. *Journal of the Iranian Chemical Society, 5*(4), 603-609.

Hamid, H. B. A. (2009). Fabrication, structural and electrical characteristics of zinc oxide thin films by direct current sputtering.

Hickernell, F. S. (1976). Zinc-oxide thin-film surface-wave transducers. *Proceedings of the IEEE, 64*(5), 631-635.

Hosono, E., Fujihara, S., Kimura, T., & Imai, H. (2004). Non-basic solution routes to prepare ZnO nanoparticles. *Journal of Sol-gel Science and Technology, 29*(2), 71-79.

Hsieh, P.-T., Chen, Y.-C., Kao, K.-S., & Wang, C.-M. (2008). Luminescence mechanism of ZnO thin film investigated by XPS measurement. *Applied Physics A, 90*(2), 317-321.

Hsu, L., Yeh, C., Kuo, C., Huang, B., & Dhar, S. (2005). Optical and transport properties of undoped and Al-, Ga-and In-doped ZnO thin films. *Journal of Optoelectronics and Advanced Materials, 7*(6), 3039.

Hu, M. Z.-C., Payzant, E. A., & Byers, C. H. (2000). Sol–gel and ultrafine particle formation via dielectric tuning of inorganic salt–alcohol–water solutions. *Journal of Colloid and Interface Science, 222*(1), 20-36.

Hung, L., & Chen, C. (2002). Recent progress of molecular organic electroluminescent materials and devices. *Materials Science and Engineering: R: Reports, 39*(5), 143-222.

Hutson, A. (1960). Piezoelectricity and conductivity in ZnO and CdS. *Physical Review Letters, 4*(10), 505.

Ilican, S., Caglar, Y., & Caglar, M. (2008). Preparation and characterization of ZnO thin films deposited by sol-gel spin coating method. *Journal of Optoelectronics and advanced materials, 10*(10), 2578-2583.

Inamdar, D., Agashe, C., Kadam, P., & Mahamuni, S. (2012). Doping optimization and surface modification of aluminum doped zinc oxide films as transparent conductive coating. *Thin Solid Films, 520*(11), 3871-3877.

Jeong, S.-H., Kim, B.-S., & Lee, B.-T. (2003). Photoluminescence dependence of ZnO films grown on Si (100) by radio-frequency magnetron sputtering on the growth ambient. *Applied Physics Letters, 82*(16), 2625-2627.

Jiang, X., Wong, F., Fung, M., & Lee, S. (2003). Aluminum-doped zinc oxide films as transparent conductive electrode for organic light-emitting devices. *Applied Physics Letters, 83*(9), 1875-1877.

Jimenez-Gonzalez, A., Urueta, J. A. S., & Suarez-Parra, R. (1998). Optical and electrical characteristics of aluminum-doped ZnO thin films prepared by solgel technique. *Journal of Crystal Growth, 192*(3), 430-438.

Jin, B., Im, S., & Lee, S. Y. (2000). Violet and UV luminescence emitted from ZnO thin films grown on sapphire by pulsed laser deposition. *Thin Solid Films, 366*(1), 107-110.

Kakati, N., Jee, S. H., Kim, S. H., Oh, J. Y., & Yoon, Y. S. (2010). Thickness dependency of sol-gel derived ZnO thin films on gas sensing behaviors. *Thin Solid Films, 519*(1), 494-498.

Karzel, H., Potzel, W., Köfferlein, M., Schiessl, W., Steiner, M., Hiller, U., . . . Blaha, P. (1996). Lattice dynamics and hyperfine interactions in ZnO and ZnSe at high external pressures. *Physical Review B, 53*(17), 11425.

Kita, Y., Furukawa, A., Futamura, J., Ueda, K., Sawama, Y., Hamamoto, H., & Fujioka, H. (2001). Remarkable effect of aluminum reagents on rearrangements of epoxy acylates via stable cation intermediates and its application to the synthesis of (S)-(+)-sporochnol A. *Journal of Organic Chemistry, 66*(26), 8779-8786.

Klenk, R., Klaer, J., Scheer, R., Lux-Steiner, M. C., Luck, I., Meyer, N., & Rühle, U. (2005). Solar cells based on CuInS 2—an overview. *Thin Solid Films, 480*, 509-514.

Klingshirn, C., Priller, H., Decker, M., Brückner, J., Kalt, H., Hauschild, R., . . . Thonke, H. W. K. (2005). Excitonic properties of ZnO *Advances in Solid State Physics* (pp. 275-287): Springer.

Kolosov, D., English, D., Bulovic, V., & Barbara, P. (2001). Forrest SR and Thompson ME. *Journal of Applied Physics, 2001*, 90.

Könenkamp, R. (2000). *Photoelectric properties and applications of low-mobility semiconductors* (Vol. 167): Springer Science & Business Media.

Lee, J.-H., Ko, K.-H., & Park, B.-O. (2003). Electrical and optical properties of ZnO transparent conducting films by the sol–gel method. *Journal of Crystal Growth, 247*(1), 119-125.

Levinson, L. M., & Philipp, H. R. (1986). Zinc oxide varistors—a review. *American Ceramic Society Bulletin, 65*(4), 639-646.

Lin, Y.-H. (2010). *Structure and properties of transparent conductive ZnO films grown by pulsed laser deposition (PLD).* University of Birmingham.

Liu, Z., Li, J., Ya, J., Xin, Y., & Jin, Z. (2008). Mechanism and characteristics of porous ZnO films by sol–gel method with PEG template. *Materials Letters, 62*(8–9), 1190-1193.

Livage, J., Henry, M., & Sanchez, C. (1988). Sol-gel chemistry of transition metal oxides. *Progress in Solid State Chemistry, 18*(4), 259-341.

Lou, X., Shen, H., & Shen, Y. (1991). Development of ZnO series ceramic semiconductor gas sensors. *Journal of Transducer Technology, 3*(1).

Ma, Y., Du, G., Yang, S., Li, Z., Zhao, B., Yang, X., . . . Liu, D. (2004). Control of conductivity type in undoped ZnO thin films grown by metalorganic vapor phase epitaxy. *Journal of Applied Physics, 95*(11), 6268-6272.

Manifacier, J., Gasiot, J., & Fillard, J. (1976). A simple method for the determination of the optical constants n, k and the thickness of a weakly absorbing thin film. *Journal of Physics E: Scientific Instruments, 9*(11), 1002.

Matsuoka, M. (1971). Nonohmic properties of zinc oxide ceramics. *Japanese journal of applied physics, 10*(6), 736.

Meulenkamp, E. A. (1998). Synthesis and growth of ZnO nanoparticles. *The Journal of Physical Chemistry B, 102*(29), 5566-5572.

Miki-Yoshida, M., Paraguay-Delgado, F., Estrada-Lopez, W., & Andrade, E. (2000). Structure and morphology of high quality indium-doped ZnO films obtained by spray pyrolysis. *Thin Solid Films, 376*(1), 99-109.

Mitzi, D. B. (2001). Thin-film deposition of organic-inorganic hybrid materials. *Chemistry of Materials, 13*(10), 3283-3298.

Mondal, S., Bhattacharyya, S., & Mitra, P. (2013). Effect of Al doping on microstructure and optical band gap of ZnO thin film synthesized by successive ion layer adsorption and reaction. *Pramana, 80*(2), 315-326.

Muhammad, F. F., & Sulaiman, K. (2011). Tuning the optical band gap of DH-6T by Alq_3 dopant. *Sains Malaysiana, 40*(1), 17-20.

Natsume, Y., & Sakata, H. (2000). Zinc oxide films prepared by sol-gel spin-coating. *Thin Solid Films, 372*(1), 30-36.

Nishio, K., Miyake, S., Sei, T., Watanabe, Y., & Tsuchiya, T. (1996). Preparation of highly oriented thin film exhibiting transparent conduction by the sol-gel process. *Journal of Materials Science, 31*(14), 3651-3656.

Nomura, K., Ohta, H., Ueda, K., Kamiya, T., Hirano, M., & Hosono, H. (2003). Thin-film transistor fabricated in single-crystalline transparent oxide semiconductor. *Science, 300*(5623), 1269-1272.

Norton, D. P., Heo, Y. W., Ivill, M. P., Ip, K., Pearton, S. J., Chisholm, M. F., & Steiner, T. (2004). ZnO: growth, doping & processing. *Materials Today, 7*(6), 34-40.

Ohyama, M., Kouzuka, H., & Yoko, T. (1997). Sol-gel preparation of ZnO films with extremely preferred orientation along (002) plane from zinc acetate solution. *Thin Solid Films, 306*(1), 78-85.

Ohyama, M., Kozuka, H., Yoko, T., & Sakka, S. (1996). Preparation of ZnO films with preferential orientation by sol-gel method. *Nippon Seramikkusu Kyokai Gakujutsu Ronbunshi, 104*(4), 296-300.

Olson, D. C., Shaheen, S. E., White, M. S., Mitchell, W. J., van Hest, M. F. A. M., Collins, R. T., & Ginley, D. S. (2007). Band-Offset Engineering for Enhanced Open-Circuit Voltage in Polymer–Oxide Hybrid Solar Cells. *Advanced Functional Materials, 17*(2), 264-269.

Ondo-Ndong, R., Ferblantier, G., Al Kalfioui, M., Boyer, A., & Foucaran, A. (2003). Properties of RF magnetron sputtered zinc oxide thin films. *Journal of Crystal Growth, 255*(1), 130-135.

Ono, S., Yamazaki, O., Ohji, K., Wasa, K., & Hayakawa, S. (1978). SAW resonators using rf-sputtered ZnO films on glass substrates. *Applied Physics Letters, 33*(3), 217-218.

Özgür, Ü., Alivov, Y. I., Liu, C., Teke, A., Reshchikov, M., Doğan, S., . . . Morkoc, H. (2005). A comprehensive review of ZnO materials and devices. *Journal of Applied Physics, 98*(4), 041301.

Park, S.-H. K., Lee, J.-I., Hwang, C.-S., & Chu, H. Y. (2005). Characteristics of organic light emitting diodes with Al-doped ZnO anode deposited by atomic layer deposition. *Japanese Journal of Applied Physics, 44*(2), 1-7.

Patil, G., Kajale, D., Gaikwad, V., & Jain, G. (2012). Spray pyrolysis deposition of nanostructured tin oxide thin films. *ISRN Nanotechnology, 2012*.

Pierre, A. C. (2013). *Introduction to sol-gel processing* (Vol. 1): Springer Science & Business Media.

Pontes, F., Pontes, D., Leite, E., Longo, E., Santos, E., Mergulhao, S., & Varela, J. A. (2003). Synthesis, ferroelectric and optical properties of (Pb, Ca) TiO3 thin films by soft solution processing. *Journal of Sol-gel Science and Technology, 27*(2), 137-147.

Raja, K., Ramesh, P., & Geetha, D. (2014). Synthesis, structural and optical properties of ZnO and Ni-doped ZnO hexagonal nanorods by Co-precipitation method. *Spectrochimica Acta Part A: Molecular and Biomolecular Spectroscopy, 120*, 19-24.

Ramanathan, K., Contreras, M. A., Perkins, C. L., Asher, S., Hasoon, F. S., Keane, J., . . . Noufi, R. (2003). Properties of 19.2% efficiency ZnO/CdS/CuInGaSe2 thin-film solar cells. *Progress in Photovoltaics: Research and Applications, 11*(4), 225-230.

Rech, B., & Wagner, H. (1999). Potential of amorphous silicon for solar cells. *Applied physics A, 69*(2), 155-167.

Rossinelli, M., Blatter, G., & Greuter, F. (1984). Grain boundary properties of ZnO varistors. *Electrical Ceramics*, 1-17.

Roy, V., Djurisic, A., Chan, W., Gao, J., Lui, H., & Surya, C. (2003). Luminescent and structural properties of ZnO nanorods prepared under different conditions. *Applied Physics Letters, 83*(1), 141-143.

Schwartz, R. W. (1997). Chemical solution deposition of perovskite thin films. *Chemistry of Materials, 9*(11), 2325-2340.

Segets, D., Gradl, J., Taylor, R. K., Vassilev, V., & Peukert, W. (2009). Analysis of optical absorbance spectra for the determination of ZnO nanoparticle size distribution, solubility, and surface energy. *ACS nano, 3*(7), 1703-1710.

Sheeba, N., Vattappalam, S. C., Sreenivasan, P., Mathew, S., & Philip, R. R. (2016). Influence of Sb incorporation on optical, electrical and gas sensing properties of transparent ZnO thin films. *Materials Chemistry and Physics, 179*, 137-142.

Shen, X.-P., Yuan, A.-H., Hu, Y.-M., Jiang, Y., Xu, Z., & Hu, Z. (2005). Fabrication, characterization and field emission properties of large-scale uniform ZnO nanotube arrays. *Nanotechnology, 16*(10), 2039.

Shim, E. S., Kang, H. S., Kang, J. S., Kim, J. H., & Lee, S. Y. (2002). Effect of the variation of film thickness on the structural and optical properties of ZnO thin films deposited on sapphire substrate using PLD. *Applied Surface Science, 186*(1), 474-476.

Shrestha, S. P., Ghimire, R., Nakarmi, J. J., Kim, Y.-S., Shrestha, S., Park, C.-Y., & Boo, J.-H. (2010). Properties of ZnO: Al films prepared by spin coating of aged precursor solution. *Bulletin of the Korean Chemical Society, 31*(1), 112-115.

Singh, G., Shrivastava, S., Jain, D., Pandya, S., Shripathi, T., & Ganesan, V. (2010). Effect of indium doping on zinc oxide films prepared by chemical spray pyrolysis technique. *Bulletin of Materials Science, 33*(5), 581-587.

Smith, D. Thin-film deposition: principles and practice. 1995. New York: McGraw Hill.

Souri, D. (2011). Effect of molybdenum tri-oxide molar ratio on the optical and some physical properties of tellurite–vanadate–molybdate glasses. *Measurement, 44*(4), 717-721.

Spanhel, L. (2006). Colloidal ZnO nanostructures and functional coatings: a survey. *Journal of Sol-gel Science and Technology, 39*(1), 7-24.

Spanhel, L., & Anderson, M. A. (1991). Semiconductor clusters in the sol-gel process: quantized aggregation, gelation, and crystal growth in concentrated zinc oxide colloids. *Journal of the American Chemical Society, 113*(8), 2826-2833.

Srikant, V., & Clarke, D. R. (1998). On the optical band gap of zinc oxide. *Journal of Applied Physics, 83*, 5447.

Sun. (2000). (PhD Thesis), University of Science and Technology of China.

Sun, D., Wong, M., Sun, L., Li, Y., Miyatake, N., & Sue, H.-J. (2007). Purification and stabilization of colloidal ZnO nanoparticles in methanol. *Journal of Sol-gel Science and Technology, 43*(2), 237-243.

Tauc, J., Grigorovici, R., & Vancu, A. (1966). Optical properties and electronic structure of amorphous germanium. *Physica Status Solidi B, 15*(2), 627-637.

Thomas, G. (1997). Materials science: Invisible circuits. *Nature, 389*(6654), 907-908.

Tiku, S., Lau, C., & Lakin, K. (1980). Chemical vapor deposition of ZnO epitaxial films on sapphire. *Applied Physics Letters, 36*(4), 318-320.

Tu, K.-N., Mayer, J. W., & Feldman, L. C. (1992). Electronic thin film science: Macmillan, New York.

Van Slyke, S., Chen, C., & Tang, C. (1996). Organic electroluminescent devices with improved stability. *Applied Physics Letters, 69*(15), 2160-2162.

Wang, J., Cao, J., Fang, B., Lu, P., Deng, S., & Wang, H. (2005). Synthesis and characterization of multipod, flower-like, and shuttle-like ZnO frameworks in ionic liquids. *Materials Letters, 59*(11), 1405-1408.

Wang, M., Kim, E. J., Chung, J. S., Shin, E. W., Hahn, S. H., Lee, K. E., & Park, C. (2006). Influence of annealing temperature on the structural and optical properties of sol–gel prepared ZnO thin films. *Physica Status Solidi A, 203*(10), 2418-2425.

Wang, Z. L. (2008). Splendid one-dimensional nanostructures of zinc oxide: a new nanomaterial family for nanotechnology. *ACS nano, 2*(10), 1987-1992.

Xiang, H., Wei, S.-H., & Gong, X. (2009). Identifying Optimal Inorganic Nanomaterials for Hybrid Solar Cells. *The Journal of Physical Chemistry C, 113*(43), 18968-18972.

Xie, G., Fanga, L., Peng, L., Liu, G., Ruan, H., Wu, F., & Kong, C. (2012). Effect of In-doping on the optical constants of ZnO thin films. *Physics Procedia, 32*, 651-657.

Zak, A. K., Abrishami, M. E., Majid, W., Yousefi, R., & Hosseini, S. (2011). Effects of annealing temperature on some structural and optical properties of ZnO nanoparticles prepared by a modified sol–gel combustion method. *Ceramics International, 37*(1), 393-398.

Zak, A. K., Razali, R., Majid, W. A., & Darroudi, M. (2011). Synthesis and characterization of a narrow size distribution of zinc oxide nanoparticles. *International Journal of Nanomedicine, 6*, 1399.

Zhang, Y. (2004). High Quality ZnO Epitaxial Grown By Plasma Assisted Molecular Beam Epitaxy.

Znaidi, L. (2010). Sol–gel-deposited ZnO thin films: a review. *Materials Science and Engineering: B, 174*(1), 18-30.

LIST OF PUBLICATIONS AND PAPERS PRESENTED

1. **Basri, S. H.**; Za'aba, N. K.; Sarjidan, M. A. Mohd; Majid, W. H. Abd. (2013). Effect of Transition Metal Dopant on the Optoelectronics Properties of Zinc Oxide Thin Film. *Journal of Nanoelectronics and Optoelectronics, 8 (5),* 425-430.

2. **Basri, S.H.**, Mohd Sarjidan, M.A., Abd Majid, W.H. (2014). Structural and optical properties of nickel-doped and undoped zinc oxide thin films deposited by sol-gel method. *Advanced Materials Research, 895,* 250-253.

3. Sarjidan, M. A. Mohd; Salleh, N. S.; **Basri, S. H.**; Razali, R.; Za'aba, N. K.; Majid, W. H. Abd. (2014) Tunable optoelectronic properties of sol–gel derived ZnO nanostructure thin film by annealing treatment. *Materials Express, 4,* 422-428.